

AN INVESTIGATION OF SOME UNUSUAL SINGLE CRYSTALS
OF
THE HEAVY FERMION SUPERCONDUCTOR UBe_{13}

By
STEPHEN G. THOMAS

A DISSERTATION PRESENTED TO THE GRADUATE SCHOOL
OF THE UNIVERSITY OF FLORIDA IN PARTIAL FULFILLMENT
OF THE REQUIREMENTS FOR THE DEGREE OF
DOCTOR OF PHILOSOPHY

UNIVERSITY OF FLORIDA

1998

ACKNOWLEDGMENTS

I would like to begin by thanking my advisor, Dr. Greg Stewart, for suggesting this interesting problem. He is indeed a true “idea man” with a keen eye for data. I am also grateful to Dr. Peter Hirschfeld and Dr. Pradeep Kumar for taking an interest in this work and offering many helpful suggestions.

There is quite an extensive “without whom this work would never have been finished” list associated with this dissertation. My lab-mates Dr. Bohdan Andraka, Dr. Jung Soo Kim, and Richard Pietri all contributed technical advice and labor to this effort. Mr. Wayne Acree measured a seemingly endless stream of samples for me and now knows that “last one” really means “10 more.” The guys of the Physics Department machine and electrical shops took my rather crude sketches and/or pleas for help and turned them into real working devices. Computer assistance from Mr. Chandra Chegiredy and Mr. Dan Roscigno was ever present and, as is always the case for those guys, not fully appreciated. Thanks go to Mrs. Susan Rizzo, Mrs. Darlene Latimer, and Mrs. Janet Germany for reminding me of important dates, papers to sign, papers to initial, papers to file, papers to update, and for the free candy. The documentation template was graciously provided by Dr. Yuli Kanev and Dr. Mike Jones. I especially want to thank my good friend Mike Jones for joining me in hoisting the poundage and lending much time and effort to the computer aspects of this work. If only everyone would accept payment in burritos.

On the personal side I am lucky to have been able to meet so many good people while I did science in this town. Cheers go to my dear friends. No amount of “fancy book learnin’ “ could ever equal what I have learned from all of them.

TABLE OF CONTENTS

ACKNOWLEDGMENTS	ii
ABSTRACT	vi
CHAPTERS	
1 INTRODUCTION	1
1.1 Properties of Heavy Fermion Compounds	1
1.1.1 Specific Heat	2
1.1.2 Magnetic Susceptibility	3
1.1.3 Resistivity	7
1.1.4 Other Properties	7
1.2 The Heavy Fermion Superconducting State	9
1.3 Theories of the Heavy Fermion Ground State	12
2 PROPERTIES OF UBe_{13}	18
2.1 Normal State Properties of UBe_{13}	18
2.1.1 Normal State Specific Heat	19
2.1.2 Resistivity	22
2.1.3 Magnetic Susceptibility	25
2.1.4 Neutron Scattering	28
2.2 Superconducting Properties of UBe_{13}	28
2.2.1 Superconducting Length Scales	29
2.2.2 Upper Critical Magnetic Field	30
2.2.3 Specific Heat	32
3 MOTIVATION	42
4 EXPERIMENTAL METHODS	46
4.1 Preparation of Polycrystalline Samples	46
4.2 Preparation of Single Crystalline UBe_{13}	46
4.3 Annealing	47
4.4 Measurement of Specific Heat	48
4.4.1 The Sample Platforms	49
4.4.2 Cryostats	53

4.4.3	Specific Heat in Magnetic Field	53
4.5	Resistivity	53
4.5.1	Resistivity in Magnetic Field	54
4.6	D.C. Magnetic Susceptibility and Magnetization	54
4.7	Microprobe Microanalysis	54
4.8	X-ray Diffraction	56
5	RESULTS	59
5.1	Electron Probe Microanalysis	60
5.2	X-ray Analysis	76
5.3	Magnetic Susceptibility	87
5.4	Specific Heat	96
5.4.1	Polycrystalline Data	122
5.4.2	Specific Heat in Magnetic Field	141
5.5	Resistivity and Magnetoresistance	158
5.6	Other Studies	167
6	CONCLUSION	173
6.1	Review of Results	173
6.2	Comparisons to B doped UBe_{13}	178
6.3	Impurities and UBe_{13}	186
6.4	Symmetry and f -electron Correlations	187
6.5	Future Work	193
APPENDICES		
A	$\chi_{D.C.}$ ANOMALY I	195
A.1	Magnetic Susceptibility	195
B	$\chi_{D.C.}$ ANOMALY II	218
B.1	X-ray Analysis	218
B.2	Resistivity	220
REFERENCES		223
BIOGRAPHICAL SKETCH		233

Abstract of Dissertation Presented to the Graduate School
of the University of Florida in Partial Fulfillment of the
Requirements for the Degree of Doctor of Philosophy

AN INVESTIGATION OF SOME UNUSUAL SINGLE CRYSTALS
OF
THE HEAVY FERMION SUPERCONDUCTOR UBe_{13}

By

Stephen G. Thomas

December 1998

Chairman: G.R. Stewart
Major Department: Physics

We report a study of 9 anomalous single crystals of the heavy Fermion superconductor UBe_{13} . The anomalous crystals possess a T_c depressed by roughly 20% and a specific heat jump at T_c (ΔC_{T_c}) enhanced by as much as 50% compared to standard UBe_{13} samples. Characterization of this big-jump-low- T_c (*BJLT*) ground state was accomplished through x-ray diffraction, d.c. magnetic susceptibility, resistivity, specific heat, and electron-probe microanalysis (*EPMA*).

Incorporation of *Al* into the *BJLT* lattice during the growth process results in an average single crystal stoichiometry of $UBe_{12.89}Al_{.11}$. The *Al* is found to reside predominantly on the *BeI* lattice site, expanding the lattice 50% less than in polycrystalline $UBe_{12.89}Al_{.11}$. Annealing polycrystalline $UBe_{12.89}Al_{.11}$ at $1400^\circ C$ for 5 hours and cooling to $1000^\circ C$ at $15^\circ C$ /hour redistributes a majority of the *Al* to the *BeI* lattice site and induces a *BJLT*-like ground state. Low temperature specific heat results give no indication of an increase in the density of states or superconducting entropy of the *BJLT* transition.

A 60% reduction in the amplitude and a 25% reduction in the characteristic temperature of the high temperature specific heat anomaly in the *BJLT* crystals relative to standard UBe_{13} indicates a significant change in the local U -ion environment. The anomaly is almost completely suppressed in unannealed $UBe_{12.89}Al_{.11}$ and is restored to a *BJLT*-like state after annealing. We associate the change in the local U f -electron environment to be proportional to the suppression of the amplitude and frequency of intersite dynamic f -electron correlations.

Our data are interpreted in terms of strong coupling theory, in which $\Delta C_{T_c} \propto T_c/\omega_0$, where ω_0 is the frequency of the f -electron correlations, and static and dynamic pair breaking. *Al* acts as a static pair breaker in all samples, reducing T_c . The dynamic pair breaking effects of the low frequency f -electron correlations are enhanced due to the preferential ordering of the *Al* impurity on the *BeI* lattice site. As ω_0 is reduced ΔC_{T_c} is enhanced. Suggestions for future work are offered.

CHAPTER 1 INTRODUCTION

In 1979 a bulk superconducting transition was discovered in the large-effective-mass intermetallic compound $CeCu_2Si_2$ [1]. This single result ushered in the era of “heavy Fermion superconductivity”, so named for those superconducting compounds which possess an electron effective mass some two to three orders of magnitude larger than that found in ordinary metals. Since the effective mass is directly proportional to the electronic density of states at the Fermi level, heavy Fermion (HF) compounds are characterized by enormous values of the low temperature electronic specific heat and magnetic susceptibility. In the first two sections of this chapter we discuss the fundamentals of HF compounds and HF superconductors. General experimental properties and trends are presented. A theoretical description of the HF ground state follows.

1.1 Properties of Heavy Fermion Compounds

Heavy Fermion materials are intermetallic compounds in which one of the constituents is a rare-earth or actinide atom (usually Ce or U) with a partially filled $4f$ or $5f$ electron shell. These electronic f -states at the Fermi surface are localized at high temperatures. As the temperature is lowered these localized electronic states become itinerant and eventually form a narrow f -band of strongly interacting electrons, or quasi-particles, located just above the Fermi energy. This gives rise to

some highly unusual properties which we are able to observe through thermal and transport property measurements [2, 3, 4, 5, 6, 7]. One such property, the electron effective mass, (m^*), is significantly enhanced in these systems. The electronic density of states at the Fermi level ($N(0)$) is inversely proportional to the Fermi energy (E_f). This in turn is inversely proportional to m^* . Thus, as shown below, a large density of states at the Fermi level implies an enhanced electron effective mass which is proportional to the electronic specific heat coefficient (γ) at low temperature. Heavy Fermion compounds exist in a variety of ground states. The following sections describe the properties of these compounds in terms of thermal and transport property measurements.

1.1.1 Specific Heat

The well known expression for the specific heat (C) of a normal metal in the free-electron model is [8]

$$C = \gamma T + \beta T^3 \quad (1.1)$$

for temperatures well below the Debye temperature (Θ_D). Here, γ and β are given by the following expressions:

$$\gamma = \frac{N(0)\pi^2 K_B^2}{3} \quad (1.2)$$

$$\beta = \frac{1944 \times 10^3 n}{\Theta_D^3} \quad (1.3)$$

where K_B is Boltzmann's constant ($1.38062 \times 10^{-23} J/K$) and n is the number of atoms in a formula unit of the compound. A simple argument, based on a spherical

Fermi surface with wave vector K_F , gives [8]

$$N(0) = \frac{mK_F}{\hbar^2 \pi^2} \quad (1.4)$$

with \hbar equal to Plank's constant divided by 2π ($1.05459 \times 10^{-34} Js$) and m the free electron mass. By rearranging equations 1.1-1.4 it is easy to show that m is directly proportional to the low temperature specific heat coefficient γ . At sufficiently low temperatures where we are able to neglect the phonon contribution (β) to C , a measurement of C/T is a direct measurement of the density of states at the Fermi energy, which is proportional to the electron mass. As we shall see in section 1.3, the density of states at the Fermi level need only be modified by replacing the bare electron mass m with an effective mass m^* when moving from a free electron to a Fermi liquid picture. Due to interactions between electrons and between electrons and phonons, the bare density of states is "dressed" by an interaction term $(1 + \lambda)$ and we no longer speak of single electrons. Rather, the term quasiparticle is used, and it is the quasiparticles that possess the highly enhanced m^* which characterizes HF compounds. Table 1.1 lists some HF compounds and their respective ground states. Note the enormous values of $\gamma(T \rightarrow 0)$ compared to elemental Cu and Pd .

1.1.2 Magnetic Susceptibility

At room temperature the f -electron atoms of HF compounds behave as a collection of localized, weakly interacting moments. The susceptibility (χ) follows the Curie-Weiss form [8]:

$$\chi = \frac{n\mu_{eff}^2}{3K_B(T - \Theta_{CW})} \quad (1.5)$$

Table 1.1: A listing of some HF compounds and their respective ground states.

Compound	Ground State	$\gamma(T \rightarrow 0)$ $\frac{mJ}{(mole-K^2)}$	Transition Temperature (K)	References
<i>CeCu₆</i>	Paramagnetic	1300	–	[9]
<i>UPt₄Au</i>	Paramagnetic	710	–	[10]
<i>UAl₂</i>	Paramagnetic	142	–	[11]
<i>U₂Zn₁₇</i>	Antiferromagnetic	500	$T_N=9.7$	[12]
<i>UCd₁₁</i>	Antiferromagnetic	840	$T_N=5$	[13]
<i>UBe₁₃</i>	Superconducting	1000	$T_c=.9$	[14]
<i>UPt₃</i>	Superconducting/ Antiferromagnetic	450	$T_c=.5$ $T_N=5$	[15]
<i>CeCu₂Si₂</i>	Superconducting	1000	$T_c=.65$	[1]
<i>URu₂Si₂</i>	Superconducting/ Antiferromagnetic	180	$T_c=1.5$ $T_N=17$	[16]
<i>UPd₂Al₃</i>	Superconducting/ Antiferromagnetic	150	$T_c=2$ $T_N=14$	[17]
<i>Cu</i>	Paramagnetic	.695		
<i>Pd</i>	Paramagnetic	9.4		

where n is the density of local moments, μ_{eff} is the magnitude of the local moment in Bohr magnetons ($1\mu_B = 9.27410 \times 10^{-24} J/T$), and Θ_{CW} is the Curie-Weiss temperature. As the temperature is lowered this local moment behavior gives way to a more itinerant behavior, characterized by a narrow band of conduction electrons. The low temperature susceptibility increases with decreasing temperature, and can approach values two to three orders of magnitude greater than the temperature independent Pauli susceptibility for a gas of non-interacting electrons. We can write χ for a gas of non-interacting electrons in terms of $N(0)$ [8] :

$$\chi = \mu_B^2 N(0) \quad (1.6)$$

where μ_B is the Bohr magneton. It is an experimental fact that the ratio of χ/γ for HF compounds is similar to that of ordinary metals. This indicates the low temperature susceptibility and specific heat are both enhanced by roughly the same factor, and the effective mass is also a useful concept for χ as well as C . We also note the Wilson ratio (R) given by [18]

$$R = \frac{\pi^2 K_B^2 \chi(T \rightarrow 0)}{\mu_{eff}^2 \gamma(T \rightarrow 0)} \quad (1.7)$$

reveals a trend in which pure superconducting HF systems have R values which are uniformly less than those for non-magnetic HF systems. What this means is uncertain. Table 1.2 gives representative values of μ_{eff} , Θ_{cw} , $\chi(T \rightarrow 0)$ and the Wilson ratio for some HF compounds. Notice the enormous values of $\chi(T \rightarrow 0)$ compared to that of Pd .

Table 1.2: Magnetic susceptibility data and the Wilson ratio for a selection of HF compounds.

Compound	μ_{eff} (μ_B)	Θ_{CW} (K)	$\chi(T \rightarrow 0)$ $\frac{emu}{mole}$	Wilson Ratio $\frac{218.7\chi}{\gamma\mu_{eff}^2}$	References
<i>CeCu₆</i>	2.67	-59/-18	23.3	.55	[19]
<i>UPt₄Au</i>	3.09	a,b/c axis -125	12.9 T=1.8K	.42	[20]
<i>UAl₂</i>	3.1	-245	10.8	1.73	[21]
<i>U₂Zn₁₇</i>	3.3	-105	15.8/20	.63/.8	[22]
			a,b/c axis		
<i>UCd₁₁</i>	3.45	-23	38.4	.84	[13]
<i>UBe₁₃</i>	3.08	-53	15	.35	[14]
<i>UPt₃</i>	2.6	-50/-170	15.8/8.3	1.13/.59	[23]
		a/c axis	a/c axis	a/c axis	
<i>CeCu₂Si₂</i>	2.68	-140	10.8	.33	[24]
<i>URu₂Si₂</i>	3.51	-65	2.5/8.3	.25/.82	[25]
		c axis	a/c axis		
<i>UPd₂Al₃</i>	3.2	-47	11.7	1.66	[17]
<i>Pd</i>	****	****	.75		

1.1.3 Resistivity

The room temperature resistivity ($\rho(300K)$) of HF compounds is on the order of $100 \mu\Omega - cm$, which is roughly two orders of magnitude larger than that of ordinary metals. As the temperature is lowered, $\partial\rho/\partial T$ can be positive or negative. For many of the HF compounds ρ reaches a maximum (ρ_{max}) before falling off rapidly at the lowest temperatures. This maximum has been taken as evidence for the onset of coherence as the system enters the Fermi liquid state [26]. At very low temperatures many of these systems display a resistivity which suggests strong quasiparticle-quasiparticle scattering and a residual resistivity (ρ_0) of typically several $\mu\Omega - cm$, where [8]

$$\rho = \rho_0 + AT^2 \quad (1.8)$$

The parameter A , a measure of the strength of the quasiparticle-quasiparticle scattering, is up to 7 times larger in HF compounds than in ordinary metals. Values for ρ_0 , $\rho(300K)$ and the coefficient A are given in table 1.3 for a number of HF compounds [27, 28, 29, 30, 31, 32, 33].

1.1.4 Other Properties

In order to probe the Fermi surface, electron effective mass, and the density of states at the Fermi energy, experiments designed to probe the photoemission spectrum and investigate the de Haas-van Alphen effect have been performed [34, 35, 36, 37]. In some cases the geometry of the Fermi surface obtained has agreed well with theory. However, the electron effective mass obtained has been an order of magnitude larger than predicted from band structure calculations. This

Table 1.3: Resistivity data for some HF compounds.

Compound	ρ_0 ($\mu\Omega - cm$)	$\rho(300K)$ ($\mu\Omega - cm$)	A $\frac{\mu\Omega - cm}{K^2}$	References
<i>CeCu₆</i>	18.1/5.71/10.6 a/b/c axis	70	—	[27]
<i>UPt₄Au</i>	81 T=1.4K	158	2	[28]
<i>UAl₂</i>	4.8	190	10.7	[21]
<i>U₂Zn₁₇</i>	—	110	—	[12]
<i>UCd₁₁</i>	—	80	—	[13]
<i>UBe₁₃</i>	18	107	—	[14, 29]
<i>UPt₃</i>	.5	130	.5	[30]
<i>CeCu₂Si₂</i>	4.8	90	10.7	[31]
<i>URu₂Si₂</i>	33	324/169 a/c axis	.17/.10	[32]
<i>UPd₂Al₃</i>	3.5	140	—	[33]
<i>Cu</i>	.2(77K)	1.56(273K)		
<i>Pd</i>	****	20(273K)		

large discrepancy is roughly identical to the discrepancy between the measured specific heat and electronic structure calculations. Photoemission measurements have shown significant $4f$ and $5f$ electronic character at the Fermi energy in Ce and U based compounds respectively.

1.2 The Heavy Fermion Superconducting State

The study of heavy Fermion physics began with the discovery of heavy Fermion superconductivity in 1979. Since that time 5 more ambient pressure HF superconductors (HFS) have been discovered [14, 15, 16, 17, 38]. With penetration depths (λ) of several thousand Angstroms and coherence lengths (ξ) of typically several hundred Angstroms, HFS are strong type II superconductors. The large values of λ and ξ are a direct result of the large electron effective masses involved [8]. We know it is indeed the heavy electrons which are superconducting because the jump in the specific heat (ΔC) at T_c (ΔC_{T_c}) is proportional to the normal state specific heat at T_c . With the unique exception of UBe_{13} , which will be discussed in more detail in section 2.1, the remaining HFS possess a Cooper pair coupling strength parameter (β) comparable to the BCS weak coupling value [39] of 1.43, where

$$\beta = \frac{\Delta C_{T_c}}{C_{T_c}} \quad (1.9)$$

In addition to the presence of heavy superconducting electrons, there are several other features of HFS which distinguish them from traditional superconducting elements and compounds.

Power-law temperature dependencies for the NMR spin-lattice-relaxation rate, resistivity, specific heat, sound attenuation and penetration depth seem to indicate the presence of lines or point nodes where the energy gap vanishes on the Fermi surface [40]. A conventional superconductor possesses a finite energy gap over its entire Fermi surface, resulting in exponential temperature dependencies for the properties stated above. In addition, it is important to note that the symmetry of the energy gap is equal to that of the underlying Fermi surface in a conventional superconductor [41]. Thus the presence of line or point nodes and power-law temperature dependencies in HFS is indirect evidence for a possible unconventional ground state. Experiments have also shown that non-magnetic substitutional impurities are just as effective as magnetic impurities at breaking up the Cooper pairs in HFS and reducing T_c and ΔC_{T_c} dramatically. This is seen as evidence for non-s-wave pairing, as dilute concentrations of non-magnetic impurities in s-wave superconductors have little effect on T_c and ΔC_{T_c} [42]. The discovery of multiple superconducting transitions in $U_{1-x}Th_xBe_{13}$ [43] and UPt_3 [44] makes the strongest argument to date for an unconventional superconducting ground state in HFS. It is known that a type I superconductor exhibits only one Meissner phase in the field-temperature ($B - T$) phase diagram, while type II superconductors possess a Meissner phase plus a vortex state [45]. However, a superconductor in a triplet, p-wave ($L = 1$) state may undergo several zero field transitions as is witnessed in superfluid 3He , a true unconventional superfluid in which spin fluctuations play a crucial role in mediating the Fermion-Fermion pair attraction [46]. Further evidence for non-s-wave pairing comes from the observation of strong anti-ferromagnetic correlations in HFS. The close proximity of local-moment magnetism

to superconductivity is expected to break up the Cooper pairs in s-wave superconductors essentially by aligning the Cooper pair spins, minimizing the exchange energy and reducing the energy gap. This is certainly not observed in HFS.

The exotic and possibly unconventional nature of HFS is clear. The issue is not whether the underlying BCS theory, that (heavy) electrons condense into the lowest energy state at T_c and form highly overlapping electron pairs, is incorrect for these systems. However, the particular model on which the electron pairing is based is still an open question. In other words, what are the spin and angular momentum of the electron pairs and what is the mediator of this pairing? In conventional, phonon mediated superconductors the ratio of Θ_D to the Fermi temperature (T_F) is fully two orders of magnitude less than that for HFS. This suggests that maybe conventional pairing mechanisms are not appropriate in describing HFS. It is also known that so-called strong coupling effects, which arise when we express the difference in the free energy between the superconducting and normal states to second and higher orders in T_c/T_F , are much more significant in HFS than in ordinary, weak coupling, superconducting systems [47]. Questions concerning the symmetry of the pair wave function and the pairing mechanism of HFS are as yet unanswered and under active investigation. The evidence to date suggests unconventional superconductivity, but more stringent experiments need to be performed and more data needs to be collected. The search for anisotropy in the critical fields or penetration depth, and the investigation of the possibility of an inherently magnetic superconducting state are two of the most crucial aspects of HFS being investigated today.

1.3 Theories of the Heavy Fermion Ground State

We begin our discussion of the HF normal state at high temperature, where magnetic susceptibility data indicate local f -moment behavior. A phenomenological approach is provided by the single impurity Anderson model [48]. This model was originally intended for dilute magnetic impurity systems so we assume, in the high temperature limit, a decoupling of the highly concentrated HF f -orbitals. The Hamiltonian assumes an f -level in a Fermi sea of conduction electrons:

$$H = H_f + H_d + H_{fd} \quad (1.10)$$

where H_f is the Hamiltonian for the f -electron system, H_d describes the conduction electron system, and H_{fd} describes the f - d coupling. The hybridization between the f and d levels, introduced through H_{fd} , allows tunneling out of the localized f -level into the itinerant d -level, and vice versa. The matrix elements, V_k , are given by

$$V_k = \langle f_\alpha | H_{fd} | d_{k,\alpha} \rangle \quad (1.11)$$

where α represents the spin index. The Hamiltonians H_f and H_d are given by

$$H_f = \sum_{\alpha} E_f n_{\alpha} + \sum_{\alpha > \beta} U_{ff} n_{\alpha} n_{\beta} \quad (1.12)$$

$$H_d = \sum_{k,\alpha} e_k n_{k,\alpha} \quad (1.13)$$

where E_f is the binding energy of a single electron in the f -orbital, U_{ff} is the Coulomb repulsion energy between electron pairs in the f -shell, e_k represents the

energy of an electron in the d -shell of wave vector k , and n represents the number of electrons in the shell with spin index α or β . One is now able to calculate an effective single occupancy f -level width due to the promotion of localized electrons into the conduction band, below the Fermi level, or from the $4f^1 \rightarrow 4f^2$ transition above the Fermi level. The width (Δ) is given by

$$\Delta = \pi |V_k|^2 N(0) \quad (1.14)$$

Anderson was then able to show, working in the Hartree-Fock approximation, that the impurity ions are capable of developing a magnetic moment in the metallic host matrix as long as the Coulomb repulsion $U_{ff} \gg |V_K|$, guaranteeing single occupancy of the f -shell. It was later shown that these moments are coupled to the spin polarization of the conduction electrons via an antiferromagnetic exchange interaction (J), and this coupling introduces fluctuations in the directions of the local moments [49]. The exchange J is related to the f - d hybridization matrix element V_K and the f -shell binding energy E_f by

$$J \propto \frac{|V_K|^2}{E_f} \quad (1.15)$$

As the temperature is decreased there is a crossover from high temperature local moment behavior to a low temperature reduced moment state. This "transition" is characterized by a transition temperature (T_K). The reduction, or compensation, of the local moments occurs through the formation of a conduction electron "cloud" surrounding the impurity spin and forming a so-called virtual bound state. This is understood as the well known Kondo effect and allows us to understand

the mechanism of moment reduction [50]. However, in order to explain the large density of states at the Fermi level in HF compounds, a method for solving the Anderson model was developed and modeled to try to understand existing XPS spectroscopy data [51]. The results of these calculations included a large resonant peak in the density of states, known as the Kondo or Abrikosov-Suhl resonance, centered at temperature T_K just above the Fermi energy. The width of this resonance is inversely proportional to $N(0)$.

In the low temperature limit, data suggest that HF compounds enter into a Fermi liquid state below some characteristic temperature (T^*). The phenomenological Fermi liquid theory of Landau has been used to describe simple metals as well as HF compounds [52]. It is not obvious that treating a collection of interacting electrons as independent particles should produce a realistic description of these particles near the Fermi surface. This approach was justified by Landau who noted that if the independent electron picture was replaced by an independent quasiparticle picture, then the same arguments used for the independent electron scenario could be applied to the quasiparticle scheme and acquire more validity. In effect, a quasiparticle can be viewed as a single particle surrounded by a distortion cloud in the electron gas. Thus, we view a Fermi liquid as a system of interacting, "dressed" electrons. Utilizing the results from Landau's theory, the low temperature ground state of HF compounds can be described as a narrow band of heavy, itinerant, interacting quasiparticles. Properties such as the electron mass are renormalized due to the motion and distortion of the surrounding

particle cloud. The pertinent results of Fermi liquid theory are as follows:

$$\gamma = \frac{\pi^2 K_B^2 N(0)}{3} \quad (1.16)$$

$$N(0) = \frac{K_F m^*}{\pi^2 \hbar^2} \quad (1.17)$$

$$\chi = \frac{m^*/m}{1 + F_0^a} \chi^0 \quad (1.18)$$

$$\rho = \rho_0 + AT^2 \quad (1.19)$$

here, χ^0 is the susceptibility in the non-interacting system and F_0^a is a dimensionless Landau parameter.

From table 1.1 we observe a number of different HF ground states. The question arises as to which state will prevail at low temperature. The answer is due in large part to the magnitude of the exchange coupling J [53, 54]. The binding energy (W_k) of the moment reducing Kondo singlet is given by

$$W_k \sim \frac{e^{-1/N(0)J}}{N(0)} \quad (1.20)$$

The binding energy of the conduction electron mediated antiferromagnetic coupling between f -moments, known as the *RKKY* interaction, is

$$W_{RKKY} \sim J^2 N(0) \quad (1.21)$$

So there arises a competition between these two interactions. For large J we obtain a paramagnetic or reduced moment state. For small J a local moment-like state is favored.

As attractive as the Kondo and Fermi liquid approaches are, there are some serious problems with both models as they pertain to HF physics. First, it is clear that in HF systems we have a lattice of f -ion impurities, so the single-site Kondo model would have to be adapted to include the interactions between the impurities. Crystal field effects must also be taken into account. Second, a lattice of impurity spins affects the interactions between the itinerant electrons in the Kondo model. They effectively swim in a sea of compensated spins. The repeated interaction of the itinerant electron-hole pairs is capable of screening the interaction between partially compensated impurities, and the formation of enhanced spin fluctuations at low temperature is possible. Third, because the f -electrons are capable of jumping into and out of the conduction band, they are able to interact with and couple to the spin fluctuations, which leads to temperature corrections in thermal and transport properties. The main problem with applying Landau theory to the HF ground state lies in the fact that, unlike liquid ^3He , HF systems are intrinsically anisotropic as a result of the crystal lattice. So, the effective electron mass is no longer simply related to the quasiparticle interaction. The presence of spin-orbit coupling makes it difficult to specify the magnetic moment of the quasiparticles, as they are no longer directly related to the free electron moment. Most importantly, there arise significant non-quasiparticle contributions to the magnetic susceptibility, so measurements of the susceptibility cannot be related directly to the properties of the quasiparticles.

To summarize, the competition between the RKKY and Kondo interactions and the cross-over to an itinerant electron Fermi liquid state all combine to give rise to rather unconventional thermal and transport properties in HF compounds at

low temperature. The large effective mass, small resistivity, antiferromagnetic spin correlations and greatly reduced ordered moments, when taken together, are poorly understood. The emergence of superconductivity from this complex normal state is certainly unexpected, especially when we consider how the energy scales of true *BCS* and heavy Fermion superconductors differ. In a typical *BCS* superconductor the Fermi energy is much larger than the phonon energy ($K_B T_D \ll K_B T_F$). However in the heavy Fermion systems this is not the case since the large m^* implies a significantly reduced Fermi energy. The merging of these two energy scales implies that the standard *BCS* formalism may not be applicable to the heavy Fermion superconductors.

CHAPTER 2

PROPERTIES OF UBe_{13}

In this chapter we review the properties of the HF superconductor UBe_{13} . The first section covers normal state properties. The second section concentrates on the superconducting state. We focus on data obtained from thermal and transport property measurements, but information gained from other experiments is provided.

2.1 Normal State Properties of UBe_{13}

The HF superconductor UBe_{13} crystallizes in the cubic $NaZn_{13}$ structure, space group $Fm\bar{3}c$, Pearson symbol $cF112$ [55, 56, 57, 58]. The lattice constant of polycrystalline material has been determined from neutron scattering data to be 10.2602 Angstroms at 250K [59, 60]. Each unit cell contains 8 formula units, with 2 inequivalent *Be* sites (*BeI* and *BeII*). There are 8 *BeI* sites and 96 *BeII* sites per unit cell. The nearest neighbor $U-U$ distance is 5.1301Å, while the nearest neighbor $U-BeII$ distance is only 3.1Å. Thus direct $U-U$, $5f-5f$, overlap is almost absent and $U-5f$ hybridization with the *Be s* and *p* orbitals is dominant. The structure is shown in figure 2.1 [61]. By using the available crystallographic data we have been able to calculate the volume of the atomic *BeI* and *BeII* sites.¹ The *BeI* site volume is ~ 25 Angstroms³ while the *BeII*

¹We are indebted to Dr. Mike Jones for his assistance in these calculations.

site volume is $\sim 18 \text{ Angstroms}^3$. This 35% difference in site volumes will play an important role in the following (chapter 5) discussion of our results. We now review some interesting normal state results for this compound.

2.1.1 Normal State Specific Heat

The normal state specific heat of single crystalline, annealed UBe_{13} (sample #T2) is presented in figure 2.2. The data reveal an anomaly centered around 2.5K. The entropy of this anomaly has been calculated to be on the order of $1J/(mole - K)$ [7]. A fitting procedure performed in terms of the spin(1/2) Kondo impurity model resulted in large discrepancies, which were attributed to “coherence effects” [62]. However, fitting the f -electron contribution to the specific heat (ΔC_f) to a standard 2-level Schottky scheme gives excellent results [63]. The success of this approach suggests that about 5% of the U ions are involved in a multilevel system split by $.6meV$. Neutron studies have found no evidence for a resonance which would correspond to ΔC_f [59]. The effects of substitutional impurities on the 2.5K anomaly have also been studied [63]. When doped (on the U site) with elements smaller than U (leading to a contraction of the lattice) the anomaly is shifted up in temperature. Doping with elements which expand the lattice suppresses the anomaly and shifts it to lower temperatures. So it appears that UBe_{13} possesses a multi-level Schottky system superimposed on a non-magnetic, normal ground state. There is increasing evidence which relates this 2.5K anomaly to the presence of f -electron correlations, or spin fluctuations [61]. The presence of these fluctuations adds another energy scale to the UBe_{13} ground state and may play an important role in the lower temperature superconducting transition.

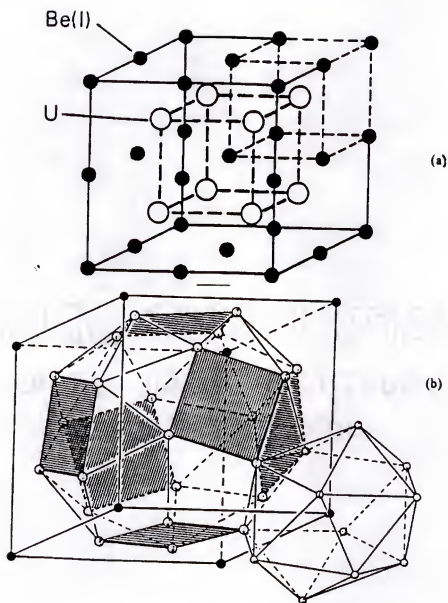


Figure 2.1: The structure of the UBe_{13} unit cell [61]. In (a) the $Be(II)$ atoms have been omitted for clarity. In (b) the closed circles represent $Be(II)$ atoms and are shown surrounding a U atom site (not shown). The open circles are $Be(I)$ atoms. Also shown is $Be(II)$ icosahedron surrounding one of the $Be(I)$ atoms.

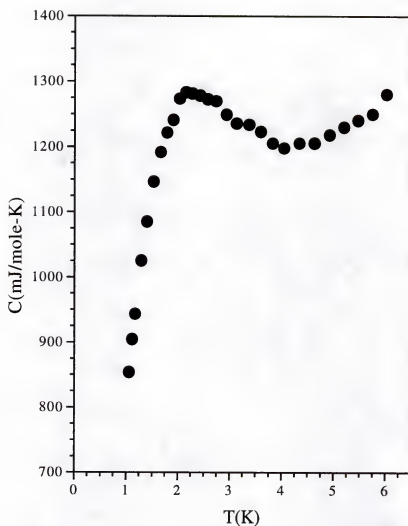


Figure 2.2: The high temperature specific heat vs. temperature for a standard UBe_{13} single crystal. The entropy under this anomaly approaches 1 Joule/mole-K . After subtracting a suitable phonon background, the remaining f -electron contribution to this anomaly may be modeled after a two level Schottky scheme in which only a fraction of the U ions contribute to the split level system.

Above 20K, reports indicate the presence of a broad Schottky peak centered at 70K [62]. This is attributed to a first excited crystal field level at 150K-180K. These data also provide further evidence that the U ions are in the $5f^3$ (U^{3+}) configuration.

2.1.2 Resistivity

The resistivity (ρ) of UBe_{13} from 1-290K is shown in figure 2.3. From a large room temperature value of $130\mu\Omega\text{-cm}$, the data exhibit a Kondo-like increase with decreasing temperature until a local maximum is reached around 25K. This broad shoulder is thought to be due to a combination of crystal field splitting and a Kondo effect [64]. Crystal field states are expected due to the existence of a large Schottky anomaly centered at 70K. The presence of the Kondo effect seems to broaden the shoulder and shift it to the lower temperature of 25K. These claims are supported by evidence from doping experiments which show a disappearance of the anomaly with increased U $5f$ - Be sp hybridization and a shifting to higher temperatures with decreased hybridization [65]. As the temperature decreases further, we reach a maximum around 2.5K. This maximum is thought to be due to the onset of coherence, the presence of spin fluctuations, or the presence of a two-level Schottky ground state [65, 66, 63, 61, 67, 68, 69, 70]. The interaction of the U $5f$ electrons with the conduction electrons leads to the formation of massive quasiparticles, and the system appears to approach a Fermi liquid-like state. Only minor amounts of impurities are required to suppress this 2.5K peak [71]. The decrease in ρ below 2.5K is eventually interrupted by the onset of superconductivity at .9K. At T_c the resistivity is on the order of $100\mu\Omega\text{-cm}$. The resistivity is extremely pressure and

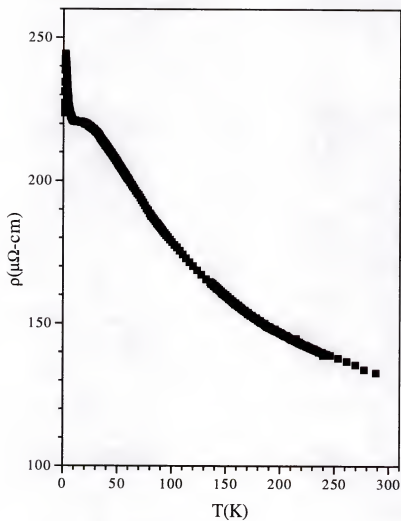


Figure 2.3: The resistivity vs. temperature for UBe_{13} . Note the broad shoulder centered around 25K and the peak at 2.5K. This peak is thought to be due to the onset of coherence.

magnetic field dependent [72, 73, 74, 75, 76, 77]. As the temperature is lowered the large, negative magnetoresistance ($\Delta R = R(H, T) - R(0, T)$) approaches 0. Thus since $\Delta R=0$ at $T=0$, then $R(0,0)$ (the residual resistivity) is taken to be equal to the high field limit of $\sim 18\mu\Omega\text{-cm}$. There is no tendency for saturation by 10T. It is also known that the normal state resistivity is reduced via application of pressure, which affects the interatomic spacing but not the number of conduction electrons, as would chemical substitution. Data indicate an intrinsic resistivity of $\sim 18\mu\Omega\text{-cm}$ is reached in magnetic fields up to $\geq 9T$ and that this value is pressure independent. Taken together with the dramatic drop in the resistivity from room temperature the low temperature scattering in UBe_{13} is believed to be predominantly inelastic with little contribution from lattice imperfections.

The magnetoresistance of UBe_{13} is also very interesting. The maximum of the low temperature anomaly is seen to increase quadratically with field and is eventually destroyed by high fields. A scaling relation which applies equally well to single as well as polycrystalline material indicates that neither the periodic Kondo lattice model nor the single impurity Kondo model are applicable to this system [78]. The scaling also indicates the presence of ferromagnetic correlations, an unexpected result. Scaling of the magnetoresistance curves from 1-15K leads to the following relation:

$$\frac{\Delta R}{R(0, T)} = \frac{(T - .75K)^6}{H} \quad (2.1)$$

where H is the applied field strength in T . We also note that the magnetoresistance remains negative down to the lowest temperatures measured to date. This also

argues against a Kondo lattice approach to understanding this system. Measurements of the magnetoresistance under pressure have shown that the large negative values of ΔR persist up to 19Kbar. The strong effects of magnetic field and pressure on the resistance of UBe_{13} also suggest that a decrease of the heavy electron mass is accompanied by an increase in the temperature range in which Fermi liquid effects are observed ($\rho \propto T^2$).

2.1.3 Magnetic Susceptibility

The magnetic susceptibility (χ) of UBe_{13} from 1.8 to 300K is shown in figure 2.4. In the low temperature limit χ approaches 15 *memu/mole*. This is a truly enormous value when compared to that of *Pd* (.75 *memu/mole*), which possesses the largest χ of all non-magnetic elements. As we mentioned in section 1.1.2, the dramatic low temperature increase in χ is mirrored by a similar increase in the low temperature specific heat coefficient γ , indicating the entry into a large effective mass, itinerant-electron ground state. Doping experiments have shown that the magnetic susceptibility per *U* mole is independent of the *U* ion concentration [79]. Thus single-ion effects play a key role in the ground state of UBe_{13} . Looking now at the inverse susceptibility (χ^{-1}) versus temperature in figure 2.5, we immediately notice the linear, Curie-Weiss high temperature region extending from $\sim 100 - 300K$. This is an indication of local moment behavior. A linear extrapolation of the high temperature data [80] yields an effective moment of $3.40\mu_B$ and a Curie-Weiss temperature (Θ_{CW}) of -70K.

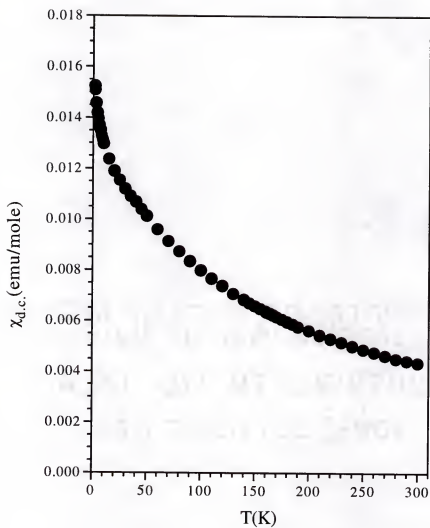


Figure 2.4: The magnetic susceptibility vs. temperature for UBe_{13} . Note the enormous value of $\chi_{d.c.}$ as $T \rightarrow 0K$.

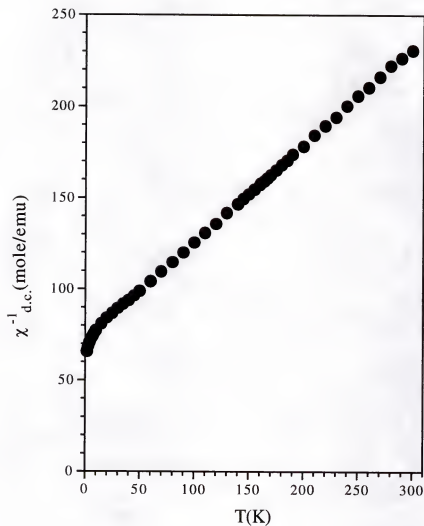


Figure 2.5: The inverse magnetic susceptibility vs. temperature for UBe_{13} . The linear region above 100K suggests local moment behavior. A linear extrapolation of this region indicates the presence of anti-ferromagnetic correlations. This description clearly breaks down as T approaches 0K.

2.1.4 Neutron Scattering

The scattering of neutrons from the atomic nuclei of a crystalline lattice provides for highly accurate determinations of structural parameters as well as phonon and magnetic spectra. Such studies have been performed on polycrystalline UBe_{13} [59, 60]. The results indicate that the lattice parameter of UBe_{13} increases smoothly with temperature and reaches a value of 10.2602 Angstroms by 250K. A significant amount of static disorder has also been observed and is associated with the atoms on the $Be(II)$ sites. Inelastic results taken at 10K have revealed a broad scattering spectrum which nearly accounts for all of the observed bulk magnetic susceptibility. To date, quasielastic results have given no indication of the narrow f -level resonance associated with the heavy f -electron ground state. Since the HF ground state is characterized by an extremely narrow resonance located slightly above the Fermi energy, the failure to detect this resonance is due to the inability to achieve the required experimental resolution.

2.2 Superconducting Properties of UBe_{13}

Superconductivity in UBe_{13} was first observed in 1975 [81]. Unfortunately the results were attributed to precipitated U filaments and not to bulk superconductivity. It was not until 1983 that a bulk superconducting transition was confirmed via low temperature specific heat measurements, thus making UBe_{13} the second HF superconductor known at that time [14]. In this section we discuss results obtained from experiments designed to probe UBe_{13} at temperatures below T_c .

2.2.1 Superconducting Length Scales

Determinations of mean free path (l), coherence length (ξ), and penetration depth (λ) provide us with information concerning the energy gap structure, density and effective mass of the superconducting electrons, and type (I or II) of the superconductor under investigation [39]. We may write the penetration depth as

$$\lambda(T) = \left(\frac{\epsilon_0 m c^2}{n(T) q^2} \right)^{1/2} \quad (2.2)$$

for particles of mass m , charge q and concentration n . ϵ_0 is the permittivity of free space ($10^7/4\pi^2$) and c the speed of light ($3 \times 10^8 m/s$). The coherence length is given by

$$\xi = \frac{2\hbar v_F}{\pi E_g} \quad (2.3)$$

where v_F is the Fermi velocity and E_g the energy gap. Precise measurements of the mean free path for UBe_{13} are rather uncertain due to the large temperature dependence of the resistivity near T_c [82, 83]. A value on the order of 100 Angstroms is generally accepted. Due to the large room temperature resistivity of $\sim 130 \mu\Omega\text{-cm}$, it seems appropriate to base length scale calculations in the “dirty” limit, where $l < \xi$. Calculations of ξ in the dirty limit yield a value of ~ 140 Angstroms [82]. The zero temperature penetration depth has been measured to be between 2000-11000 Angstroms [84, 85]. A calculation of the Ginzburg-Landau parameter ($\kappa = .96 \cdot \lambda(0)/\xi$) in the dirty limit gives a result on the order of 100 and indicates that UBe_{13} is a strong type II superconductor.

2.2.2 Upper Critical Magnetic Field

The upper critical magnetic field (H_{c2}) of UBe_{13} has been measured extensively [82, 86, 73, 76, 87, 88] and is shown in figure 2.6 [89]. Below 6T the results for single and polycrystalline material are similar and give an initial slope (H'_{c2}) of between 40-50T/K. Above 6T the temperature dependence of H_{c2} clearly differs between the 2 sample types. The single crystalline data indicate a leveling off above 6T and a zero temperature limit ($H_{c2}(0)$) approaching 9T, while the slope of the polycrystalline sample actually increases with increasing field. The large values of H'_{c2} and $H_{c2}(0)$ in both sample types may indicate the presence of strong spin-orbit scattering and very massive electrons. The occurrence of Pauli limiting has also been theorized in order to explain the unusual curvature and saturation for single crystalline material. It has been suggested that sample quality and the method used to analyze the raw data (resistive mid-point or onset, for example) are factors which influence the saturation of $H_{c2}(T)$ and the curvature near T_c . By incorporating the effects of strong coupling, a model has been applied successfully to the UBe_{13} $H_{c2}(T)$ curve which takes into account both the positive curvature at $\sim 6T$ and the violation of the Clogston Pauli limit. The coupling parameter obtained is extremely large, although the exact nature of the coupling is as yet unknown. A non-uniform (*FFLO*) superconducting state appearing below .4K is also postulated from the proposed simple model. Several groups have investigated the possibility of anisotropy in $H_{c2}(T)$ [87, 90, 91]. The best evidence to date suggests that $H_{c2}(T)$ is isotropic in the limit $T/T_c \rightarrow 1$. As the anisotropy of the Fermi surface is rather small in various metals, an energy gap of the same symmetry would also show little anisotropy. For cubic systems, as $T/T_c \rightarrow 1$,

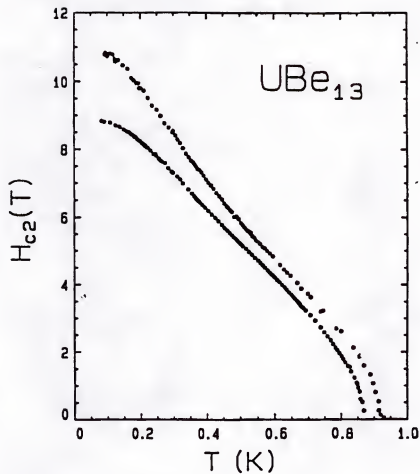


Figure 2.6: The upper critical magnetic field vs. temperature for single (lower curve) and polycrystalline (upper curve) UBe_{13} [89]. Note that the single crystalline data appear to level off with increasing field, while the slope of the polycrystalline data actually increases with field above 6T.

$H_{c_2}(T)$ is always isotropic for a conventional superconductor. Thus the lack of any measurable anisotropy in $H_{c_2}(T)$ for UBe_{13} is an inconclusive result as far as the unconventional nature of the superconducting state is concerned.

2.2.3 Specific Heat

The low temperature specific heat (C) of an annealed single crystalline sample of UBe_{13} (sample #2A) is shown in figure 2.7. The superconducting transition at T_c leads to a sizeable discontinuity (ΔC_{T_c}) which is comparable in magnitude to the specific heat at T_c (C_{T_c}). We can easily calculate for this crystal that $\Delta C_{T_c}/C_{T_c} = 1.83$. This indicates two important points. First, since $\Delta C_{T_c} \propto C_{T_c}$ we know it is the heavy electrons which are superconducting. Second, the value of 1.83 is greater than the BCS weak coupling limit of 1.43 and implies strong coupling effects are dominant in UBe_{13} . Another parameter of interest is the value of C/T as $T \rightarrow 0$. This is known as the Sommerfeld coefficient ($\gamma(0)$). Since we are working with a second order phase transition, the superconducting and normal state entropies must be equal at T_c [8]. To determine the correct entropies and obtain $\gamma(0)$, an equal area entropy construction is performed. The result of this procedure is shown in figure 2.8, and is performed in the following way. The high temperature data ($T > T_c$) is linearly extrapolated to $T \sim T_c$. Superconducting data below T_c is extended beyond the experimental peak. Next, an idealized (vertical) transition is postulated and placed in between the normal and superconducting extrapolations. By requiring that the superconducting entropy added to our idealized transition is equal to the normal state entropy subtracted from it, the critical temperature of the idealized transition is determined. Having done this we may now calculate

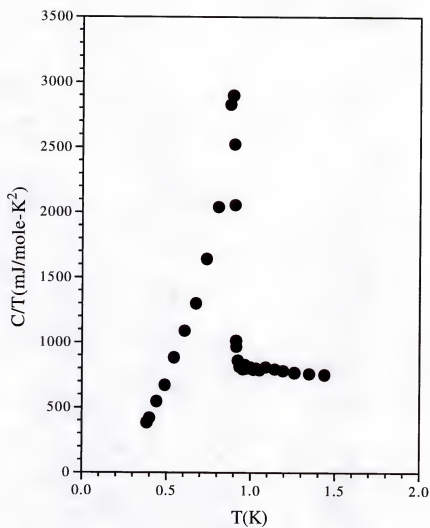


Figure 2.7: The specific heat divided by temperature vs. temperature for standard UBe_{13} single crystal 2A. This sample was annealed for 6 months at 1000°C .

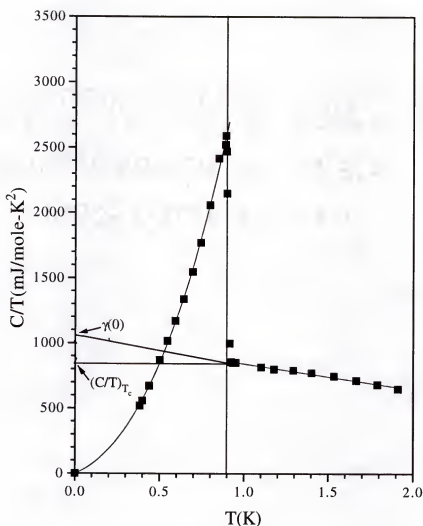


Figure 2.8: The specific heat divided by temperature vs. temperature for standard UBe_{13} single crystal 2A used to construct an equal entropy plot. The normal state entropy obtained from integrating a constant C/T below T_c ($(C/T)_{T_c}$) is insufficient to achieve entropy balance at T_c . To remedy this, a new linear extrapolation below T_c is performed such that the new normal state entropy equals the superconducting entropy at T_c . In this way entropy balance is achieved and the true value of C/T as $T \rightarrow 0$ ($\gamma(0)$) is calculated.

the superconducting and normal state entropies (S_{sc} and S_n respectively) via

$$S_{sc} = \int_0^{T_c} (C/T)_{sc} dT \quad (2.4)$$

$$S_n = \int_0^{T_c} (C/T)_n dT \quad (2.5)$$

The normal state entropy is calculated assuming the specific heat is independent of temperature below T_c . Superconducting data below our lowest available temperature ($\sim .35K$) is postulated with a linear extrapolation from 0K to the first low temperature data point. The error introduced into S_{sc} by this method is roughly 3%, which we take as our absolute error for our entropy calculations. The results for this crystal, and all UBe_{13} samples with a $T_c \sim .9K$ analyzed in a similar manner, indicate an entropy mismatch at T_c with $S_{sc} > S_n$ by about +9%. This is ~ 3 times our estimated uncertainty in S calculated in this way. To remedy the situation a new linear extrapolation of the normal state data is incorporated below T_c to increase S_n by the required amount. Once the equality of the entropies has been established the values of $C/T(T_c)$ and $\gamma(0)$ (the adjusted value necessary to conserve entropy) are easily read off of the plot. With $\gamma(0)$ we are then able to calculate a more physically relevant coupling parameter (β) given as $\Delta C_{T_c}/(\gamma(0) \cdot T_c)$. We list some important parameters for this crystal in table 2.1. It should be noted that variations in sample quality preclude assigning a definitive value to any of the parameters listed for all UBe_{13} samples. Note the range of values for the given parameters in this table. However, the large values of $\gamma(0)$, $\Delta C_{T_c}/C_{T_c}$ and the positive entropy mismatch are common features to all pure ($T_c \sim .9K$) UBe_{13} samples measured to date [92, 93].

Table 2.1: Specific heat parameters for UBe_{13} annealed single crystal standard #2A and a polycrystalline sample [94].

Compound	T_c (K)	ΔC_{T_c} $\frac{mJ}{(mole-K)}$	$\Delta C_{T_c}/\gamma(0) \cdot T_c$	$C/T(T_c)$ $\frac{mJ}{(mole-K^2)}$	$\gamma(0)$ $\frac{mJ}{(mole-K^2)}$	$\Delta S(\%)$ $\frac{(S_{sc}-S_n)}{S_{sc}}$
UBe_{13} #2A	.905	1705	1.83	852	1031	+9%
UBe_{13}	.82	1582	1.62	941	1190	+18%

The behavior of the superconducting transition upon doping with La , Y , and Th on the U site is rather interesting and presented in figure 2.9 [95, 96, 79, 97, 98, 99]. Here, T_c vs. ΔC_{T_c} for doped and pure (T_{c0} and $\Delta C_{T_{c0}}$) UBe_{13} are plotted in reduced coordinates. Dilute concentrations of non-magnetic impurities are just as effective at breaking up the Cooper pairs and reducing T_c and ΔC_{T_c} as are magnetic impurities. The effect of magnetic impurities on conventional s -wave superconductors is well known and indicated by the curve “ $A - G$ ”, for Abrikosov and Gor’kov, in the figure [100]. The sensitivity of UBe_{13} to non-magnetic impurities, a class into which La , Y , and Th may be grouped due to the large spatial extent (and subsequent hybridization with the conduction electrons) of the valence electrons of these elements, is taken as evidence for a non- s -wave (anisotropic) pairing state. Two special dopants are Th and B .

When doped with Th , T_c behaves non-monotonically as a function of Th concentration (x) [101, 43, 102]. For $U_{1-x}Th_xBe_{13}$, with $.019 \leq x \leq .043$, two specific heat transitions occur, as seen in figure 2.10. The existence of magnetic correlations associated with the second transition has been confirmed and a local moment of $\sim .001\mu_B$ established [103, 104]. Data on the pressure dependence of T_c for the

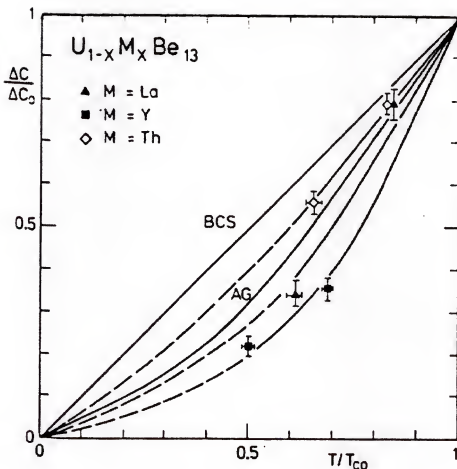


Figure 2.9: The behavior of UBe_{13} upon doping on the U -ion site as viewed in reduced coordinates [98]. Note the dramatic drop in T_c for all doped samples, and that this effect does not depend on whether the dopant is magnetic or non-magnetic. The straight line is the so called *BCS* law of corresponding states. This is a similarity principle which holds that within the basic *BCS* model, the similarities between superconducting phases far outweigh the differences. The curve labeled “A-G”, for Abrikosov-Gor’kov, is the theoretical behavior one would expect from a conventional *s*-wave superconducting state doped with magnetic impurities.

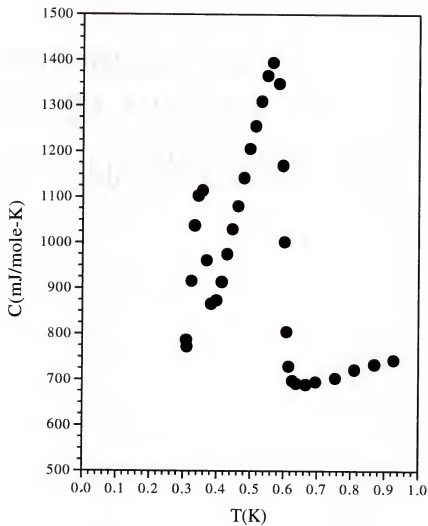


Figure 2.10: The specific heat vs. temperature for $\text{U}_{97}\text{Th}_{03}\text{Be}_{13}$. Note the two transitions. Although magnetic correlations have been detected below the second transition, all evidence to date suggests that both peaks are superconducting.

second transition (at T_{c2}) indicate that it is superconducting, and not magnetic in origin [105]. Also, an abrupt change in the slope of the lower critical field occurring at T_{c2} is an indication of a marked increase in the Cooper pair density below T_{c2} [104]. Further evidence for two superconducting transitions in *Th* doped UBe_{13} comes from measurements of H_{c2} [106]. The data clearly show that H'_{c2} as $T \rightarrow T_c$ is identical for both transitions. Thus there is strong experimental evidence for two superconducting transitions, and this may be the best evidence to date for truly unconventional superconductivity in this compound.

Boron has quite an unexpected effect on the specific heat, and data is presented in figure 2.11 for polycrystalline $UBe_{12.97}B_{.03}$ [94]. An equal area entropy construct, as discussed in section 2.2.3, allows us to compare several important parameters of this sample with those of pure UBe_{13} . The results are presented in table 2.2. The fact that ΔC_{T_c} and $\Delta C_{T_c}/(\gamma(0) \cdot T_c)$ are significantly enhanced

Table 2.2: Specific heat parameters for UBe_{13} and $UB_{.03}Be_{12.97}$ [94].

Compound	T_c (K)	ΔC_{T_c} $\frac{mJ}{(mole-K)}$	$\Delta C_{T_c}/\gamma(0) \cdot T_c$	$C/T(T_c)$ $\frac{mJ}{(mole-K^2)}$	$\gamma(0)$ $\frac{mJ}{(mole-K^2)}$	$\frac{\Delta S(\%)}{(S_{sc}-S_n)}$ S_{sc}
UBe_{13}	.82	1582	1.43	941	1350	+18%
$UB_{.03}Be_{12.97}$.79	3991	3.27	1120	1550	-2%

for the *B* doped sample while T_c remains relatively unchanged is quite remarkable. One possible explanation put forth is that the addition of *B* alters the strong coupling parameter (T_c/ω_0) by decreasing the frequency (ω_0) of the bosonic pair mediating interaction [94]. A change in the symmetry of the superconducting state due to inelastic impurity scattering has also been suggested. This was interpreted

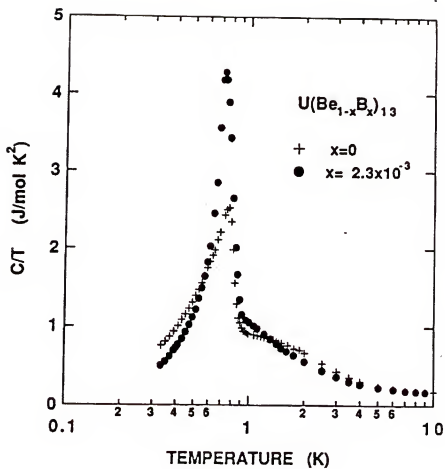


Figure 2.11: The specific heat divided by temperature vs. temperature for pure and B doped UBe_{13} [94]. Note that while ΔC_{T_c} is greatly enhanced for the B doped sample, T_c remains equal to that of the pure material.

as a change in the nodal structure of the (probable) anisotropic energy gap. Further evidence for this lies in the fact that the low temperature specific heat evolves from an approximately T^3 temperature dependence in pure UBe_{13} to a T^2 dependence in the B doped sample. No magnetic excitations have been detected in the B doped compound [107], although it is important to note that the correlation, or Kondo, temperature associated with the normal state specific heat is shifted to lower temperatures as ΔC_{T_c} is enhanced. Thus by considering the experimental properties of UBe_{13} , we see that this is an interesting superconducting compound that is not well understood.

CHAPTER 3

MOTIVATION

The motivation for this study is presented in figures 3.1 and 3.2. The data in figure 3.1 show the low temperature specific heat for two different single crystalline UBe_{13} samples (sample *R1* [108] and sample *2A* discussed previously). Both samples were grown by the *Al* flux growth technique. Note that an enhanced superconducting transition, similar to that of sample *R1*, has been observed previously [109].

The superconducting properties of these samples clearly differ in at least two ways. First, the transition temperature T_c of *R1* is greatly reduced from $\sim .9K$ to $\sim .75K$. Second, the discontinuity at T_c is significantly enhanced for this crystal. What is the cause of the reduced T_c and the enhanced ΔC in this novel single crystal of UBe_{13} ? Is this an impurity effect, structural effect, or both? Is this strictly a single crystalline phenomenon or may the results be duplicated for polycrystalline material? A series of experiments were designed and carried out to address these hypotheses and to attempt to elucidate the nature of this new, novel, ground state of UBe_{13} . We present our results in chapter 5.

During the course of this investigation, analysis of magnetic susceptibility data revealed an interesting transition in χ in some UBe_{13} single and polycrystalline samples. This is shown in figure 3.2. Thus as an offshoot to the main project at hand we have also investigated this anomaly and have attempted to understand whether it is magnetic or structural in nature, and what relationship, if any, exists

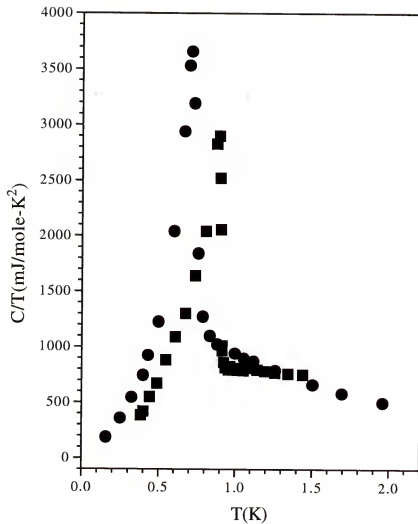


Figure 3.1: The specific heat divided by temperature vs. temperature for anomalous single crystal R1 [108] of UBe_{13} (circles) and a standard single crystal 2A (squares). Note the reduced T_c and enhanced ΔC_{T_c} for the anomalous crystal. The Big-Jump-Low- T_c (BJLT) behavior will be investigated in this study.

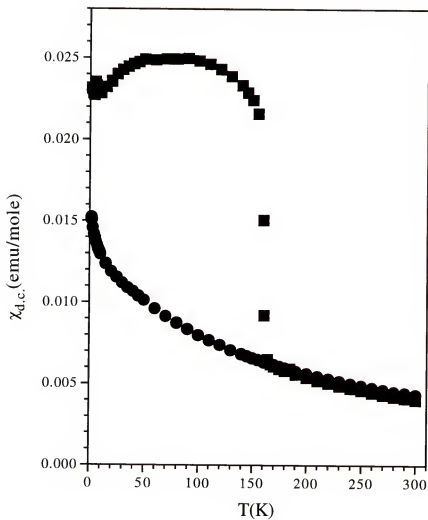


Figure 3.2: The magnetic susceptibility vs. temperature for an anomalous single crystal of UBe_{13} (squares) and a standard high purity polycrystal 9P (circles). Note the onset of a ferromagnetic-like anomaly at 160K in the single crystalline data.

between this anomaly in χ and the novel superconducting transition described above.

CHAPTER 4

EXPERIMENTAL METHODS

In this chapter we describe the various sample preparation and data gathering techniques used in this study.

4.1 Preparation of Polycrystalline Samples

Polycrystalline samples of UBe_{13} and UM_xBe_{13-x} , where M is a substitutional element specified in the text, were prepared by arc-melting together U (99.9% pure), Be (99.8% pure) and M (typically 99.99% pure) in a Zr gettered purified Ar gas atmosphere. The Be used was Be “scrap” from Atomergic corp. The U was obtained from Cameco corp or Los Alamos laboratory (Phil Armstrong U). High purity samples were prepared with 99.99% pure electro-transport refined U from Ames laboratory and 99.999% pure zone refined Be . Due to the large vapor pressure of Be , 6% excess Be was added at the beginning of the melt to allow for Be loss. Samples were melted once, flipped over, and melted a second time to ensure homogeneity.

4.2 Preparation of Single Crystalline UBe_{13}

All UBe_{13} single crystals were grown via an Al flux growth technique [110]. The presence of the Al lowered the melting point of UBe_{13} from over $2000^{\circ}C$ to less than $1400^{\circ}C$ which enabled us to obtain a homogeneous liquidous melt at a

temperature of 1400°C . The amount of starting material was determined by the percentage of UBe_{13} desired. Typically, 4-6% UBe_{13} was seen to produce copious amounts of sizable single crystals. The starting materials were loaded into a small BeO crucible and covered with a BeO lid. This crucible was then placed into a Ta tube. The Ta tube was placed in a purified Ar atmosphere and sealed by arc-melting a Ta lid to the top. After sealing, the Ta tube was placed into the center of an alumina tube which ran the length of a computer controlled Lindberg furnace. The ends of the tube were capped and sealed in such a way as to allow a continuous flow of Ar gas to flow over the Ta tube throughout the growth process. The temperature of the oven was ramped up at a rate of 75°C/hr until 1400°C was reached. Once stabilized, the temperature was held constant for typically 5 hours, depending on the specs desired for the particular batch of crystals being grown. After this time had elapsed, the temperature was ramped down to 1000°C at a rate of $10 - 15^{\circ}\text{C/hr}$, which was also batch dependent. By 1000°C UBe_{13} crystals had grown from the melt and a cooling rate of 75°C/hr was employed to bring the oven back to room temperature. To remove the as-grown single crystals from the Al flux, the contents of the BeO crucible were immersed in a solution of KOH and H_2O .

4.3 Annealing

The effects of annealing on T_c and ΔC for UBe_{13} can be dramatic, and it is important to avoid any mass loss during the procedure to retain the unannealed sample's stoichiometry. Each sample was placed in a new, outgassed BeO crucible. The underside of this crucible contained a small ($10 - 15\text{mg}$) piece of Be which

served as a source of *Be* vapor during the annealing process. This small *BeO* crucible was then placed inside a larger *BeO* crucible which was capped with a *BeO* lid. The entire sample, vapor source, crucible unit was set inside a *Ta* tube and sealed, via arc-melting, in a purified *Ar* gas atmosphere. As was the case for preparing single crystalline specimens, the *Ta* tube was inserted into an alumina process tube and placed in the center of a computer controlled furnace. The temperature and length of time for annealing were variable and will be given explicitly for each sample presented.

4.4 Measurement of Specific Heat

The importance of accurate specific heat data for determining quantities such as T_c , ΔC , and entropy (S) cannot be overemphasized. Specific heat data was gathered in two temperature regions. The first region was from $\sim .35K \rightarrow 1.5K$ and the second from $1.5K \rightarrow 6K$. The thermal relaxation technique was used in both regions. The details of this method may be found elsewhere [111, 112, 113]. We would like to emphasize a few important points here.

Once the cryostat and sample reached a stable equilibrium temperature T_0 power was applied to the sample platform heater, increasing the sample temperature by an amount ΔT above the cryostat block (or reservoir) temperature T_0 . Power to the heater was then turned off and the sample temperature decayed exponentially according to

$$T(t) = T_0 + \Delta T e^{-t/\tau_1} \quad (4.1)$$

where τ_1 was the time constant of the sample and platform, and was a measure of the time to reach thermal equilibrium. Heat was conducted from the sample platform to the cryostat reservoir through 1-4 $Au - Cu$ wires, depending on the platform used (see below). τ_1 was obtained by plotting the off-null signal of a lock-in amplifier galvanometer as a function of time. This was then converted to a logarithmic plot of signal versus time and τ_1 was read off as the slope of the decay curve. The specific heat at temperature $T_0 + \Delta T/2$ was obtained via

$$C_T(t) = K\tau_1 \quad (4.2)$$

with K equal to the thermal conductance of the $Au - Cu$ wires and C_T equal to the specific heat of the entire sample/platform unit. The contribution of the platform and linking wires to the total specific C_T was then subtracted from C_T to obtain the specific heat of the sample C_s . The absolute accuracy of this method was $\pm 5\%$.

4.4.1 The Sample Platforms

At very low temperatures the specific heat of UBe_{13} is very large due in part to the significant superconducting transition at T_c . Thus it was advantageous to use a sample platform of large conductance to reduce the time constant of the temperature decay. The platform used for the low temperature portion of this study is presented in figure 4.1.

A 3/8" diameter Al_2O_3 disk was suspended in the center of a 1" diameter Cu ring by 5 supporting wires. The Cu ring was screwed directly to the cryostat

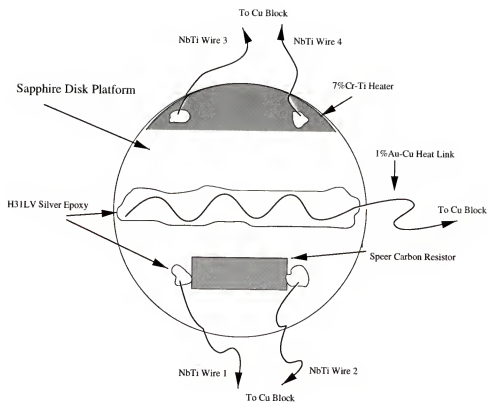


Figure 4.1: The low temperature platform used in this study.

block which was kept at equilibrium temperature T_0 . Wires 1-4 in figure 4.1 were superconducting $NbTi$ with the center portion of the Cu matrix removed to prevent any heat flow from the platform to the ring. Wires 1 and 2 were used to measure the resistance of the Speer carbon resistor which served as platform thermometer, and wires 3 and 4 were used to carry current to the platform heater. The platform heater was a strip of evaporated $7\%Ti - Cr$ alloy. Wires 1-4 were attached to the platform with H31LV silver epoxy obtained from Epo-Tek corp. Heat was conducted from the platform to the ring by the addition of a $1\%Au - Cu$ wire which was silver epoxied over the length of the platform and pressed into the Cu ring, providing direct metal to metal contact. Once constructed, the platform was calibrated as follows. First, the Speer thermometer resistance was measured as a function of temperature and calibrated against a Ge thermometer obtained from LakeShore cryogenics. Then, the conductance of the $1\%Au - Cu$ heat link was also measured as a function of temperature. The specific heat of a 99.9999% pure Au standard obtained from NIST was measured to verify the accuracy of the calibrations.

Above 1K the specific heat of UBe_{13} is substantially reduced, so a standard 4-wire high temperature platform was used to obtain data from 1-6K. The design of this platform is very similar to the low temperature platform and is shown in figure 4.2. Wires 1-4 were all $7\%Au - Cu$ alloy and served as the heat link from platform to ring. The platform thermometer was a commercially available Ge chip thermometer obtained from LakeShore Cryogenics. This platform was calibrated in the same manner as the low temperature platform, and checked with the NIST Au standard.

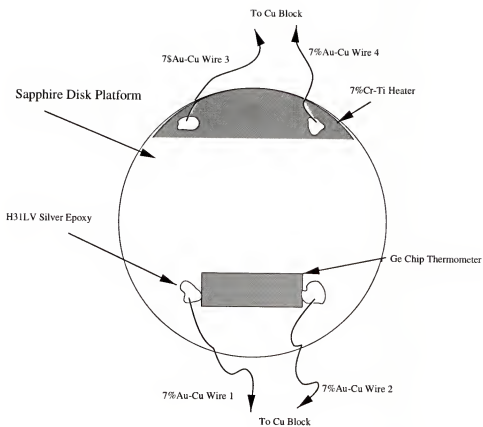


Figure 4.2: The high temperature platform used in this study.

4.4.2 Cryostats

Two cryostats were used in this study [114]. Both were initially placed in a ^4He bath to obtain a temperature of 4.2K. To reach 1.5K for the high temperature (HT) probe, the ^4He bath was pumped directly, while for the low temperature (LT) probe only an inner ^4He pot was pumped. To reach $\sim 35\text{K}$ in the LT probe a rod of activated charcoal was placed above an inner ^4He reservoir and used as an absorption pump. This probe was also equipped with a Speer carbon resistor for block temperature readings, which allowed for measurement in magnetic field due to the small (known) field dependence of this material.

4.4.3 Specific Heat in Magnetic Field

Specific heat data in magnetic fields of up to 10T was obtained in a *CCL* magnet using the previously described LT probe. The relatively small magnetoresistance of the Speer carbon resistor was accounted for according to a standard prescription [115]. A NIST *Au* standard was measured in 0T and 10T and both results indicated $\pm 5\%$ accuracy.

4.5 Resistivity

D.C. resistivity was measured using a standard 4-probe technique. The voltage and current leads were spot welded directly to the samples. All samples were cut into rectangular bars of approximately 1mm^2 cross-section. Due to uncertainties in the dimensions of the bar and in the voltage lead separation, overall accuracy was $\pm 10\%$.

4.5.1 Resistivity in Magnetic Field

We measured ρ in magnetic fields of up to $14T$ in a *CCL* magnet. The temperature of the resistivity probe was measured with a LakeShore capacitance sensor, which was calibrated against a *Ge* resistance thermometer in $0T$. Drift in the calibration was checked between runs, and no drift was detected.

4.6 D.C. Magnetic Susceptibility and Magnetization

D.C. magnetic measurements were performed from 1.8 to 300K in a commercially available SQUID magnetometer from Quantum Design. Overall accuracy of the susceptibility was $\pm 3\%$.

4.7 Microprobe Microanalysis

Electron probe microanalysis (*EPMA*) is a method of quantitative chemical analysis sensitive to within .1 atomic percent. Prior to each measurement each sample underwent 3 stages of polishing. The first stage was a rough polish with #600 grit silicon-carbide sandpaper. The samples were then set, polished face up and flush with the surface, in a 3/4" diameter 1/2" long cylinder of a 2 component plastic adhesive obtained from Buehler Corp. Next, each sample was placed in contact with a rotating polishing wheel covered with a thin layer of 6μ diamond paste compound obtained from Leco Corp. The final polish was achieved through the use of 1μ diamond paste compound.

All EPMA measurements were performed at the University of Florida Major Analytical Instrumentation Center (MAIC) by Mr. Wayne Acree on a Jeol Super-

probe #733. A 1μ diameter electron beam at approximately 100nA and 15KeV was directed at the polished sample surface. The focused electron beam irradiated the sample surface and produced characteristic X-rays, secondary electrons and backscattered electrons. The characteristic X-rays were produced from an approximately spherical region 1μ in diameter just below the sample surface. They were detected via a wavelength dispersive spectrometer (WDS). The spectrometer consisted of 2 analyzer crystals, TAP and PET, of known atomic plane spacing d . The angle Θ between the incoming radiation and the crystal plane was known. Thus by rocking each analyzer crystal before each data point was taken and fixing it in the position Θ which produced the maximum diffracted intensity, the wavelength λ of the incident X-ray beam was easily calculated from the Bragg law:

$$2d \sin \Theta = \lambda \quad (4.3)$$

Once λ was calculated the elemental constituents of the sample were determined through Mosely's law:

$$\lambda = \frac{B}{(Z - C)^2} \quad (4.4)$$

where B and C are constants for each family of X-ray lines ($K_{\alpha}, L_{\alpha} \dots$) and Z the atomic number of the element. The diffracted X-rays were then detected by a gas-filled proportional counter, amplified, converted to a pulse and counted. In this way qualitative as well as quantitative information was gained. It should be noted that the proportional counter was sealed off from the rest of the system, and X-rays entering the counter first passed through a 7.6μ Be window before being analyzed. This resulted in the photoelectric absorption of a small percentage of

the impinging x-ray signal. The combination of the photoelectric absorption of the *Be* window and the restricted *d* spacings of the analyzer crystals combined to make direct analysis of *Be* X-rays extremely difficult. So a method known as “detection by difference” was employed. In this method all known contributions to the X-ray signal were subtracted from the total signal and the remainder was assigned to *Be*.

In order to view the arrangement of the constituent elements of each sample and to check for spurious phases, a back-scattered electron (BSE) micrograph was also taken. Since BSE production increases with increasing atomic number, heavier elements such as *U* were seen to produce a stronger signal than lighter elements such as *Al*. This is known as a compositional or atomic number contrast mechanism. The BSE image was exposed to film for visual inspection.

4.8 X-ray Diffraction

X-ray diffraction was used to probe sample quality, measure the lattice constant as a function of temperature, and to check for structural changes as a function of temperature. From the Bragg law (equation 4.3 in section 4.7) it is possible to derive an expression for the lattice plane spacing *d* in terms of the lattice constant (*a*₀) and the Miller indices (*h, k, l*). For a cubic crystal the result is

$$d = \frac{a_0}{\sqrt{h^2 + k^2 + l^2}} \quad (4.5)$$

Thus the intensity of the diffracted radiation is a maximum for those values of Θ and *d* which satisfied the Bragg law. The resulting pattern was indexed with the

proper Miller indices and the lattice constant determined. Any peaks in the diffraction pattern not associated with the majority structure present were attributed to secondary phases or structures and these phases were indexed as well.

Preliminary X-ray data was obtained on a Philips APD 3720 diffractometer using $Cu K_{\alpha}$ radiation at 40KeV and 20mA, with a wavelength of 1.54056 Angstroms. Samples were ground to a fine powder in a ceramic mortar, mixed with a binding agent of 1:7 collodion:amyl acetate and fixed to a pyrex slide. The scanning rate of the rotating goniometer was $3^{\circ}/\text{min}$ over a 2Θ range from $5^{\circ} - 140^{\circ}$. Accuracy of all preliminary results was $\pm .002$ Angstroms and determined from measurements on a *Si* standard powder (SRM #640b) obtained from NIST.

Detailed X-ray data collection was carried out at the National Synchrotron Light Source (NSLS) in Brookhaven, N.Y. on the SUNY X3B1 beamline with the assistance of Dr. Peter Stephens, Dr. Sylvina Pagola and Mr. Götz Bendele. Powdered samples were either mounted as flat plates between two pieces of Scotch tape (low temperature studies) or in standard .5mm diameter glass capillaries (room temperature studies). X-rays of 17KeV (.73347 Angstroms), which is just below the *U* L_3 shell edge, were selected by a double *Si*(111) monochromator before diffraction. The absorption length calculated at this energy for *UBe*₁₃ was 78μ . The diffracted X-rays were then sent through a *Ge*(111) analyzer crystal before being detected by a commercial *NaI* scintillation detector. The results were then normalized to the incident beam intensity which was measured as a signal from an ionization chamber between the sample and the monochromator. The extremely narrow Bragg peaks obtained were conducive to analysis via the Rietveld refine-

ment technique of profile matching and refinement [115]. The Rietveld method fits the entire powder pattern to a model rather than extracted Bragg intensities. The standard data analysis software package FullProf was used to obtain the appropriate parameters.

CHAPTER 5

RESULTS

In this chapter we report the results obtained from our characterization of nine *BJLT* single crystals grown and harvested via the *Al* flux technique discussed in section 4.2. We compare these results to polycrystalline and single crystalline UBe_{13} “standards” which display nominal thermal and transport properties. The *BJLT* crystals analyzed originated from two different batches or growth runs. The variables associated with each batch were the rate at which the melt was cooled from $1400^{\circ}C$ to $1000^{\circ}C$ and the concentration (x) of UBe_{13} relative to *Al* in the melt. We list all samples, batch numbers, cooling rates, and UBe_{13} concentrations in table 5.1. They are listed in order of increasing T_c . Our sampling results have shown that approximately 20% of the crystals in a given batch possess the novel features investigated here.

To elucidate the nature of the novel *BJLT* ground state, a series of experiments designed to probe the magnetic, chemical, structural, thermodynamic, and transport properties of the nine anomalous crystals in table 5.1 were performed. In the following sections the results from these experiments are presented. The identification of the crystals used for this study as *BJLT* crystals was confirmed via measurement of the low temperature specific heat. After these measurements were performed, additional structural, chemical, and transport data were gathered. In order to present a clear, continuous picture of this study we begin our analysis with the structural and chemical aspects of the *BJLT* ground state by

Table 5.1: The 9 *BJLT* UBe_{13} single crystals investigated in this study.

<i>BJLT</i> Crystal	Batch #	Cooling Rate ($\frac{^{\circ}C}{hour}$)	$(UBe_{13})_xAl_{1-x}$ (x)
30	2	10	.06
31	2	10	.06
19	7	15	.04
28	2	10	.06
29	2	10	.06
24	7	15	.04
21	7	15	.04
27	2	10	.06
38	2	10	.06

concentrating on *EPMA* and x-ray diffraction results. Then, we present magnetic properties in the context of our results for the magnetic susceptibility. Specific heat and resistivity data follow. Throughout this report we will be comparing the *BJLT* crystal data to those of several UBe_{13} single and polycrystalline standard samples. In table 5.2 we list and describe these standards.

5.1 Electron Probe Microanalysis

In order to investigate the stoichiometry and chemical make-up of the *BJLT* lattice, electron probe microanalysis (*EPMA*) was performed as described in section 4.8. An obvious impurity candidate was *Al*, since all crystals were grown in *Al* flux. The remaining impurities searched for included *Si*, *Fe*, *Ni*, *Ta*, *O*, and *Cu*. These elements represented the impurities with the highest concentrations in the *U* and *Be* starting elements as given by the respective supplier certifications. To avoid possible surface contamination effects due to the insufficient removal of

Table 5.2: The standard samples to which the various *BJLT* crystals were compared in this study.

Sample Description	Crystal Type	Annealing
2A	Single Crystal (SC)	6 months @ 1000°C
13	SC	None
13A	SC	1750 hours @ 1400°C
14	SC	None
7PA	High Purity Polycrystal (PC)	488 hours @ 1200°C
9P	High Purity PC	None
1PA	High Purity PC	1750 hours @ 1400°C

the *Al* flux, all crystals were cleaved and analyzed on an interior surface. A total of 30 random data points were taken for each sample, and the x-ray signal from each point was counted for 100 seconds. In table 5.3 we present the impurity detected down to the .1 atomic percent level of sensitivity available and its concentration for the 9 *BJLT* crystals and 2 standards, polycrystal (PC) 9P and single crystal (SC) 2A. These results indicate 3 important points. First, the only impurity present in the *BJLT* lattice is *Al*. Second, The *Al* is non-uniformly distributed throughout the crystalline lattice. Third, the *Al* resides only on the *Be* site(s). We know this because there is no correlation between the *Al* and *U* concentrations, while the relationship between the *Al* and *Be* concentrations is clear. The larger the *Al* content for a specific point, the smaller the *Be* content, and vice versa. It is also observed that adding *Al* to the *UBe*₁₃ lattice results in a larger lattice parameter (see section 5.2). Since the atomic radius of *Al* (1.43 *Angstroms*) is larger than

Table 5.3: *EPMA* results for the 9 *BJLT* crystals and 2 UBe_{13} standards.

Sample Description	Impurity Detected	$UBe_{13-x}Al_x$ (x)
<i>BJLT</i> 30	<i>Al</i>	.109±.026
<i>BJLT</i> 31	<i>Al</i>	.103±.042
<i>BJLT</i> 19	<i>Al</i>	.122±.040
<i>BJLT</i> 28	<i>Al</i>	.109±.064
<i>BJLT</i> 29	<i>Al</i>	.117±.040
<i>BJLT</i> 24	<i>Al</i>	.120±.043
<i>BJLT</i> 21	<i>Al</i>	.099±.032
<i>BJLT</i> 27	<i>Al</i>	.113±.031
<i>BJLT</i> 38	<i>Al</i>	.108±.031
9P	None	<.001
Standard PC		
2A	None	<.001
Standard SC		

that of *Be* (1.12 *Angstroms*) and less than *U* (1.80 *Angstroms*) the expansion is due to the replacement of *Be* with *Al*. To emphasize the 3 points stated above we give the raw data obtained from a typical *BJLT* crystal (31) in table 5.4. It is clear from the data of table 5.4 that there is no correlation between the *Al* and *U* concentrations, and that the inhomogeneity of the *Al* impurity is statistically significant. To assess the extent of this inhomogeneity, backscattered electron (*BSE*) photographs were taken. We present photos for *BJLT* crystals 19 and 30 (typical of all *BJLT* crystals) as well as standard crystal 2A in figures 5.1-5.3. The dark spots on the *BSE* images originate from an element, or elements, of atomic number lower than that of the surrounding matrix. Due to *EPMA*'s inability to directly detect *Be*, we conclude that the contrast seen in the pictures for samples 19 and 30 is due to the presence of large amounts of non-uniformly distributed *Al*

Table 5.4: Raw *EPMA* data for *BJLT* crystal 31 showing the correlation between the *Al* and *Be* atomic data and the large standard deviation of the *Al* and *Be* concentrations.

Point	<i>U</i> Atomic Percent	<i>Be</i> Atomic Percent	<i>Al</i> Atomic Percent
1	8.04	91.21	.75
2	8.05	91.35	.60
3	8.06	91.05	.89
4	8.09	89.54	2.36
5	8.06	91.41	.53
6	8.07	91.26	.68
7	8.08	91.24	.68
8	8.14	91.04	.82
9	8.03	91.36	.61
10	8.09	90.76	1.15
11	7.98	90.83	1.19
12	7.97	90.42	1.61
13	8.08	90.17	1.74
14	8.05	91.15	.81
15	8.05	91.01	.94
16	8.03	91.12	.85
17	8.09	91.32	.59
18	8.4	87.12	4.48
19	8.1	90.58	1.32
20	8.22	89.63	2.15
21	8.10	91.39	.50
22	8.09	90.22	1.69
23	8.02	91.32	.66
24	8.15	90.16	1.69
25	8.09	90.99	.91
26	8.13	90.88	.99
27	8.13	91.34	.52
28	8.07	90.95	.98
29	8.11	91.31	.59
30	8.05	91.07	.88
Ave	8.09	90.77	1.14
	$\pm .08$	$\pm .86$	$\pm .80$

sitting in a background of uniformly distributed U . To confirm this, the electron beam was concentrated directly onto one of the large dark spots of sample 30 and the x-ray signal counted for 100 seconds. The resulting stoichiometry obtained was $U_{1.019}Be_{12.73}Al_{.251}$. By directing the beam into a clear portion of the atomic matrix and also counting the resulting signal for 100 seconds, a stoichiometry of $U_{1.019}Be_{12.866}Al_{.113}$ was obtained. Further proof for the existence of highly Al rich regions in the $BJLT$ lattice is also shown in figures 5.1-5.3 for samples 19, 30, and 2A. In these photos, known as x-ray maps, only those x-rays characteristic of Al were allowed to diffract and expose the film. The regions sampled in the x-ray map and BSE images are identical. The correlation between the dark regions of the BSE photos and the exposed regions of the Al x-ray map photos is clear. It is important to note that the dimensions of these Al rich islands are on the order of 1μ , which is roughly 2 orders of magnitude greater than the coherence length of UBe_{13} .

The question then arises as to whether Al doped polycrystalline UBe_{13} exhibits this same tendency toward inhomogeneous Al distribution and the formation of highly Al rich islands. We have prepared annealed and unannealed $UBe_{13-x}Al_x$ ($x=.11$ and $.2$), arc-melted portions of $BJLT$ crystals 21 and 24, and annealed a portion of $BJLT$ crystal 30 and subjected them to $EPMA$ analysis. The polycrystalline annealing procedure was an attempt to duplicate the single crystalline growth conditions. A portion of each sample was held at $1400^\circ C$ for 5 hours, and then cooled to $1000^\circ C$ at a rate of $15^\circ C/hour$. We shall refer to this particular annealing protocol as single crystalline growth parameter (SCGP) annealing. Annealing crystal 30 was an attempt to alter the the ground state of a $BJLT$ system

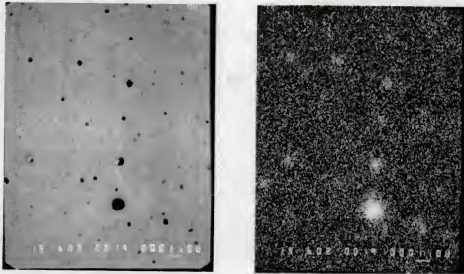


Figure 5.1: *BSE* (left) and x-ray map (right) photos of *BJLT* crystal 19. The dark spots on the *BSE* image are due to a decrease in the yield of back-scattered electrons at the detector compared to the surrounding (lighter shaded) areas. These spots are proven to be *Al* rich via inspection of the x-ray map image taken in the exact same section of the sample. There is a direct correlation between the dark *BSE* regions and the brighter x-ray map , which result from increased scattering of *Al* radiation.

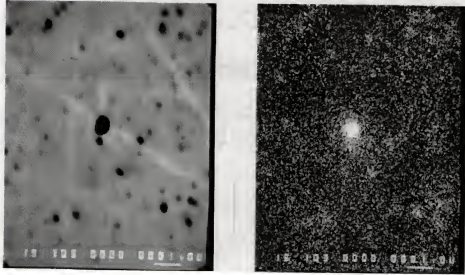


Figure 5.2: *BSE* (left) and x-ray map (right) photos of *BJLT* crystal 30. The dark spots on the *BSE* image are due to a decrease in the yield of back-scattered electrons at the detector compared to the surrounding (lighter shaded) areas. These spots are proven to be *Al* rich via inspection of the x-ray map image taken in the exact same section of the sample. There is a direct correlation between the dark *BSE* regions and the brighter x-ray map , which result from increased scattering of *Al* radiation.



Figure 5.3: *BSE* (left) and x-ray map (right) photos of standard crystal 2A. The pure, *Al*-free nature of this sample is verified by the lack of any dark or bright spots in the *BSE* and x-ray map images.

by affecting changes in atomic position and/or the structure of the unit cell. It was annealed at 1400°C for 504 hours. By melting crystals 21 and 24 we essentially create polycrystalline material and seek to compare the new *Al* distribution with the original distribution. As for the previous samples, 30 random data points, counted for 100 seconds per point, were taken for all samples. The results are presented in table 5.5. From table 5.5 we learn that unannealed *Al* doped polycrystalline UBe_{13} exhibits an inhomogeneous distribution of *Al* on the *Be* lattice sites. We will address the noticeable discrepancy between the experimentally determined *EPMA* *Al* content and the original stoichiometry below. The large standard deviation of the *Al* distribution is in the same proportion to the total (roughly 30%) as it is for the as-grown and melted *BJLT* crystals. This makes a precise determination of the *Al* content difficult. However, the large, abundant *Al* rich regions seen in all *BJLT* crystals are not present in the unannealed *Al* doped samples, as can be seen from the *BSE* images in figure 5.4. After annealing, the *Al* concentration becomes much more homogeneous in these samples, with standard deviations on the order of only 2-3%. Thus, the *Al* distribution in arc-melted $\text{UBe}_{13-x}\text{Al}_x$ appears to be just as inhomogeneous as that in the as-grown *BJLT* crystals. Homogeneity is restored via annealing. At no point do the *Al* doped polycrystals develop the large *Al* rich regions clearly observed in the *BJLT* crystals.

Turning now to melted *BJLT* crystals 21 and 24 (21*M* and 24*M* respectively) we observe that like the unannealed *Al* doped polycrystals and the unmelted crystals 21 and 24, the *Al* inhomogeneity still exists in the *BJLT* crystals after melting. According to the *BSE* and x-ray map images in figures 5.5-5.8, the large *Al* rich

Table 5.5: *EPMA* results for 2 Al doped unannealed and annealed UBe_{13} polycrystals, as-grown and melted *BJLT* crystals 21 and 24, and unannealed and annealed *BJLT* crystal 30.

Sample Description	$UBe_{13-x}Al_x$ (x)	Be content
$UBe_{12.89}Al_{.11}$ Unannealed PC	.053 \pm .018	12.926 \pm .027
$UBe_{12.89}Al_{.11}$ Annealed PC	.035 \pm .001	12.912 \pm .013
$UBe_{12.80}Al_{.20}$ Unannealed PC	.067 \pm .025	12.884 \pm .025
$UBe_{12.80}Al_{.20}$ Annealed PC	.040 \pm .001	12.93 \pm .011
<i>BJLT</i> 21	.099 \pm .032	12.855 \pm .036
<i>BJLT</i> 21 <i>M</i> Melted	.088 \pm .033	12.876 \pm .036
<i>BJLT</i> 24	.120 \pm .043	12.748 \pm .043
<i>BJLT</i> 24 <i>M</i> Melted	.042 \pm .013	12.914 \pm .014
<i>BJLT</i> 30	.109 \pm .026	12.891 \pm .027
<i>BJLT</i> 30 Annealed	****	****

islands have also been substantially dispersed upon melting.¹ We shall see in section 5.4 that the specific heat of the *melted BJLT* crystals is almost identical to that of unannealed $UBe_{12.89}Al_{.11}$.

The effect of long-term high temperature annealing on the *Al* distribution of *BJLT* sample 30 is quite interesting. *EPMA* results give no indication for the presence of *Al* in the annealed lattice of *BJLT* 30. Evidently long-term, high temperature annealing has caused the *Al* to migrate completely out of the UBe_{13} lattice. Although no pockets of pure *Al* were detected in the BSE mode, and the x-ray results of section 5.2 also give no indication for the presence of elemental *Al* in the lattice, we can not rule out the possibility that long-term high temperature annealing caused the *Al* in the lattice of this sample to migrate out of the lattice and become deposited in grain boundaries. As we shall see in section 5.4, the low temperature specific heat of annealed crystal 30 closely resembles that of pure (*Al* free) standard UBe_{13} . The effects of impurities on T_c and ΔC_{T_c} are well documented for this compound and the post annealing microprobe (and specific heat) data presented here strongly suggest that a large proportion of the *Al* has been displaced due to the long-term high temperature annealing. The mass loss upon annealing for this crystal was $\sim .4\%$. A simple calculation shows that *Al* accounts for approximately .6% of the total mass for as-grown crystal 30. The total mass of the sample annealed was only $11.52mg \pm .03mg$, so a mass loss of $\sim .4\%$ is just within our limits of detectability. We also note that the *SCGP* annealing procedure performed on $UBe_{13-x}Al_x$ ($x=.11, .20$) resulted in a dramatic reduction

¹The dark spots visible in figure 5.6 for melted crystal 21 are due to porosity and not to the presence of *Al*. There is no statistically significant correlation between the dark spots in the *BSE* image and their corresponding location in the x-ray map.

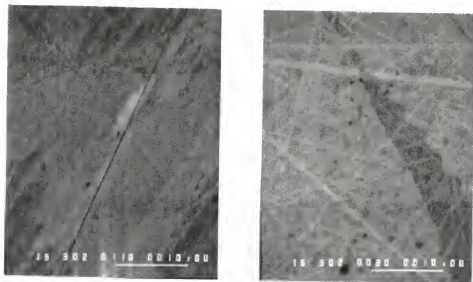


Figure 5.4: *BSE* images of polycrystalline $UB_{e_{12.89}}Al_{11}$ (left) and $UB_{e_{12.80}}Al_{20}$ (right). The lack of any dark regions in these photos is evidence for the absence of the concentrated *Al* islands which form in the *BJLT* single crystals.

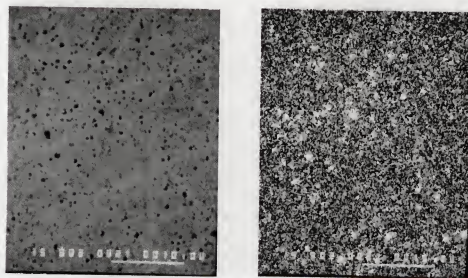


Figure 5.5: *BSE* (left) and x-ray map (right) photos of *BJLT* crystal 21 showing typical *BJLT* *Al* island formation.

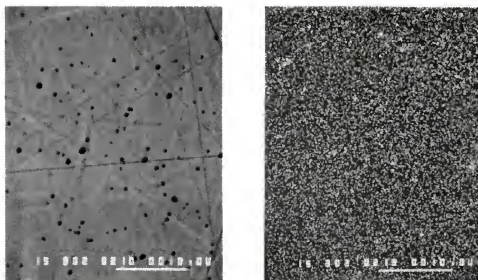


Figure 5.6: *BSE* (left) and x-ray map (right) photos of melted *BJLT* crystal 21 showing a substantial reduction and dispersion of the concentrated *Al* islands compared to figure 5.5. The dark spots in the *BSE* photo are a result of sample porosity. The x-ray map gives no indication for the presence of *Al* at the locations of these *BSE* spots.

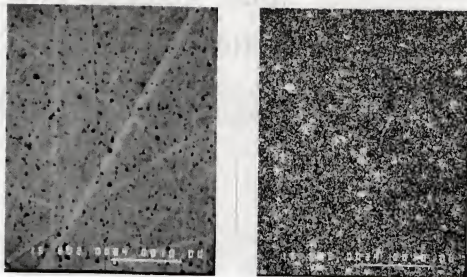


Figure 5.7: *BSE* (left) and *x-ray map* (right) photos of *BJLT* crystal 24 showing typical *BJLT Al* island formation.

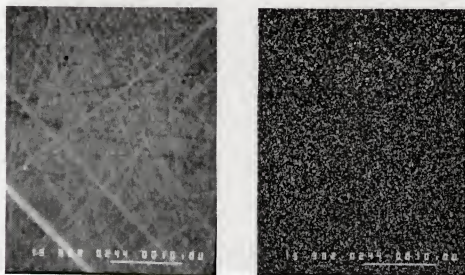


Figure 5.8: *BSE* (left) and *x-ray map* (right) photos of melted *BJLT* crystal 24 showing a substantial reduction and dispersion of the concentrated *Al* islands compared to figure 5.7.

in the *Al* inhomogeneity (indicating substantial atomic redistribution within the lattice), but it was an insufficient amount of time to allow complete migration out of the lattice. We will show in the next section that short-term annealing results in a redistribution of the *Al* impurity among the *Be* lattice sites, and in fact preferential occupation of the larger *BeI* site by the *Al* after annealing. Further proof that *Al* is extremely unstable in the UBe_{13} lattice comes from our long-term high temperature annealing studies on $UBe_{12.92}Al_{.08}$. The unannealed *EPMA* determined *Al* contents of this sample was $Al_{.028}$. After annealing at $1400^{\circ}C$ for 800 hours, the *Al* content of $UBe_{12.92}Al_{.08}$ was reduced to .008.

Finally, it is apparent in the last column of table 5.5 that the *Al* content of all polycrystalline samples, as determined from *EPMA*, is consistently less than what is expected from the original stoichiometry. These polycrystals were fabricated under controlled conditions, and the displacement of such large quantities of *Al* during the arc-melting process is highly unlikely and not consistent with the recorded mass losses. In fact all mass loss during arc-melting may be attributed to *Be*. Because of its large vapor pressure and therefore tendency to evaporate, 6% extra *Be* is added to the starting elements to compensate for any loss incurred during arc-melting. This is a well established fact. The stoichiometry problem observed here is due in large part to the x-ray induced production of x-rays, or fluorescence, of the *Be K*-shell by the *Al K $_{\alpha}$* radiation [116]. The difference in energy between the *Be K* edge and *Al K $_{\alpha}$* radiation is only 1.376 *KeV*. This effect is known to be significant for energy differences of 3 *KeV* or less. To verify this hypothesis we calculated the stoichiometry of 5 *Al* free UBe_{13} single crystals via *EPMA*. The result was an average *Be* concentration of $12.953 \pm .010$, or roughly

5% lower than expected. Thus with no *Al* induced fluorescence the *Be* concentration was too low. Notice from table 5.5 that in all cases the addition of *Al* to the polycrystalline lattice results in *Be* concentrations which are *larger* than expected by 4% and 6% for unannealed $UBe_{12.89}Al_{.11}$ and $UBe_{12.80}Al_{.20}$ respectively. We also note that the sample volume probed by secondary fluorescence can be greater than 1000 times the volume probed by direct electronic excitation.

To summarize, *EPMA* results on as-grown and melted *BJLT* crystals as well as unannealed $UBe_{13-x}Al_x$ ($x=.11, .20$) suggest that *Al* resides strictly on the *Be* lattice sites in these systems and is distributed inhomogeneously throughout the lattice. Annealing appears to homogenize the *Al* content of the polycrystals. The as-grown *BJLT* crystals may be distinguished from the unannealed and annealed *Al* doped polycrystals by the presence of large *Al* rich regions which may contain as much as 2 times the amount of *Al* as that found in the surrounding matrix. Upon melting, the *BJLT* crystals retain their *Al* inhomogeneity, but the large *Al* rich islands are dissipated. The direct observation of the break-up of these regions of higher *Al* content and the reduction in the *Al* content standard deviation are strong indicators for the motion and redistribution of *Al* in the $UBe_{13-x}Al_x$ lattice upon annealing and arc-melting. Thus, as far as the chemical make-up of the underlying lattice is concerned, melted *BJLT* and unannealed *Al* doped polycrystalline UBe_{13} appear quite similar, whereas as-grown *BJLT* crystals appear rather unique. However, it is highly unlikely that the *Al* rich regions in *BJLT* UBe_{13} are the cause of the anomalous T_c and ΔC_{T_c} investigated here. We recall from section 2.2.1 that the mean free path and coherence length for UBe_{13} are on the order of 100 *Angstroms*, while from the scale indicated in the *BSE* and

x-ray map images in this chapter it is clear that the dimensions of the *Al* rich regions are roughly two orders of magnitude larger. It appears from these data that the presence of *Al* in the UBe_{13} lattice is not a sufficient condition for the formation of the *BJLT* ground state. However, using the *Al* impurity (and the *Al* rich islands) as an atomic marker to compare various samples, we have seen through annealing and arc-melting that the *Al* impurity is extremely mobile in the lattice. Arc-melting dissipates the micron sized islands and annealing homogenizes the *Al* content. Thus the conclusion to be drawn from these data is that once *Al* is introduced to the UBe_{13} lattice, the atomic position (and as we shall see in the next section its effect on the size of the underlying lattice) plays a key role in determining the nature of the superconducting ground state.

5.2 X-ray Analysis

The possibility of a structural anomaly or second phase in the *BJLT* crystals was investigated via CuK_{α} ("table top") and synchrotron x-ray diffraction. The synchrotron wavelength chosen was .73347 *Angstroms*. The x-ray determined lattice parameter (a_0) for *BJLT* crystals 19 and 31, 4 *Al* doped polycrystals, and 2 UBe_{13} standards is presented in table 5.6. The parameters for the synchrotron data were obtained via Rietveld refinement fits to the powder diffraction pattern. For these fits, the lattice parameter, over-all isotropic thermal parameter, diffraction line shape parameters and fractional occupancy of the *Al* impurity were varied. The goodness-of-fit is indicated by the value of χ^2 , defined as the square of the ratio of the weighted profile crystallographic *R* factor to the expected crystallographic

R factor. The CuK_{α} data was analyzed with standard techniques, and the lattice parameter determined via an extrapolation of the high angle diffraction data.

We note immediately from these data that the *BJLT* lattice for samples 31 and 19 is expanded by approximately .006 and .004 *Angstroms* respectively over the standard UBe_{13} unit cell of 13A. The similarity between the annealed $UBe_{12.89}Al_{.11}$ lattice parameter and the *BJLT* lattice parameters is also apparent. This is an important result. Annealing 11% and 20% *Al* doped polycrystalline UBe_{13} evidently has a dramatic effect on the size of the unit cell, and for $UBe_{12.89}Al_{.11}$ produces a unit cell with dimensions very similar to that of the *BJLT* lattice. From the previous section (table 5.5) it was observed that annealing had a measurable effect on the *EPMA* determined *Al* homogeneity for this sample. The as-melted sample had an *EPMA* derived *Al* concentration of $Al_{.053} \pm .018$, while the annealed sample yielded a content of $Al_{.035} \pm .001$. This difference, however, is not consistent with the observed decrease in the x-ray determined lattice parameter upon annealing. We shall see that the *EPMA* derived $\sim 30\%$ reduction in the *Al* content of this sample after annealing should result in a lattice parameter of 10.265 *Angstroms* as opposed to the 10.262 *Angstroms* measured here. A similar argument for the 20% *Al* doped sample shows that the annealed sample lattice parameter should be 10.269 *Angstroms* as opposed to the observed value of 10.265. We may explain this by first noting that the large standard deviation of the *Al* content of all unannealed samples makes the average *Al* values (and thus the reduction after annealing) rather imprecise. We have also seen how the effects secondary x-ray fluorescence cause the absolute values of the *Al* and *Be* concentrations to be uncertain as well. The redistribution of the *Al* among

Table 5.6: X-ray diffraction results for *BJLT* crystals 19 and 31, 4 *Al* doped polycrystals and 2 *UBe*₁₃ standards.

Sample Description	CuK_{α} a_0 (<i>Angstroms</i>)	Synchrotron a_0 (<i>Angstroms</i>)	Goodness-of-fit χ^2
<i>BJLT</i> 31	10.264 \pm .002	10.2634 \pm .0002	2.06
<i>BJLT</i> 19	10.262	****	****
<i>UBe</i> _{12.89} <i>Al</i> ₁₁ Unannealed PC	****	10.2689	1.76
<i>UBe</i> _{12.89} <i>Al</i> ₁₁ Annealed PC	10.262	****	****
<i>UBe</i> _{12.97} <i>Al</i> ₀₃ Unannealed PC	10.262	****	****
<i>UBe</i> _{12.94} <i>Al</i> ₀₆ Unannealed PC	10.265	****	****
<i>UBe</i> _{12.80} <i>Al</i> ₂₀ Unannealed PC	10.279	****	****
<i>UBe</i> _{12.80} <i>Al</i> ₂₀ Annealed PC	10.265		
<i>UBe</i> _{12.75} <i>Al</i> ₂₅ Unannealed PC	10.284	****	****
13A Standard SC	****	10.2570	2.03
1PA Standard PC	10.258	****	****

the *Be* lattice sites is, however, very clear. We have calculated the atomic site volumes of the *BeI* and *BeII* lattice sites² for the UBe_{13} unit cell, and discovered that the *BeI* site volume (25.277 *Angstroms*³) is 35% larger than the *BeII* site volume (18.736 *Angstroms*³). The drastic reduction in the lattice parameter seen here after annealing may then be explained by requiring preferential *BeI* site occupation of the *Al*. It has already been determined via *NMR* analysis that *B* resides exclusively on the *BeI* site in polycrystalline $UBe_{13-x}B_x$. In section 5.4 we show that annealing also has a pronounced effect on the specific heat of $UBe_{12.89}Al_{.11}$.

Besides preferential *BeI* site occupation, the reduction in the lattice parameter of annealed $UBe_{12.89}Al_{.11}$ may be due to the *Al* migrating completely out of the UBe_{13} lattice and forming interstitial pockets of pure *Al*. Annealing may also reduce the effects of any non-uniform lattice strain present. Before addressing these points it is important to note that our attempts to obtain more accurate fits to the x-ray data of $UBe_{12.89}Al_{.11}$ and *BJLT* 31 by requiring preferred occupation of either *Be* lattice site by the *Al* impurity were unsuccessful due to the low concentration of *Al* present and the very weak (only 2-3 times that of *Be*) atomic scattering factor at such a short x-ray wavelength. In fact, even for the sample with the largest *Al* concentration ($UBe_{12.89}Al_{.11}$) the goodness-of-fit parameter χ^2 remained unchanged ($\chi^2=1.76$) in going from placing no *Al* in the lattice to placing stoichiometric amounts of *Al* either randomly distributed among the *Be* sites or on only 1 *Be* site. So for the samples investigated here, we are unable to directly observe the possible redistribution of *Al* between the *Be* atom sites in going from an unannealed to annealed *Al* doped UBe_{13} unit cell via x-ray diffraction.

²We are indebted to Dr. Mike Jones for his assistance in these calculations.

We may search for the presence of strain and secondary phases by analyzing the x-ray spectrum of *BJLT* sample 31, shown in figures 5.9 and 5.10. All peaks in this spectrum, as well as the unannealed and annealed $UBe_{13-x}Al_x$ ($x = .11, .20$) polycrystalline spectra, may be indexed to the cubic $cF112$ ($Fm3c$) structure. The sensitivity of synchrotron radiation to impurity phases is $\sim 1\%$ by weight. Although there is a direct correlation between the *Al* and *Be* concentrations for all *EPMA* data points taken for this sample, the lack of any anomalous, secondary peaks in the x-ray spectrum for sample 31, as well as the adherence to Vegard's for *Al* doped polycrystalline material (see below), is further proof that the *Al* impurity resides in the UBe_{13} lattice and is not interstitial or a component of a secondary phase. For a typical powder specimen of 15mg, a calculation based on the stoichiometry $UBe_{12.95}Al_{.05}$ shows that the *Al* mass is .4% of the starting weight, and therefore should produce observable elemental impurity x-ray peaks if separate from the majority phase. The extremely sharp, narrow diffraction peaks of sample 31 also show no sign of asymmetry or broadening due to lattice strain. In fact for 5 randomly chosen peaks ((0,2,10), (8,4,4), (8,2,0), (8,4,2), and (4,2,2)) the full width at half maximum (FWHM) for *BJLT* 31 was consistently 25% less than that of annealed, *Al*-free standard 13A. We note that a similar analysis for unannealed $UBe_{12.89}Al_{.11}$ indicated that the FWHM for the same peaks listed above was consistently 1.5 to 2 times greater than *Al*-free standard 13A. Another method often used to search for lattice strain is to obtain the slope from a plot of the FWHM vs. 2θ for several families of lattice planes and to look for deviations among the families. This was done for *BJLT* 31 for the (x,0,0), (x,x,0), and (x,x,x) lattice planes from $8 \leq 2\theta \leq 43$. The result of this calculation was that all

slopes were identical to within 8% for *BJLT* 31 and 13A, and .7% for unannealed $UBe_{12.89}Al_{.11}$. Thus we see that the presence of *Al* in the UBe_{13} lattice has a measurable effect on the size of the lattice, and also possibly on the shape of the unit cell. The *Al* rich single crystal 31 appears to have incorporated *Al* into the lattice in such a way as to minimize any residual stress and strain experienced by the unit cell, whereas the arc-melted sample $UBe_{12.89}Al_{.11}$ shows possible evidence for stress related line broadening.

By plotting the unannealed *Al* doped lattice parameters of table 5.6 versus the *Al* concentrations (see figure 5.11), Vegard's linear relationship is verified for this doped system. The fact that this relationship is satisfied over a large range of impurity concentrations is evidence that the *Al* does indeed enter the UBe_{13} lattice during arc-melting and does not form a second phase or interstitial pockets. Clearly our previous results for the lattice parameters of *annealed* $UBe_{12.89}Al_{.11}$ (10.262 *Angstroms*) and *annealed* $UBe_{12.80}Al_{.20}$ (10.265 *Angstroms*) would fall well below the linear relationship displayed by the *unannealed* samples in this plot even if we incorporate the slight reduction in the *Al* content seen in the *EPMA* data. Since there is no evidence for second phases or interstitial pockets, we may conclude from this that the substantially reduced lattice parameter is a result of the redistribution of a portion of the *Al* impurity to the larger *BeI* lattice site. In fact by plotting the annealed lattice parameters of $UBe_{13-x}Al_x$ ($x = .11, .20$) in figure 5.12, along with the *Al*-free annealed single crystal 13A data, we see that the linear relationship between lattice parameter and *Al* concentration is obeyed even in the annealed state. This argues against the random loss of *Al* during annealing and also against the accumulation of *Al* in grain boundaries, and suggests that *Al*

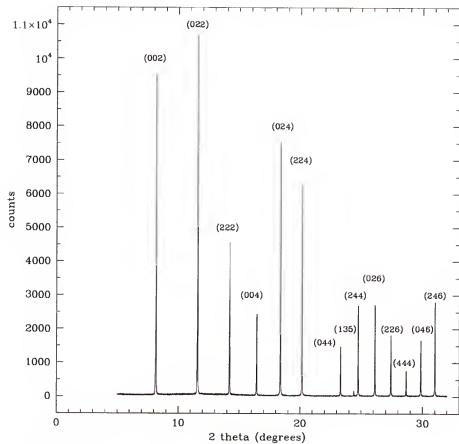


Figure 5.9: The synchrotron x-ray spectrum of *BJLT* crystal 31. This data was taken at a wavelength of .73347 *Angstroms*. All peaks are indexed to the cubic *cF112* (*Fm3c*) structure.

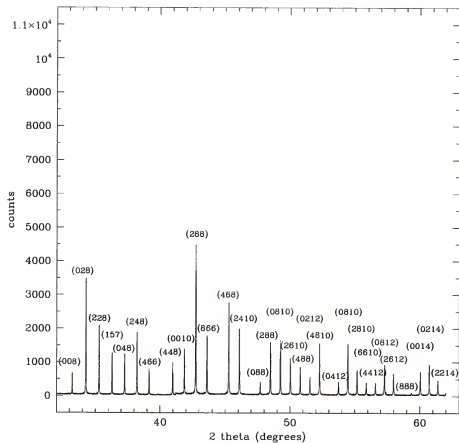


Figure 5.10: The synchrotron x-ray spectrum of *BJLT* crystal 31. This data was taken at a wavelength of .73347 *Angstroms*. All peaks are indexed to the cubic *cF112* (*Fm3c*) structure.

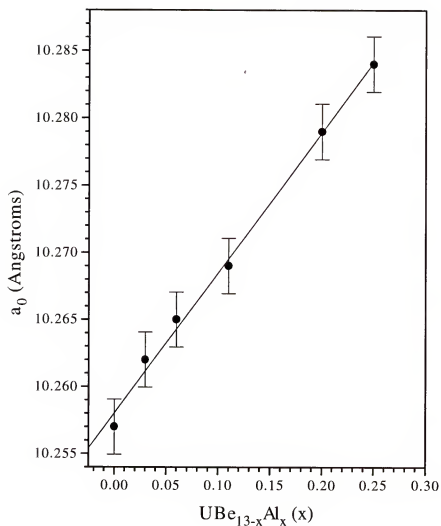


Figure 5.11: The lattice constant (a_0) vs. Al concentration (x) for $UBe_{13-x}Al_x$. The linear relationship is known as Vegard's law, and allows for interpolation of Al content based on lattice size. It also indicates that Al is very soluble in this lattice and enters the lattice in a very systematic way. The error bars are based on our CuK_α x-ray data. Note that the lattice parameter for annealed $UBe_{12.89}Al_{1.11}$ (10.262 Angstroms) falls well below the linear relationship established by the unannealed samples measured here.

enters the lattice and is redistributed inside the lattice in a very systematic manner. We may assume that the *Al* in the unannealed arc-melted samples is uniformly distributed among the *BeI* and *BeII* sites. Since there is 1 *BeI* site to every 12 *BeII* sites, a simple calculation gives unannealed stoichiometries of approximately $UBe_{11.90}^{II}Al_{.10}Be_{.99}^IAl_{.01}$ and $UBe_{11.82}^{II}Al_{.18}Be_{.98}^IAl_{.02}$. After annealing, if we assume that all of the *Al* in the 11% doped sample migrates to the *BeI* site, and an equal percentage of the *Al* in the 20% doped sample also migrates to this site. The final stoichiometries achieved are then $UBe_{12.00}^{II}Be_{.89}^IAl_{.11}$ and $UBe_{11.98}^{II}Al_{.02}Be_{.82}^IAl_{.18}$.

In summary, CuK_{α} and synchrotron x-ray diffraction results for the *BJLT* single crystals indicate that, when compared to standard UBe_{13} , the *BJLT* lattice is expanded due to the presence of *Al*. However, compared to polycrystals with similar *Al* contents the *BJLT* lattice appears substantially contracted. There is no evidence for secondary phases, interstitial pockets, or lattice strain in the *BJLT* lattice. Upon annealing, the lattice parameter of $UBe_{12.89}Al_{.11}$ is reduced by $\sim .007$ Angstroms and approaches that of the single crystalline *BJLT* unit cell. No second phases or interstitial pockets of *Al* were detected in the unannealed or annealed $UBe_{12.89}Al_{.11}$ lattice, although there is evidence for the possibility of stress related line broadening. A redistribution of a majority of the *Al* impurity after annealing to the larger *BeI* lattice site would explain the significant contraction of the lattice observed in $UBe_{13-x}Al_x$ ($x=.11, .20$) after annealing. This preferential site occupation and lattice contraction (and the resulting enhanced specific heat, as we shall see) give annealed $UBe_{12.89}Al_{.11}$ a very *BJLT*-like structure and ground state.

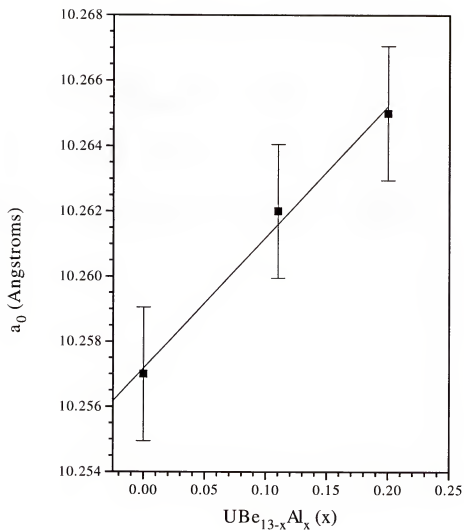


Figure 5.12: The lattice constant (a_0) vs. Al concentration (x) for annealed $UBe_{13-x}Al_x$ ($x=0, .11, .20$). The linear relationship which exists in the annealed state suggests that the reduction in the lattice parameter in these samples after annealing is due to a systematic redistribution of the Al impurity and preferential BeI site occupation, and not random Al losses.

5.3 Magnetic Susceptibility

The d.c. magnetic susceptibility of all *BJLT* crystals was measured in the low field regime of 100G from 1.8K to 300K. We define the susceptibility (χ) as the ratio of the magnetization (M) to the applied field (H). The susceptibility, effective moment, and Curie temperature for all as-grown, melted, and annealed *BJLT* crystals 4 standard samples, as well as annealed and unannealed $UBe_{13-x}Al_x$ ($x=.11, .20$) are given in table 5.7. Representative as-grown *BJLT* and standard data (for samples 19, 31, and 9P) are shown in figures 5.13-5.15. The data listed in table 5.7 are somewhat sample dependent with no observable distinction between either single and polycrystalline UBe_{13} or between the *Al* doped and pure material. Annealing appears not to affect the state of the *Al* doped samples. The average values of $\chi(1.8K)$ and μ_{eff} for the 9 as-grown *BJLT* crystals are 14.72 *memu/mole* and $3.6\mu_B$ respectively, and are comparable to the values obtained for all standard and *Al* doped samples listed. We concentrate now on the susceptibility data for the melted and annealed *BJLT* crystals. As we shall see in section 5.4, the melting and annealing of *BJLT* crystals has a profound effect on their thermal properties, most notably T_c and ΔC_{T_c} . The question arises as to whether the changes in these thermal parameters are linked to any observable change in the magnetic parameters discussed here. According to the data in table 5.7 concerning crystals 21 and 24, melting does not have any consistent effect on $\chi(1.8K)$, μ_{eff} , or θ_{CW} . The effective moment and strength of the antiferromagnetic correlations are seen to decrease for sample 21 and increase for sample 24 after melting. All values, before and after melting, are nominal. Melting the *BJLT* crystals essentially creates *Al* doped polycrystalline material (this will become more clear when we present the

specific heat results in section 5.4) and has no effect on the magnetic aspects of the ground state. The susceptibility data for the as-grown and melted samples 21 and 24 are shown in figures 5.16-5.17.

We turn now to the data for unannealed and annealed *BJLT* crystal 30. It is clear that annealing results in a marked increase in the values of μ_{eff} and $|\theta_{CW}|$ for sample 30, while the value of $\chi(1.8K)$ is enhanced only marginally and is within the scatter limits for UBe_{13} . The data are presented in figure 5.18. In section 5.4, via specific heat measurements, we show that annealing *BJLT* crystal 30 essentially destroys the *BJLT* ground state and restores the standard UBe_{13} ground state. This fact makes the data presented in figure 5.18 even more intriguing. What is the cause of this anomaly with an onset temperature of $\sim 160K$ in annealed *BJLT* UBe_{13} ? Whatever the nature of this anomaly, the data make it clear that it is not a necessary condition for the formation of either the standard or *BJLT* UBe_{13} ground states. Therefore we will leave a detailed analysis of this feature for appendices A and B, and concentrate our efforts in this chapter on understanding the *BJLT* ground state.

To summarize, the magnetic susceptibility results for the *BJLT* crystals presented here suggest that the magnetic correlations which may exist in pure UBe_{13} are neither enhanced nor suppressed (down to 1.8K) in these novel crystals. The results for as-grown and melted *BJLT* samples are comparable to and within the scatter limits for pure UBe_{13} and *Al* doped polycrystalline UBe_{13} . However, annealing has quite an unexpected effect on the UBe_{13} ground state, and produces an anomaly in χ with an onset temperature of 160K. This anomaly is not a necessary

Table 5.7: The magnetic susceptibility, effective moment, and Curie-Weiss temperature for all *BJLT* crystals, melted crystals 21*M* and 24*M*, and 3 high purity polycrystalline and 1 single crystalline standard.

Sample Description	$\chi(1.8K)$ ($\frac{\text{emu}}{\text{mole}}$)	μ_{eff} (μ_B)	Θ_{CW} (K)
<i>BJLT</i> 30	$14.5 \pm .3$	3.55	-105
<i>BJLT</i> 30 Annealed	16.8	4.17	-145
<i>BJLT</i> 31	14.5	3.62	-119
<i>BJLT</i> 19	15.3	3.51	-98
<i>BJLT</i> 28	15.2	3.82	-131
<i>BJLT</i> 29	13.8	3.41	-103
<i>BJLT</i> 24	14.7	3.52	-104
<i>BJLT</i> 24 <i>M</i> Melted	14.6	3.8	-134
<i>BJLT</i> 21	14.9	3.91	-144
<i>BJLT</i> 21 <i>M</i> Melted	14.1	3.57	-118
<i>BJLT</i> 27	14.8	3.52	-105
<i>BJLT</i> 38	14.8	3.55	-103
9 <i>P</i>	14.6	3.55	-110
Standard PC			
7 <i>P</i>	15.3	3.96	-147
Standard PC			
11 <i>P</i>	13.8	3.6	-130
Standard PC			
$UBe_{12.89}Al_{11}$	14.56	3.538	-111
Unannealed PC			
$UBe_{12.89}Al_{11}$	14.91	3.665	-117
Annealed PC			
$UBe_{12.80}Al_{20}$	14.43	3.334	-87
Unannealed PC			
$UBe_{12.80}Al_{20}$	14.60	3.826	-132
Annealed PC			
2 <i>A</i>	15.4	3.61	-114
Standard SC			

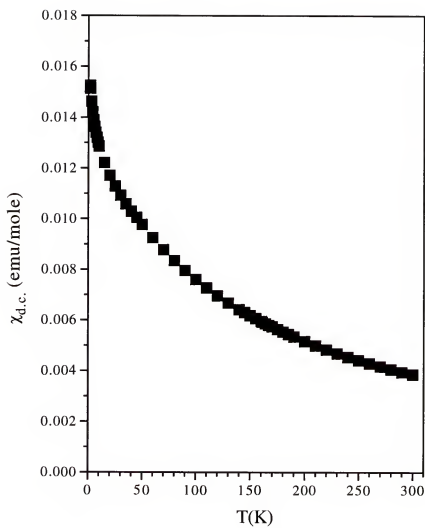


Figure 5.13: The magnetic susceptibility vs. temperature for *BJLT* crystal 19.

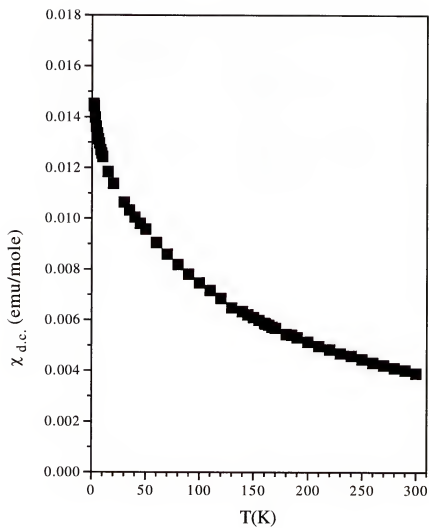


Figure 5.14: The magnetic susceptibility vs. temperature for *BJLT* crystal 31.

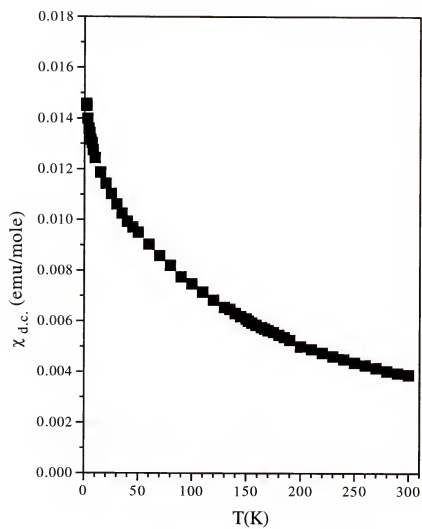


Figure 5.15: The magnetic susceptibility vs. temperature for standard polycrystal 9P.

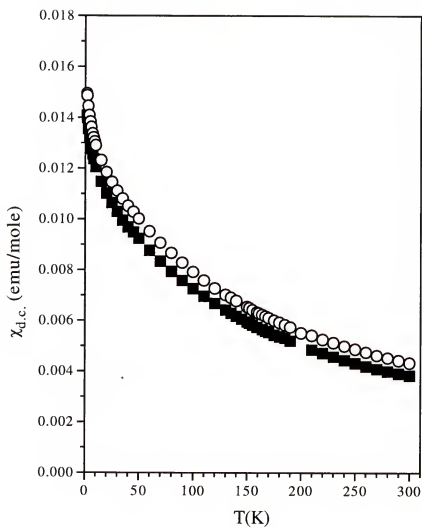


Figure 5.16: The magnetic susceptibility vs. temperature for as-grown (solid squares) and melted (open circles) *BJLT* crystal 21.

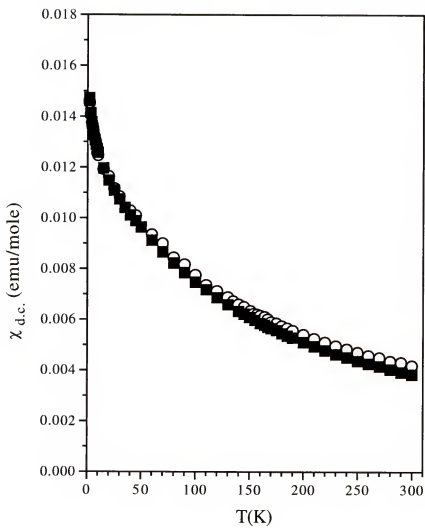


Figure 5.17: The magnetic susceptibility vs. temperature for as-grown (solid squares) and melted (open circles) *BJLT* crystal 24.

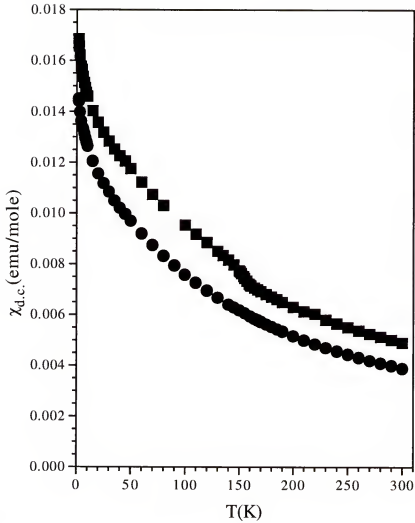


Figure 5.18: The magnetic susceptibility vs. temperature for as-grown (circles) and annealed (squares) *BJLT* crystal 30. This crystal was annealed for 504 hours at 1400°C . The anomalous behavior seen at 160K has been observed in other UBe_{13} samples, both pure and doped, and is not a necessary condition for the formation of either the standard or *BJLT* UBe_{13} ground states. Note also that annealed sample was measured in an applied field of $H=1000\text{G}$ to increase the signal and reduce the effects of scatter.

condition for the formation of the *BJLT* or standard UBe_{13} ground states and will be investigated in appendices A and B.

5.4 Specific Heat

Low temperature specific heat results for the 9 as-grown *BJLT* crystals and UBe_{13} standards 2A and 9P are presented in table 5.8, where all parameters have been defined previously in section 2.2.3. The last 2 columns give the ratio of the *BJLT* crystal T_c to T_c of standard 2A (T_c/T_{c0}) and the ratio of the respective specific heat discontinuities at T_c ($\Delta C_{T_c}/\Delta C_{T_{c0}}$). In figures 5.20-5.28 we plot

Table 5.8: Low temperature specific heat parameters for the *BJLT* crystals and 2 UBe_{13} standards.

Sample Description	T_c (K)	ΔC_{T_c} ($\frac{mJ}{mole-K^2}$)	T_c/T_{c0}	$\Delta C_{T_c}/\Delta C_{T_{c0}}$
<i>BJLT</i> 30	.72±.03	2429±121	.79	1.42
<i>BJLT</i> 31	.73	2283	.80	1.34
<i>BJLT</i> 19	.73	2196	.80	1.28
<i>BJLT</i> 28	.74	2299	.81	1.35
<i>BJLT</i> 29	.74	2168	.81	1.27
<i>BJLT</i> 24	.74	2100	.81	1.23
<i>BJLT</i> 21	.74	2638	.81	1.55
<i>BJLT</i> 27	.74	2100	.81	1.23
<i>BJLT</i> 38	.75	2566	.82	1.50
9P	.90	1697	.99	.99
Standard PC				
2A	.91	1705	1	1
Standard SC				

the data for each crystal along with the data of standard crystal 2A for comparison purposes. All *BJLT* crystals display the characteristic depressed T_c and

enhanced ΔC_{T_c} . We have seen in section 2.2.3 that doping UBe_{13} with magnetic and non-magnetic impurities results in a rapid suppression of ΔC_{T_c} and a reduced T_c compared to the nominally pure starting material. The extremely interesting nature of the data in table 5.8 is made more clear if we plot the last 2 columns as $\Delta C_{T_c}/\Delta C_{T_{c0}}$ versus T_c/T_{c0} . This is shown in figure 5.19. What it means for a superconductor which clearly contains a measurable quantity of a known impurity (*Al*) to lie *above* the *BCS* law of corresponding states in such a plot is unclear and leads to several questions. First, is the enhanced ΔC_{T_c} in these crystals a result of increased strong coupling effects? Second, is the observed *BJLT* transition really the admixture of 2 separate transitions which occur at nearly the same temperature? And finally, might the difference between the standard and *BJLT* superconducting transitions be an indication of a change in the symmetry of the UBe_{13} ground state? We would also like to know if the interesting single crystalline results presented here are purely the result of *Al* impurity effects incurred during the single crystalline growth process or whether they may be reproduced in polycrystalline material.

We begin our analysis by displaying a typical *BJLT* equal entropy construction (as discussed in section 2.2.3) for *BJLT* crystal 19 in figure 5.29 and comparing it to a similar construct for standard 2A (figure 2.8). As we have seen in section 2.2.3, standard UBe_{13} possesses a positive entropy mismatch at T_c . In order to ensure that the normal and superconducting entropies at T_c (S_n and S_{sc}) are equal in standard UBe_{13} , the normal state data below T_c must be extrapolated to $T=0$ in such a way as to *increase* the normal state entropy, thereby arriving at the correct value of C/T at $T=0$, defined as $\gamma(0)$. What is immediately apparent

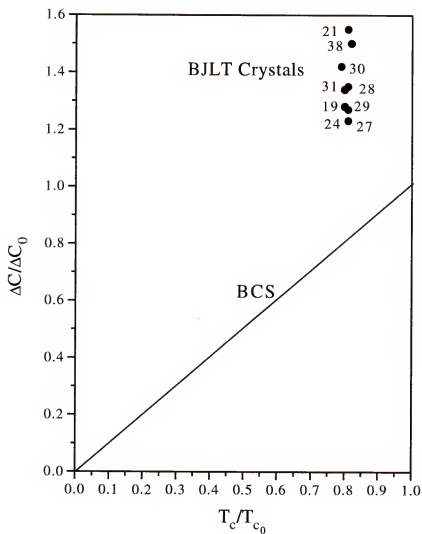


Figure 5.19: $\Delta C_{T_c}/\Delta C_{T_{c0}}$ versus T_c/T_{c0} for all 9 *BJLT* crystals investigated in this study. The straight line represents the behavior one would expect due to the so-called BCS law of corresponding states.

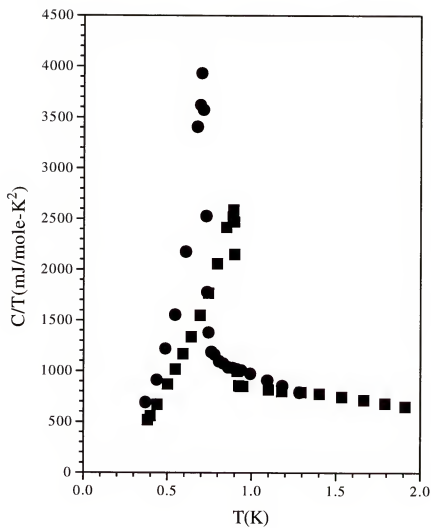


Figure 5.20: The specific heat divided by temperature vs. temperature for *BJLT* crystal 30 (circles) and standard UBe_{13} crystal 2A (squares).

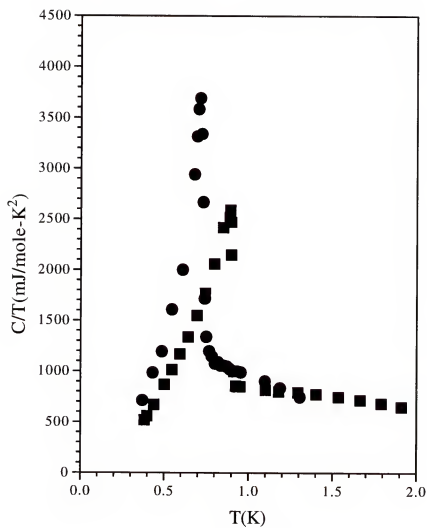


Figure 5.21: The specific heat divided by temperature vs. temperature for *BJLT* crystal 31 (circles) and standard UBe_{13} crystal 2A (squares).

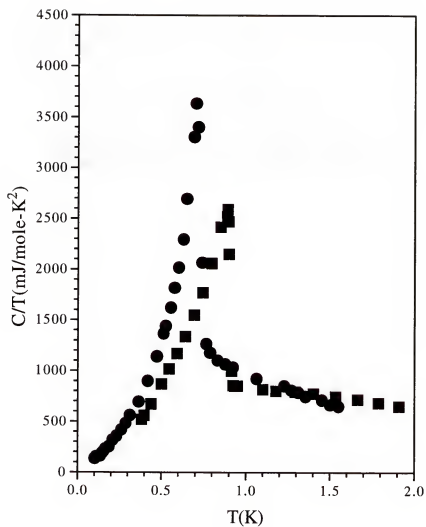


Figure 5.22: The specific heat divided by temperature vs. temperature for *BJLT* crystal 19 (circles) and standard UBe_{13} crystal 2A (squares).

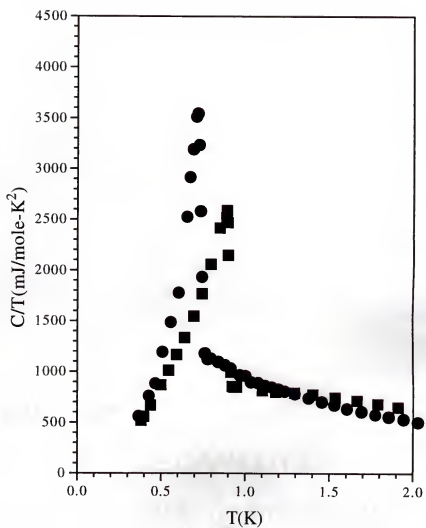


Figure 5.23: The specific heat divided by temperature vs. temperature for *BJLT* crystal 28 (circles) and standard UBe_{13} crystal 2A (squares).

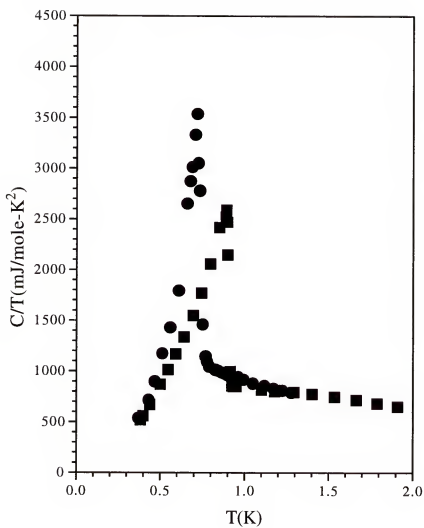


Figure 5.24: The specific heat divided by temperature vs. temperature for *BJLT* crystal 29 (circles) and standard UBe_{13} crystal 2A (squares).

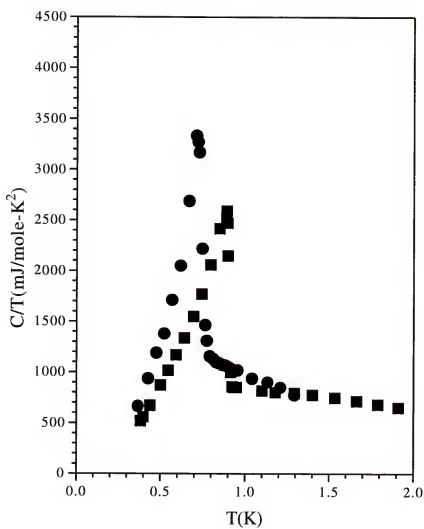


Figure 5.25: The specific heat divided by temperature vs. temperature for *BJLT* crystal 24 (circles) and standard UBe_{13} crystal 2A (squares).

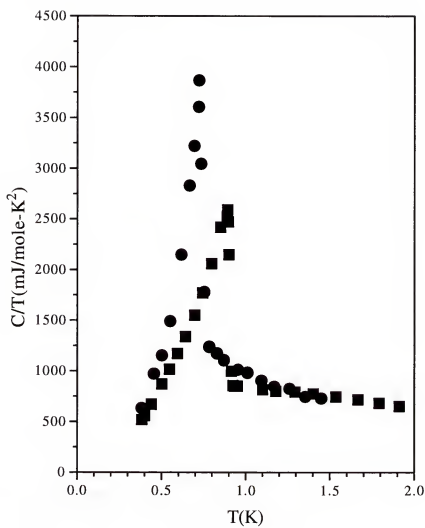


Figure 5.26: The specific heat divided by temperature vs. temperature for *BJLT* crystal 21 (circles) and standard UBe_{13} crystal 2A (squares).

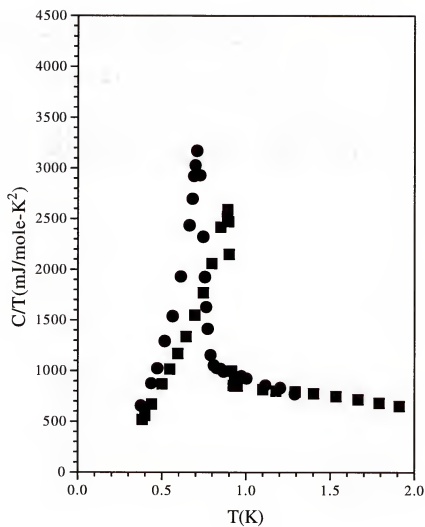


Figure 5.27: The specific heat divided by temperature vs. temperature for *BJLT* crystal 27 (circles) and standard UBe_{13} crystal 2A (squares).

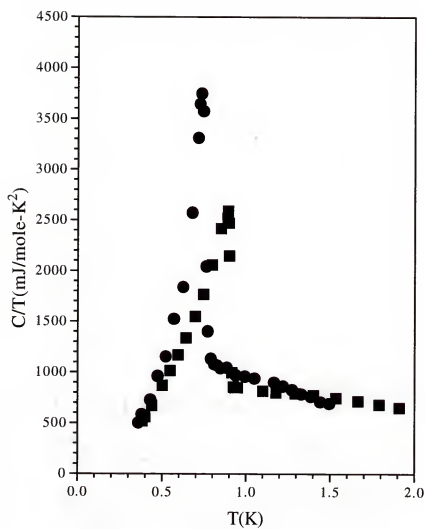


Figure 5.28: The specific heat divided by temperature vs. temperature for *BJLT* crystal 38 (circles) and standard UBe_{13} crystal 2A (squares).

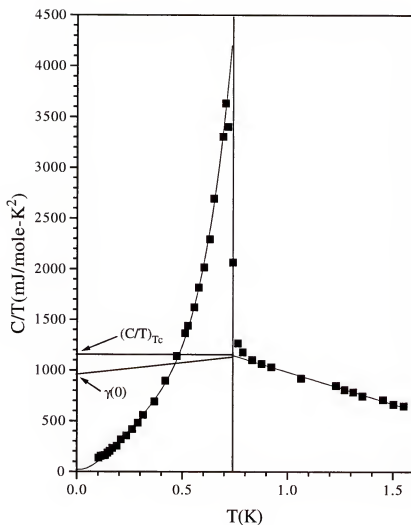


Figure 5.29: The specific heat divided by temperature vs. temperature for *BJJLT* crystal 19 used to construct an equal entropy plot. A constant C/T below T_c results in the normal state entropy being 8% larger than the superconducting entropy at T_c . To remedy this, a simple, linear fit from T_c to $T=0$ is postulated to decrease the normal state entropy by the required amount and ensure equal entropy at T_c .

from figure 5.29 is that the *BJLT* crystal shown (19), which is typical of all *BJLT* crystals analyzed, possesses a *negative* entropy balance at T_c . Thus, unlike standard UBe_{13} , *BJLT* UBe_{13} requires us to *decrease* the normal state entropy when arriving at $\gamma(0)$. It is this value of $\gamma(0)$, required to conserve entropy at T_c , which we shall use in subsequent calculations. The parameters obtained from equal entropy constructions for all *BJLT* crystals are given in table 5.9.

Table 5.9: Low temperature specific heat parameters obtained from equal entropy constructions for the *BJLT* crystals and 2 UBe_{13} standards.

Sample Description	$C/T(1K)$ $(\frac{mJ}{mole-K^2})$	$C/T(T_c)$ $(\frac{mJ}{mole-K^2})$	$\gamma(0)$ $(\frac{mJ}{mole-K^2})$	$\% \Delta S$ $(\frac{S_{sc}-S_n}{S_{sc}})$	β $(\frac{mJ}{mole-K^2})$
<i>BJLT</i> 30	966 \pm 50	1136 \pm 57	1085 \pm 55	-3	3.11
<i>BJLT</i> 31	955	1127	1058	-3	2.96
<i>BJLT</i> 19	984	1157	985	-8	3.05
<i>BJLT</i> 28	933	1072	920	-8	3.38
<i>BJLT</i> 29	917	1048	901	-8	3.25
<i>BJLT</i> 24	984	1162	1016	-5	2.79
<i>BJLT</i> 21	980	1145	947	-7	3.55
<i>BJLT</i> 27	925	1061	1005	-3	2.82
<i>BJLT</i> 38	976	1132	920	-10	3.72
9P	778	784	895	+7	2.13
Standard PC					
2A	837	852	1031	+9	1.83
Standard SC					

It is clear that all *BJLT* crystals possess a negative entropy mismatch at T_c which requires that the value of $\langle C/T \rangle_{T_c}$ be substantially reduced to ensure entropy balance. As a result of this necessary procedure, the resulting value of $\gamma(0)$ for the *BJLT* crystals is not enhanced over that of standard UBe_{13} . By dividing the large discontinuity in C at T_c by $\gamma(0) \cdot T_c$ we are able to calculate the *BCS*

coupling strength parameter β , given in the last column of table 5.9. The extremely large values of β may be an indication of increased strong coupling effects in *BJLT* UBe_{13} since the *BCS* isotropic *s*-wave value of β is 1.43, while a possible anisotropic *d*-wave value is .67. Since most of the evidence to date suggests that UBe_{13} is an anisotropic *d*-wave superconductor, a change in the symmetry of the superconducting ground state from *d*-wave to *s*-wave in the *BJLT* crystals would result in a factor of 2 increase in the coupling parameter β . As we see in table 5.9, the *BJLT* coupling parameter is enhanced over the standard UBe_{13} value by factors of 1.2-2. Using *BJLT* crystal 27 and standard 2A for comparison purposes, we note that if both ground states were of *d*-wave symmetry, then the coupling of crystal 27 is enhanced over that of the standard by a factor of 1.5. If, however, the symmetry of crystal 27 is *s*-wave in character, then compared to the *d*-wave standard the coupling of crystal 27 is actually reduced by $\sim 28\%$.

In figure 5.30 we plot the low temperature specific heat for *BJLT* 19 below .37K. Attempts to fit these data via a power-law relationship result in a temperature dependence ($C \propto T^\alpha$) of $\alpha = 2.4$. This may be compared to the values $\alpha = 2.8 - 3.0$ obtained previously on standard single and polycrystalline UBe_{13} [93, 14, 117, 92]. Although the data presented here fall into a rather limited temperature range, this change in the temperature dependence in C from standard to *BJLT* UBe_{13} may be an indication of a difference in the nodal structure between the two superconducting ground states. We shall see later in this section that while ΔC_{T_c} for polycrystalline $UBe_{12.89}Al_{.11}$ is markedly suppressed compared to that of *BJLT* or standard UBe_{13} , T_c for this sample is only .02K higher than T_c for *BJLT* crystal 30. This small difference is well within our error bars for T_c .

Moreover, once $UBe_{12.89}Al_{.11}$ is annealed ΔC_{T_c} is enhanced to a standard-like value while T_c is again unchanged. Also, arc-melting *BJLT* crystals 21 and 24 (figures 5.35 and 5.36) results in a substantially reduced ΔC_{T_c} and unchanged T_c for these crystals. So it appears that the depressed T_c observed in all doped polycrystalline and impure *BJLT* crystals (as-grown or melted) is due to the well known effects of the *Al* impurity on the anisotropic (possibly *d*-wave) order parameter. Since we see no change in T_c among all of these samples, whether suppressed polycrystalline or enhanced *BJLT*, we conclude that *Al* behaves similarly in all samples and that all ground states are of the same (anisotropic) symmetry.

In order to investigate the possibility of 2 separate transitions occurring at nearly the same temperature we turn to table 5.10. Here, we list the transition widths (defined as the difference between the temperature of the experimental peak and T_c), values of $\gamma(0)$, and superconducting entropy for the *BJLT* crystals and 2 standards. Were the large *BJLT* peaks the result of 2 transitions we would expect that the transition widths would increase beyond those of standards 2A and 9P. This is clearly not the case. All *BJLT* crystals display sharp peaks with nearly vertical transitions. We also note from table 5.10 that the entropy under the *BJLT* transition, when compared to standards 2A and 9P, is not enhanced considering the range of the values given and our 3% error bars. And finally, the value of $\gamma(0)$ for all crystals listed (standard and *BJLT*) is, within our error bars of $\pm 5\%$, unchanged. Thus the low temperature specific heat data presented here suggests that the *BJLT* peak is due to a single superconducting phase transition. We turn now to the specific heat above 2K.

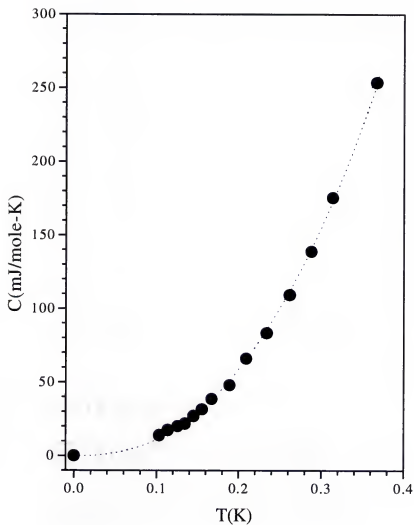


Figure 5.30: The low temperature specific heat vs. temperature for *BJLT* crystal 19. The dashed line is a best fit to the data, and indicates a temperature dependence of $T^{2.4}$ over this limited range. This is to be compared to the standard UBe_{13} temperature dependence of T^3 .

Table 5.10: Low temperature specific heat parameters for the *BJLT* crystals and 2 UBe_{13} standards.

Sample Description	Transition Width (K)	$\gamma(0)$ ($\frac{mJ}{mole-K^2}$)	S_{sc} ($\frac{mJ}{mole-K}$)
<i>BJLT</i> 30	.02	1085 ± 55	805 ± 24
<i>BJLT</i> 31	.01	1058	800
<i>BJLT</i> 19	.02	985	785
<i>BJLT</i> 28	.02	920	734
<i>BJLT</i> 29	.02	901	720
<i>BJLT</i> 24	.02	1016	809
<i>BJLT</i> 21	.02	947	794
<i>BJLT</i> 27	.02	1005	770
<i>BJLT</i> 38	.01	920	775
9P	.01	895	753
Standard PC			
2A	.01	1031	852
Standard SC			

The specific heat from 1-6K for *BJLT* crystals 19 and 31 (which are representative of all *BJLT* crystals) is shown in figures 5.31 and 5.32 with standard 2A serving as a reference. Clearly the high temperature anomaly is suppressed in these crystals and shifted down in temperature compared to the standard. Relevant parameters are given in table 5.11 for all *BJLT* samples. The size of the anomaly (ΔC_{max}) is calculated by subtracting the value of C at the onset of the anomaly from the maximum (C_{max}) which is located at T_{max} . We may gauge the extent of the suppression by calculating the ratios T_{max}/T_{max0} and $\Delta C_{max}/\Delta C_{max0}$. Sample 2A served as the reference for T_{max0} and ΔC_{max0} . The dramatic reduction of the entropy associated with the high temperature anomaly in *BJLT* UBe_{13} compared to the standard suggests a comparison of the total entropy from 0-6K may be instructive. In table 5.12 the entropy from $0 \rightarrow T_c$, $T_c \rightarrow 1K$, $1 \rightarrow 6K$, and $0 \rightarrow 6K$ is tabulated for all *BJLT* crystals as well as the 2 standards 2A and 9P. We observe that since the amount of superconducting entropy in the *BJLT* crystals is comparable to that of the UBe_{13} standards, the entropy lost by these crystals from $1 \rightarrow 6K$ is gained back almost entirely in the narrow temperature range between T_c and 1K. This fact allows us to explain the negative entropy mismatch exhibited by the *BJLT* transition discussed above. The value of C/T as $T \rightarrow T_c$ from above is enhanced due to the removal and shifting to lower temperatures of a fraction of the entropy associated with the high temperature anomaly, and not due to an increased density of states at the Fermi level.

In section 2.1.1 it was stated that after subtracting a suitable phonon background ($U_{.97Th.03Be_{13}}$) the remaining f -electron contribution to the UBe_{13} data above 1K could be modeled after a 2-level Schottky scheme, with the addition of a

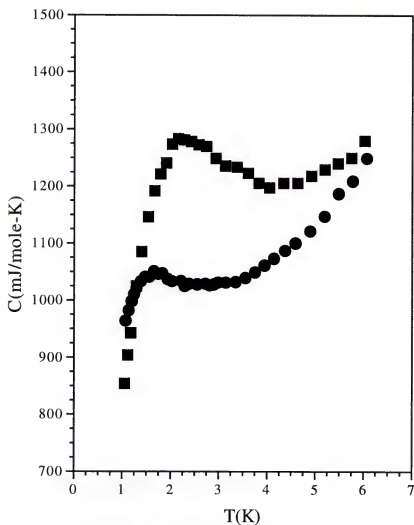


Figure 5.31: The specific heat vs. temperature for *BJLT* crystal 19 (circles) and standard crystal 2A (squares). Note the suppression and shifting to lower temperatures of the standard 2K anomaly in *BJLT* 19. The entropy removed from the anomaly is gained back between T_c and 1K, so the total entropy from $0 \rightarrow 6K$ is the same for standard and *BJLT* UBe_{13} .

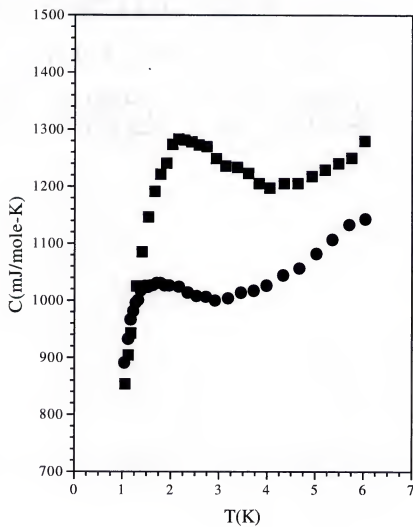


Figure 5.32: The specific heat vs. temperature for *BJLT* crystal 31 (circles) and standard crystal 2A (squares).

Table 5.11: High temperature specific heat parameters for the *BJLT* crystals and 2 UBe_{13} standards.

Sample Description	T_{max} (K)	ΔC_{max} ($\frac{mJ}{mole-K}$)	T_{max}/T_{max0}	$\Delta C_{max}/\Delta C_{max0}$
<i>BJLT</i> 30	$1.63 \pm .08$	28 ± 2	.70	.35
<i>BJLT</i> 31	1.75	25	.75	.31
<i>BJLT</i> 19	1.67	20	.71	.25
<i>BJLT</i> 28	1.68	25	.72	.31
<i>BJLT</i> 29	1.76	35	.75	.44
<i>BJLT</i> 24	1.74	42	.74	.53
<i>BJLT</i> 21	1.75	24	.75	.30
<i>BJLT</i> 27	1.69	21	.72	.26
<i>BJLT</i> 38	1.73	27	.74	.34
9P	2.27	150	.97	1.88
Standard PC				
2A	2.34	80	1	1
Standard SC				

Table 5.12: Superconducting, high temperature, and total entropy for the *BJLT* crystals and 2 *UBe₁₃* standards.

Sample Description	$S_{0 \rightarrow T_c}$ ($\frac{mJ}{mole-K}$)	$S_{T_c \rightarrow 1}$ ($\frac{mJ}{mole-K}$)	$S_{1 \rightarrow 6}$ ($\frac{mJ}{mole-K}$)	$S_{0 \rightarrow 6}$ ($\frac{mJ}{mole-K}$)
<i>BJLT</i> 30	805 \pm 24	289 \pm 9	1837 \pm 55	2931 \pm 88
<i>BJLT</i> 31	799	279	1829	2907
<i>BJLT</i> 19	785	286	1882	2953
<i>BJLT</i> 28	734	264	1826	2824
<i>BJLT</i> 29	720	256	1835	2811
<i>BJLT</i> 24	810	274	1850	2934
<i>BJLT</i> 21	794	276	1862	2932
<i>BJLT</i> 27	770	259	1842	2870
<i>BJLT</i> 38	775	264	1880	2919
9P	754	80	2137	2971
Standard PC				
2A	852	81	2110	3043
Standard SC				

third adjustable parameter equal to the concentration of f -ions present with split levels. A similar procedure was attempted for the *BJLT* crystal data above 1K and proved unsuccessful. The results for *BJLT* crystal 19, which is typical of all *BJLT* crystals, are shown in figure 5.33. We also include the results of a similar fit to standard UBe_{13} in figure 5.34.

A standard two level Schottky fit to the data for *BJLT* 19 failed completely to fit the data, and resulted in highly unphysical fitting parameters. Only by adding a third parameter *and* fixing this parameter at the 6% level stated previously in section 2.1.1 do we obtain reasonable fit parameters (a level splitting of 4K and a degeneracy ratio of .7). As we can see, however, this fit is unsatisfactory. The cause of the U split levels responsible for this high temperature anomaly has yet to be found. However, it is clearly an intrinsic effect because as we have seen, the reduction of this anomaly results in a transfer of entropy to lower temperatures such that the total entropy from 0-6K is conserved. It is interesting to note that while ΔC_{T_c} (an intrinsic parameter) is greatly enhanced in these *BJLT* systems the value of $\gamma(0)$ is not, and this is in stark contrast to the effects seen in $U_{.97}Th_{.03}Be_{13}$. In that system it was observed that the suppression of the high temperature anomaly resulted in a factor of 2 increase in the value of $\gamma(0)$ as well as 2 superconducting peaks [106]. The lack of any increased magnetic response of the *BJLT* ground state down to 1.8K compared to the standard UBe_{13} ground state suggests that maybe the combination of structural and/or site-specific effects on the U -ions (the local U environment is clearly inhomogeneous and changes drastically in going from the standard to the *BJLT* lattice as is evidenced by the expansion of the lattice and the presence of Al) play a role in the cause and subsequent suppression of

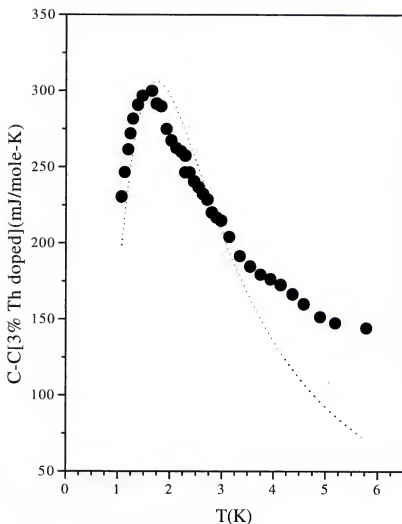


Figure 5.33: The f -electron contribution to the specific heat of $BjLT$ crystal 19 vs. temperature with a 3 term Schottky fit. This best fit was obtained by fixing the third adjustable parameter (the U -ion concentration contributing the the split level system) at the 6% level and varying the level degeneracy and splitting. Only in this way could a fit be obtained. While the parameters obtained from this procedure were similar to those for standard UBe_{13} (a level splitting of 4K and a degeneracy ratio of .7) the fit is obviously very poor. A standard two level Schottky scheme completely failed to describe these data.

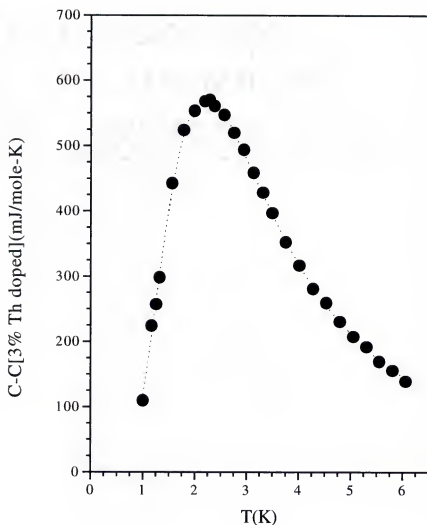


Figure 5.34: The f -electron contribution to the specific heat of a standard UBe_{13} crystal vs. temperature with a 3 term Schottky fit. The parameters obtained from this fitting procedure were a U -ion concentration, or amplitude, of 5%, a level splitting of 7K, and a degeneracy ratio of .2. A standard two level Schottky scheme completely failed to describe these data.

this anomaly. We note that a similar anomaly centered around 5K in $CeBe_{13}$ has been attributed to the presence of 1-3% trivalent Ce atoms [118]. The Ce valence appears to be dependent on the local environment as it evolves continuously as a function of La doping.

5.4.1 Polycrystalline Data

All *BJLT* specific heat results presented so far have been obtained from as-grown single crystalline samples. The question arises as to whether the *BJLT* effects seen here may be duplicated in polycrystalline material. We address this question in two ways. First, the effects of arc-melting a *BJLT* crystal and essentially creating a polycrystal are investigated. And second, because *EPMA* and x-ray diffraction results give a clear indication that *Al* is present in the *BJLT* lattice, we have prepared *Al* doped polycrystalline UBe_{13} and measured the low temperature and high temperature specific heat in the unannealed and annealed states.

Large portions of *BJLT* crystals 21 and 24 (25mg and 17mg respectively) were cleaved from their mother crystals and subjected to arc-melting. The samples (21*M* and 24*M*) were melted once to avoid any complications due to excessive *Be* weight loss. We have already seen from the *EPMA* results and *BSE* photos of section 5.1 that melting has a subtle effect on the *Al* distribution in *BJLT* crystals 21 and 24. Specifically, the large concentrated *Al* rich islands are dissipated after melting while the overall *Al* inhomogeneity is maintained. With this point in mind we compare melted and as-grown specific heat results for *BJLT* crystals 21 and 24 in figures 5.35 and 5.36. A comparison of the as-grown and melted properties

of UBe_{13} standard crystal *JS1* is shown in figure 5.37. Microprobe analysis of standard *JS1* gave no indication for the presence of *Al* in the lattice. The relevant parameters for all crystals are given in table 5.13.

Table 5.13: Specific heat parameters used to compare as-grown and melted *BJLT* crystal 21 and 24, and standard *JS1*.

Sample Description	T_c (K)	ΔC_{T_c} $(\frac{mJ}{mole-K})$	$C/T(T_c)$ $(\frac{mJ}{mole-K^2})$	$C/T(1K)$ $(\frac{mJ}{mole-K^2})$
<i>BJLT</i> 21	$.74 \pm .04$	2638 ± 132	1145 ± 57	980 ± 49
<i>BJLT</i> 21M	.74	481	1010	860
Melted				
<i>BJLT</i> 24	.74	2100	1162	984
<i>BJLT</i> 24M	.74	482	980	800
Melted				
<i>JS1</i>	.91	2239	840	800
Standard SC				
<i>JS1M</i>	.85	1530	810	780
Melted				

After melting, the *BJLT* T_c is unchanged while ΔC_{T_c} is reduced by roughly 80%. Melting also has little effect on T_c for standard *JS1* (within our $\pm 5\%$ error bars) while ΔC_{T_c} is reduced by only 30%. It is important to note that our studies of the sample dependence of ΔC_{T_c} in UBe_{13} single crystals indicate that different portions of the same crystal may give values which differ by as much as 15%. Two such portions of *BJLT* crystal 21 were measured and may be compared in figure 5.38. However, it is clear that this slight sample dependence is insufficient to produce the radical reduction in ΔC_{T_c} observed in figures 5.35 and 5.36. These data suggest that it is the *Al* trapped inside the *single crystalline BJLT* lattice which is responsible for the novel superconducting transition observed. Once the *BJLT*

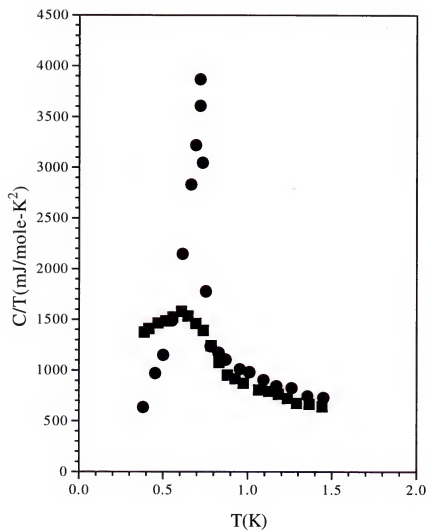


Figure 5.35: The specific heat divided by temperature vs. temperature for as-grown (circles) and melted (squares) *BJLT* crystal 21. Upon melting, T_c for this crystal is unchanged while ΔC_{T_c} is reduced by $\sim 85\%$.

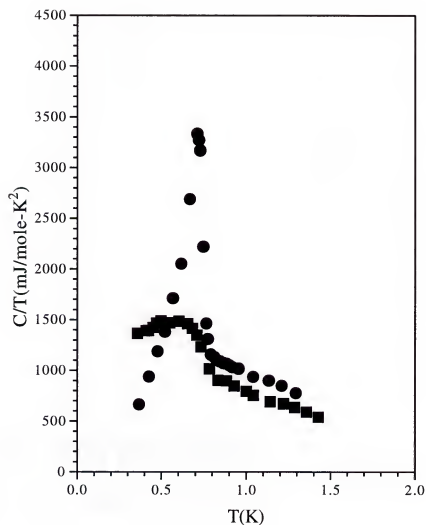


Figure 5.36: The specific heat divided by temperature vs. temperature for as-grown (circles) and melted (squares) *BJLT* crystal 24. Upon melting, T_c for this crystal is unchanged while ΔC_{T_c} is reduced by $\sim 75\%$.

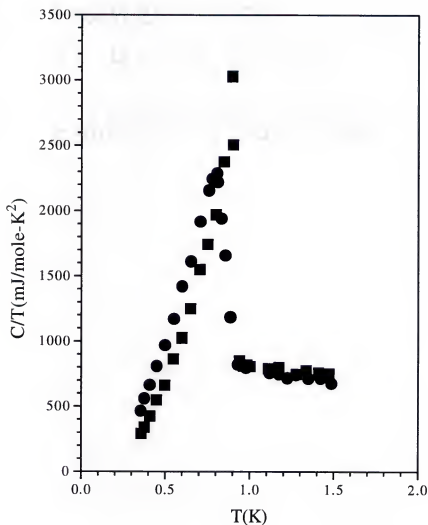


Figure 5.37: The specific heat divided by temperature vs. temperature for standard UBe_{13} crystal JS1 as-grown (squares) and melted (circles). T_c is not altered upon melting, while ΔC_{T_c} is reduced by $\sim 30\%$. Note that the sample dependence of ΔC_{T_c} has been shown to be $\sim 15\%$ (figure 5.38).

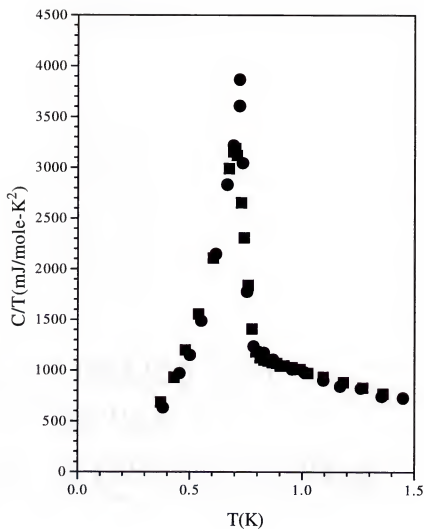


Figure 5.38: The specific heat divided by temperature vs. temperature for two sections of *BJLT* crystal 21. Note that T_c is identical for both pieces, while ΔC_{T_c} seems to indicate a roughly 15% sample dependence.

single crystalline lattice is perturbed via arc-melting, creating a polycrystalline lattice, subtle changes in the *Al* distribution along with possible structural changes incurred during the *Al* redistribution combine to produce a more traditional, impurity dominated superconducting ground state. Once again we stress that T_c is unaffected by the redistribution of the *Al*. These changes affect the normal state as well. In figures 5.39 and 5.40 we plot the normal state specific heat for as-grown and melted *BJLT* crystals 21 and 24 respectively. Clearly, melting the *BJLT* crystals and redistributing the *Al* has resulted in an almost complete suppression of the 2.5K anomaly in C which is often associated with *f*-electron behavior, such as spin fluctuations or a 2-level Schottky system. What is interesting is that the reduction of this anomaly to temperatures below T_c for the melted crystals is associated with a suppression of ΔC_{T_c} . Thus the relationship between changes in ΔC_{T_c} and T_c and ΔC_{max} and T_{max} appears rather complex. A comparison with unannealed and annealed *Al* doped polycrystalline UBe_{13} gives further insight.

In figures 5.41 and 5.42 we plot the low temperature specific heat results for samples 21*M*, 24*M*, and unannealed polycrystalline $UBe_{12.89}Al_{.11}$. The similarity between the melted *Al* rich *BJLT*, and the *Al* doped polycrystalline data is clear. We note that according to the data in table 5.5 the *Al* content of melted *BJLT* crystals and the *Al* doped polycrystal is similar. This indicates, as stated above, that the formation of the novel *BJLT* ground state is not due only to the presence of *Al* in the lattice, but is a result of possible *Al* induced structural anomalies incurred during the growth process and/or preferential *BeI* site occupation by the *Al* impurity. A look at the high temperature specific heat in figure 5.43 reveals that,

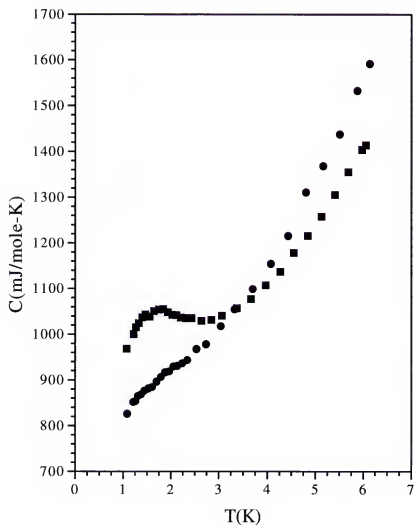


Figure 5.39: The specific heat vs. temperature for as-grown (squares) and melted (circles) *BJLT* crystal 21. Note the almost complete suppression of the anomaly for the melted (polycrystalline-like) sample compared to the as-grown *BJLT* crystal.

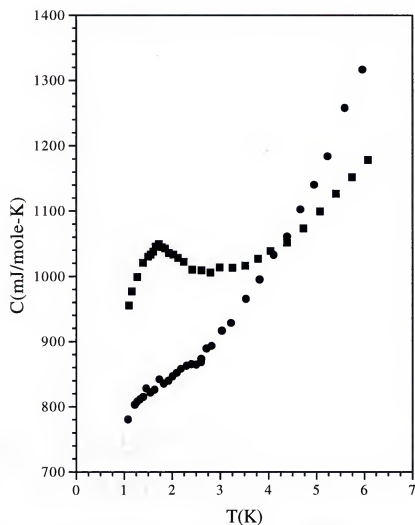


Figure 5.40: The specific heat vs. temperature for as-grown (squares) and melted (circles) *BJLT* crystal 24. Note the almost complete suppression of the anomaly for the melted (polycrystalline-like) sample compared to the as-grown *BJLT* crystal.

as expected, the unannealed polycrystalline $UBe_{12.89}Al_{.11}$ data are very similar to those of melted *BJLT* crystal 21.

We know that for *B* doped UBe_{13} the *B* impurity resides solely on the *Be*I lattice site, and polycrystalline $UBe_{12.97}B_{.03}$ displays an enhanced ΔC_{T_c} albeit with a standard T_c of $\sim 9K$. However, the small *Al* concentrations present in the *BJLT* samples makes direct site determination impossible via the available techniques. We do know from *EPMA* and x-ray diffraction data (sections 5.1 and 5.2) that melting the *BJLT* crystals dissipates the large *Al* rich islands formed during the growth process, and that the lattice parameters of the as-grown *BJLT* and annealed $UBe_{12.89}Al_{.11}$ systems are similar. What may we learn from the specific heat of annealed $UBe_{12.89}Al_{.11}$?

Annealing is one method often used to affect changes in a crystalline lattice. Thus in order to further investigate the nearness of the *Al* doped UBe_{13} polycrystalline ground state to the single crystalline *BJLT* ground state, the specific heat of annealed $UBe_{13-x}Al_x$ ($x=.11, .2$) was measured. The samples were annealed for 5 hours at $1400^\circ C$ and then cooled to $1000^\circ C$ at a rate of $15^\circ C/hour$. This was the same protocol used for growing the single crystals from batch #7 (see table 1.1). We have also annealed a small portion of *BJLT* crystal 30 at $1400^\circ C$ for 504 hours to investigate the effects of long-term high temperature annealing on the *BJLT* ground state. The polycrystalline data are presented in figures 5.44 and 5.45, and table 5.14. The data for *BJLT* 31 and standard 2A serve as a reference.

The effect of annealing on the low temperature specific heat of $UBe_{12.89}Al_{.11}$ is dramatic and results in a relatively sharp, enhanced superconducting transition at a significantly reduced T_c when compared to standard 2A. The data in

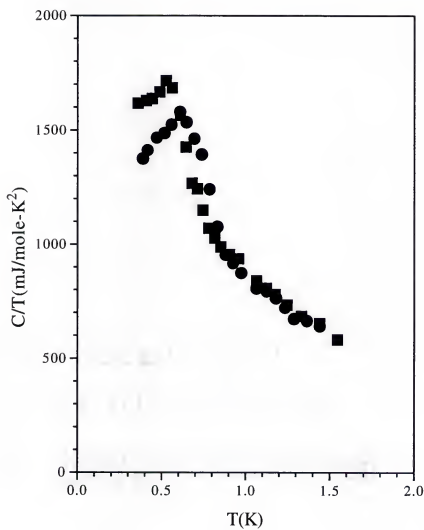


Figure 5.41: The specific heat divided by temperature vs. temperature for melted *BJLT* crystal 21*M* (circles) and unannealed $UBe_{12.89}Al_{1.11}$ (squares).

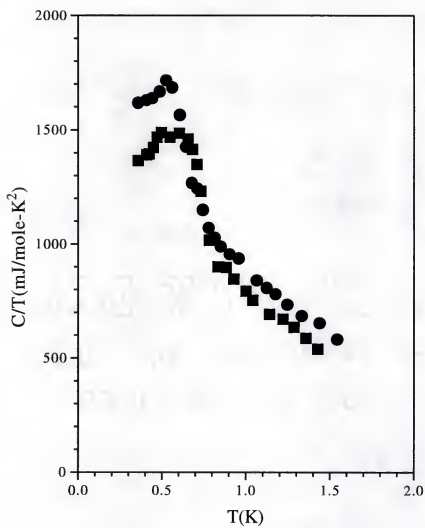


Figure 5.42: The specific heat divided by temperature vs. temperature for melted *BJLT* crystal 24M (circles) and unannealed $UBe_{12.89}Al_{11}$ (squares).

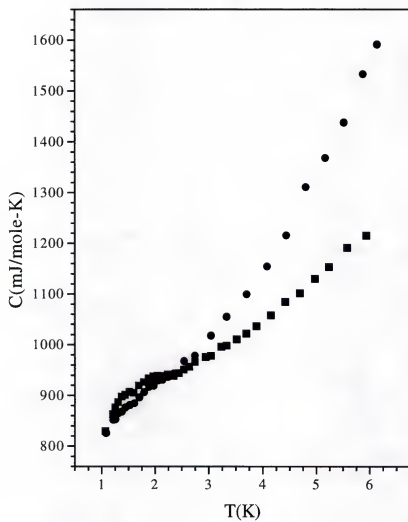


Figure 5.43: The specific heat vs. temperature for melted $BJLT$ crystal $21M$ (circles) and unannealed $UBe_{12.89}Al_{11}$ (squares).

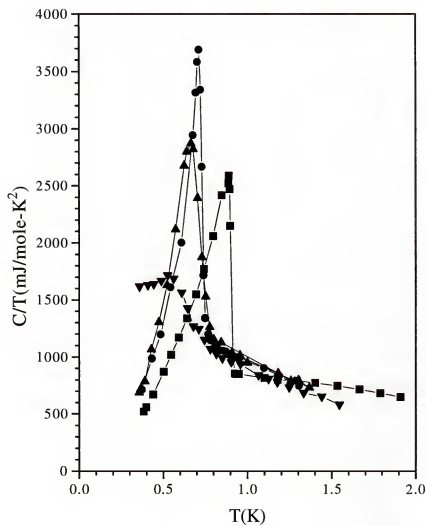


Figure 5.44: The specific heat divided by temperature vs. temperature for unannealed (downtriangles) and annealed (uptriangles) $UBe_{12.89}Al_{11}$, *BJLT* crystal 31 (circles), and standard UBe_{13} crystal 2A (squares). We see here the dramatic effect annealing has on the superconducting ground state of $UBe_{12.89}Al_{11}$.

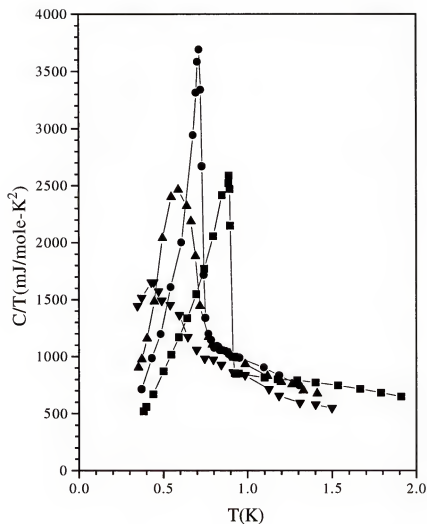


Figure 5.45: The specific heat divided by temperature vs. temperature for unannealed (downtriangles) and annealed (uptriangles) $UBe_{12.80}Al_{20}$, *BJLT* crystal 31 (circles), and standard UBe_{13} crystal 2A (squares). When compared to the data of figure 5.44, the data contained here indicate that an *Al* concentration of Al_{20} is too much to produce to enhanced ΔC_{T_c} upon annealing as is seen for $UBe_{12.89}Al_{11}$.

Table 5.14: Specific heat parameters used to compare annealed and unannealed $UBe_{13-x}Al_x$ ($x = .11, .20$).

Sample Description	T_c (K)	ΔC_{T_c} $(\frac{mJ}{mole-K})$	$C/T(T_c)$ $(\frac{mJ}{mole-K^2})$	$C/T(1K)$ $(\frac{mJ}{mole-K^2})$	$\gamma(0)$ $(\frac{mJ}{mole-K^2})$
$UBe_{12.89}Al_{.11}$ Unannealed PC	$.75 \pm .04$	616 ± 31	1028 ± 51	830 ± 47	****
$UBe_{12.89}Al_{.11}$ Annealed PC	.71	1798	1197	988	1036 ± 52
$UBe_{12.80}Al_{.20}$ Unannealed PC	.55	441	102	818	****
$UBe_{12.80}Al_{.20}$ Annealed PC	.66	1634	1188	942	1262
<i>BJLT</i> 31	.73	2283	1127	955	1058
2A	.91	1705	852	837	1031
Standard SC					

table 5.14 show us that T_c for unannealed and annealed $UBe_{12.89}Al_{.11}$ remains approximately constant within our error bars, while T_c for $UBe_{12.8}Al_{.2}$ increases slightly after annealing. In both cases ΔC_{T_c} is enhanced by roughly a factor of 3 while the transition width decreases by roughly .2K. What is most impressive is the fact that the SCGP type of annealing attempted here has resulted in a ΔC_{T_c} for $UBe_{12.89}Al_{.11}$ which is equal to that of standard 2A, as well as a nominal value of $\gamma(0)$. It appears from these data that the optimum polycrystalline Al content necessary to produce an enhanced specific jump at T_c upon annealing may be $Al_{.11}$. An equal entropy analysis reveals that, like all *BJLT* single crystals, annealed polycrystalline $UBe_{12.89}Al_{.11}$ possesses a negative mismatch at T_c of -7%. Annealed $UBe_{12.80}Al_{.20}$ appears much more standard-like, and has a calculated entropy mismatch of +3%. A comparison of the effects of annealing in these

Al doped systems to pure UBe_{13} proves very interesting. Annealing high purity UBe_{13} for 3.5 weeks at $1200^{\circ}C$ increases ΔC_{T_c} by $\sim 15\%$, has no effect on T_c , and decreases the transition width by $\sim 0.03K$ [106]. It is thus very surprising that the SCGP annealing procedure attempted here, where presumably the redistribution and homogenization of a measurable quantity of *Al* impurity takes place, results in such a dramatic improvement of the superconducting transition. The similarity of the data in table 5.14 for the annealed 11% *Al* doped sample and *BJLT* crystal 31 is an indication that the 11% *Al* doped ground state is possibly more nearly *BJLT*-like than other *Al* impurity concentrations.

A look at the high temperature specific heat in figures 5.46 and 5.47 shows us that after polycrystalline $UBe_{12.89}Al_{.11}$ is annealed according to the single crystalline growth protocol, the high temperature anomaly is largely restored and both ΔC_{max} and T_{max} approach *BJLT* values. Thus an increase in ΔC_{max} and T_{max} after annealing seems to be associated with the enhancement of ΔC_{T_c} for the *Al* doped polycrystals, while T_c is unaffected. This indicates that the relationship between the low and high temperature specific heat peaks of UBe_{13} is possibly more complex than originally suspected.

We now address the effects of annealing on *BJLT* crystal 30. A section of this sample was annealed at $1400^{\circ}C$ for 504 hours. The data are shown in figure 5.48 and in table 5.15. Clearly, long term high temperature annealing has driven the *BJLT* system into a standard, "nominally pure", superconducting ground state. Thus, based on this observation and our previous observation of the effects of annealing on creating a *BJLT*-like ground state in polycrystalline $UBe_{12.89}Al_{.11}$, we can say that the specific *Al* distribution among the *Be* lattice sites that causes

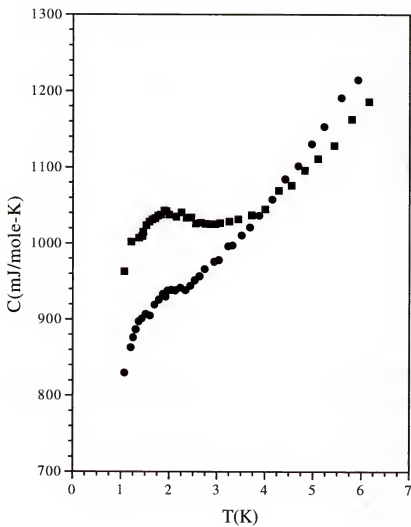


Figure 5.46: The specific heat vs. temperature for unannealed (circles) and annealed (squares) $UBe_{12.89}Al_{11}$. Annealing has resulted in the return of a fraction of the high temperature anomaly in C and, as we have seen, a significant enhancement of ΔC_{T_c} .

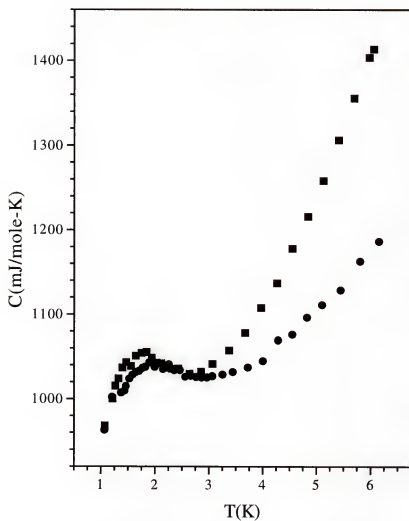


Figure 5.47: The specific heat vs. temperature for annealed $UBe_{12.89}Al_{11}$ (squares) and as-grown BJLT crystal 21 (circles). Annealing has resulted in the return of a fraction of the high temperature anomaly in C in $UBe_{12.89}Al_{11}$, making the data very similar to those of the BJLT crystal.

the *BJLT* properties seen here is a metastable low(er) temperature property that long-term high temperature annealing destroys. We observe that T_c has been increased by 20% while $C/T(1K)$ has been reduced by over 12%. An equal entropy construction yields an entropy mismatch at T_c for annealed crystal 30 of +3%, while that of the unannealed portion was -3%. It is interesting to note that even with such a change in the entropy balance between these two crystals, both the superconducting entropies and the values of $\gamma(0)$ are identical to within 3%, which is just inside our estimated error for these quantities. The equality of the values for $\gamma(0)$ lends further support to our assertion that the shifting to lower temperatures of the high temperature anomaly has a pronounced effect on the value of $C/T(1K)$, and that our linear extrapolation used to ensure entropy balance at T_c determines a more physically relevant parameter ($\gamma(0)$) which may be used in subsequent calculations. It is apparent from figure 5.44 that the values of $C/T(1K)$ and $C/T(T_c)$ are somewhat enhanced for the annealed 11% *Al* doped polycrystal over the unannealed polycrystal. As we have discussed it is incorrect to view the enhancement of C/T as a direct result of an increased effective mass (the relationship between the two was given in section 1.1.1).

5.4.2 Specific Heat in Magnetic Field

An alternate method to look for changes in m^* is to measure the specific heat as a function of magnetic field and calculate the slope of the upper critical field versus temperature as $T \rightarrow T_c$. This slope (H'_{c2}) is directly proportional to m^* . The low temperature specific heat of *BJLT* crystal 19 was measured in magnetic fields of 0, .2, .4, .6, .8, 1, 3, 4, 4.5, and 10T. The results are plotted in figure 5.49.

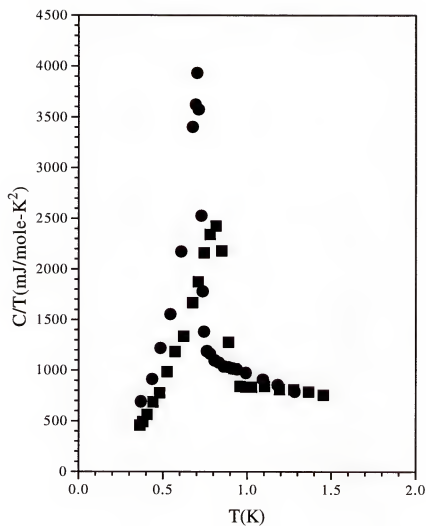


Figure 5.48: The specific heat divided by temperature vs. temperature for unannealed (circles) and annealed (squares) *BJLT* crystal 30. Long term high temperature annealing of the *BJLT* ground state evidently forces *Al* out of the lattice and results in a standard UBe_{13} ground state. Note that when comparing these data the superconducting entropy and $\gamma(0)$ are essentially equal.

Table 5.15: Specific heat parameters used to compare annealed and unannealed *BJLT* crystal 30.

Sample Description	T_c (K)	ΔC_{T_c} ($\frac{mJ}{mole-K}$)	$C/T(1K)$ ($\frac{mJ}{mole-K^2}$)	$\gamma(0)$ ($\frac{mJ}{mole-K^2}$)	S_{sc} ($\frac{mJ}{mole-K}$)
<i>BJLT</i> 30	$.72 \pm .03$	2429 ± 121	966 ± 48	1085 ± 55	805 ± 24
<i>BJLT</i> 30 Annealed	.86	1951	841	1054	828
2A	.91	1705	837	1031	852
Standard SC					

We also plot H_{c_2} versus T_c in figure 5.50. For comparison purposes we have also measured the specific heat as a function of field ($C(H)$) for standard 2A in fields of 0, .2, .4, .6, .8, 1, 3, 5, 6, 7, and 10T and present the results in figures 5.51-5.52.

These data contain 3 features we would like to discuss. We begin with the slope H'_{c_2} as $T \rightarrow T_c$. By translating the data for crystal 19 upwards in temperature so they coincide with the data for crystal 2A a direct comparison of the 2 may be made. This is done in figure 5.53, where we concentrate on the low field data. The slopes calculated from these data (for $0 \leq H \leq .6T$) give values for H'_{c_2} of 56T/K $\pm 5T/K$ and 50T/K $\pm 2T/K$ for samples 19 and 2A respectively. Both values are consistent with previous reports on UBe_{13} , and we conclude from this that the measurement of H'_{c_2} for the *BJLT* crystals gives no indication of an enhanced effective mass in these crystals. Also, the large values of H'_{c_2} observed for both the standard and *BJLT* samples suggests that both ground states are highly (equally) insensitive to applied magnetic fields. This feature of standard UBe_{13} has been cited to argue for an anisotropic *p*-wave ground state, since the parity of such a state would imply parallel Cooper pair spins, both of which would

be affected equally by the applied field, rendering a minimal field dependence for the condensation energy. So, we may also conclude that since the magnitude of H'_{c_2} for the *BJLT* ground state is equal to that of standard *UBe₁₃*, both systems have similar superconducting ground states.

Next, we compare the H_{c_2} data for both crystals over the entire range of temperatures. This is seen in figure 5.54, where we have once again shifted the data for crystal 19 up in temperature to facilitate a direct comparison. What is clear from this figure is that by $H = 4.5T$ the data for the 2 samples begin to diverge. The slope of the data for standard 2A is essentially constant with increasing field, while that of *BJLT* 19 begins to decrease slightly. By 4.5T, H_{c_2} for crystal 19 has decreased by $\sim 6\%$ compared to standard 2A. Similar measurements on *BJLT* crystals down to lower temperatures show that, compared to standard *UBe₁₃*, the slope of the *BJLT* data continues to flatten out with increasing field. We have already seen in section 2.2.2 that this saturation and decrease in the slope of H_{c_2} above 6T is also observed in some standard single crystalline *UBe₁₃* samples, while polycrystalline data reveal an increasing slope above 6T with no sign of saturation. Interestingly, the conclusion that increased sample quality leads to saturation in H_{c_2} [86] would not appear to apply in the case of *BJLT* crystals due to the observed presence and nonuniform distribution of Al in the lattice. It is important to note that the method used to determine $T_c(H)$ appears to influence whether or not saturation is observed. Saturation in the data occurs when $T_c(H)$ is determined via an onset-like criterion, thereby avoiding any uncertainties in $T_c(H)$ due to broadening of the transition in field. The H_{c_2} data shown here were analyzed via the equal entropy, mid-point technique discussed previously. We compare the *BJLT*

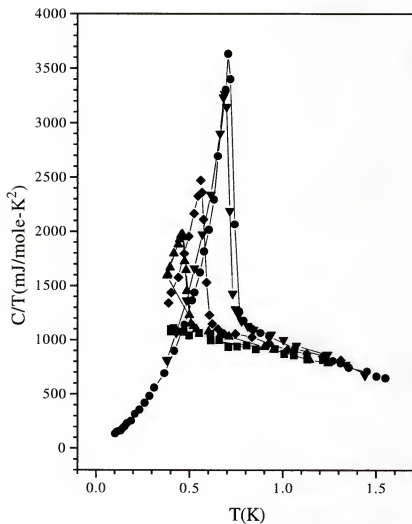


Figure 5.49: The specific heat divided by temperature vs. temperature for *BJLT* crystal 19 as a function of applied field (H). The data shown are 0T (circles), 1T (downtriangles), 3T (diamonds), 4T (triangles), and 10T (squares). Data taken from .2T \rightarrow .8T has been omitted for clarity. Note the suppression of the 10T data. The lines drawn are intended as a guide to the eye.

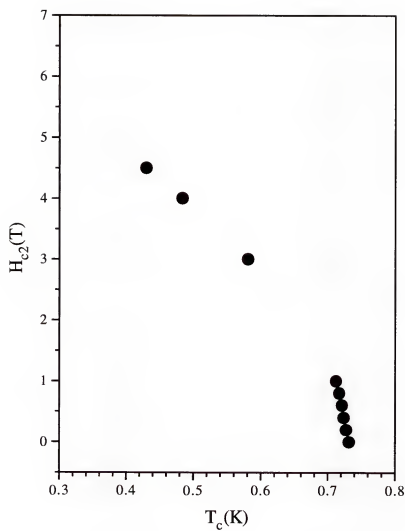


Figure 5.50: The upper critical field (H_{c2}) vs. T_c for BJLT crystal 19.

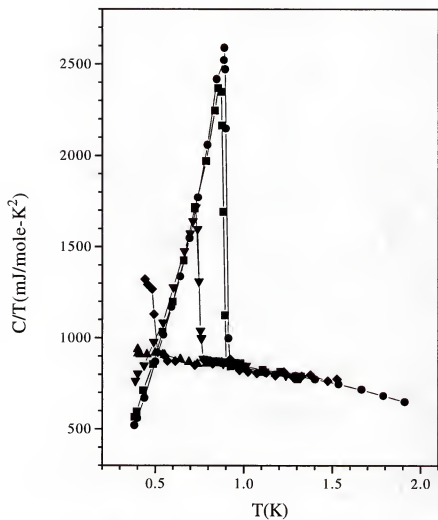


Figure 5.51: The specific heat divided by temperature vs. temperature for standard crystal 2A as a function of applied field (H). The data shown are 0T (circles), .8T (squares), 3T (downtriangles), 6T (diamonds), and 10T (triangles). Other field data have been omitted for clarity. The lines are intended as a guide to the eye.

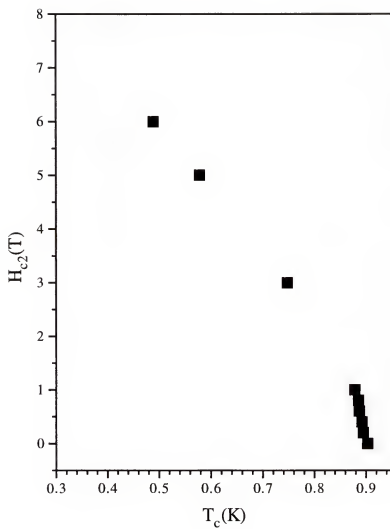


Figure 5.52: The upper critical field (H_{c2}) vs. T_c for standard crystal 2A.

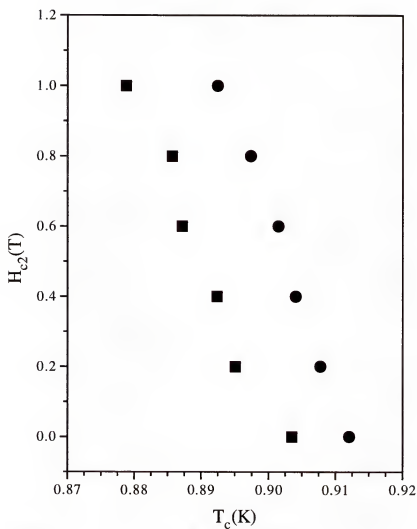


Figure 5.53: The upper critical field (H_{c2}) vs. T_c for standard crystal 2A (squares) and BJLT crystal 19 (circles) in the low field regime, where the original BJLT data have been shifted up in temperature to facilitate a direct comparison. Analysis of the low field slope ($H=0 \rightarrow 0.6\text{T}$) gives no indication for an enhanced effective mass in the BJLT crystal.

data here to our standard 2A, which was analyzed in an identical manner, and not to standard data analyzed previously using different criterion. Our analysis of $H_{c2}(T)$ for *BJLT* crystal 19 seems to indicate that, as far as the effects of magnetic fields on the superconducting ground state are concerned, the *BJLT* state shows a slightly increased saturation in field over standard UBe_{13} . As we approach T_c , H'_{c2} for the *BJLT* ground state is essentially equal to that of standard UBe_{13} and suggests similar superconducting ground states.

Finally, we would like to address the slight ($\sim 10\%$) but real suppression of the specific heat data around 1K taken in 10T for crystal 19 (see figure 5.49). This effect was not observed in standard 2A as is clear from figure 5.51. This interesting field dependence was also verified for *BJLT* crystal 31 which was measured in 9T, and is shown in figure 5.55. This type of field dependence has been observed before in UBe_{13} [99]. In this case we explain the effect by noting that the field dependence and suppression of the high temperature specific heat anomaly in pure and doped UBe_{13} is well known [119, 99, 120]. The normal state specific heat is reduced by about 10% in 13T at 2K. Data also indicate that the suppression of the specific heat data at 1K increases by only 2% as the applied field is increased from 9T to 15T. The suppression in 15T at 1K is $\sim 6\%$ and reaches 9% by 1.8K. We have seen that the high temperature anomaly of the *BJLT* crystals is suppressed and shifted down to lower temperatures. This shift is roughly .65K. Thus the observed field dependence around 1K is due to the suppression of that part of the high temperature anomaly which extends to these lower temperatures in the *BJLT* crystals.

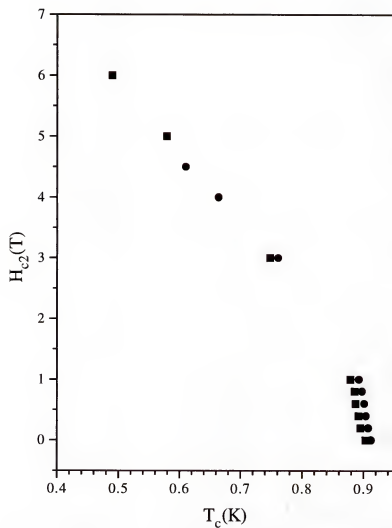


Figure 5.54: The upper critical field (H_{c2}) vs. T_c for standard crystal 2A (squares) and BJLT crystal 19 (circles), where the original BJLT data have been shifted up in temperature to facilitate a direct comparison.

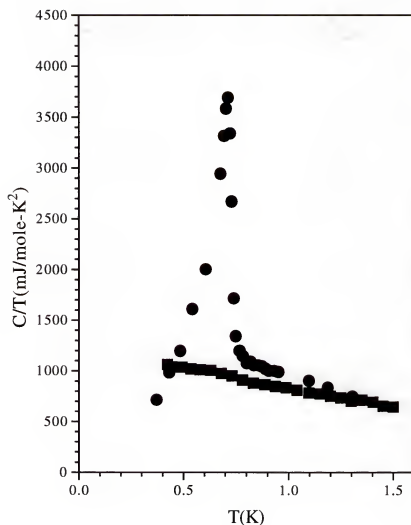


Figure 5.55: The specific heat divided by temperature vs. temperature in a field of 10T for *BJLT* crystal 31. Like *BJLT* crystal 19, this sample also displays a suppression of the specific heat in high fields. We explain this effect by noting that the high temperature 2K anomaly has been shifted to lower temperatures in these samples, and that this anomaly has a well established field dependence.

The specific heat results presented in this section paint an interesting picture of the nature of the *BJLT* superconducting ground state. Low temperature results on as-grown *BJLT* crystals indicate that the novel ground state is characterized by a $\sim 20\%$ reduction in T_c and a ΔC_{T_c} which is enhanced by as much as 50% compared to standard *UBe₁₃*. At the beginning of this chapter we asked several questions concerning the underlying cause of these novel features. Considering the data presented in this section we may now answer those questions. We begin at high temperature.

The results obtained from high temperature specific heat measurements on *BJLT UBe₁₃* indicate that the temperature of the standard 2.5K anomaly is reduced by roughly 30% and the jump in the specific heat is suppressed by $\sim 60\%$ in the *BJLT* crystals. The *f*-electron, 2-level Schottky scheme verified for standard *UBe₁₃* does not appear to exist in *BJLT UBe₁₃*. Attempts to fit the *f*-electron contribution to the specific heat with 2 and 3 parameter Schottky models completely failed to describe the data. Since the local *U* environment is clearly altered in the *BJLT* case, with the addition and nonuniform distribution of *Al* on the *Be* site(s), the destruction of the 2-level system may be the result of certain structure-specific effects since some *U* ions have a different local environment than the remainder of the lattice. The inability of neutron scattering to detect the observed low lying levels (in the standard material) suggests the possible presence of a split-level-conduction electron interaction³. So, the local *U* environment and hybridization between the *U* and conduction electron states appears to play a role in this high temperature split-level system. By altering the environment we al-

³Note that the addition of trivalent *Al* for *Be* adds an additional conduction electron to the system.

ter the system. It is interesting to note that doping experiments on the U site have shown that when the UBe_{13} lattice is contracted the anomaly in C is broadened and shifted to higher temperatures, whereas when the lattice is expanded the anomaly in C is suppressed and shifted to lower temperatures [63]. In the case of the $BJLT$ crystals, we have seen that the lattice is expanded compared to the standard and clearly the anomaly is suppressed and lowered in temperature. It appears that the size of the lattice and changes in the local U environment is critical in determining the fate of the 2.5K anomaly in C . Polycrystalline $UBe_{12.89}Al_{.11}$ displays a suppressed anomaly in C very similar to that of the melted $BJLT$ crystals 21 and 24. We may associate the almost negligible ΔC_{max} and suppressed T_{max} of this anomaly in these samples with a significant alteration in the local f -electron environment. Any f -electron correlations present would also be altered by the changing local environment. Once the polycrystals are annealed according to single crystalline growth specs, a fraction of the high temperature anomaly in C lost during arc-melting is actually returned to the system above T_c , while below T_c ΔC_{T_c} is greatly enhanced and T_c is unaltered. The annealed $UBe_{12.89}Al_{.11}$ data are very similar to the $BJLT$ data. Annealing restores the local f -electron environment to at least a $BJLT$ -like state (recall that annealing results in a migration of a majority of the Al impurity to the cubic BeI site), and those f -electron correlations destroyed by arc-melting are returned. Thus the suppression and shifting to lower temperatures of the 2.5K anomaly does not directly result in the enhanced low temperature ground state of this system, otherwise unannealed $UBe_{12.89}Al_{.11}$, with an almost total suppression of the 2.5K anomaly, would be expected to possess the most enhanced superconducting ground state, when in fact it possesses a

severely suppressed superconducting state. We have also discovered that the entropy lost under the high temperature *BJLT* peak reappears in the specific heat between T_c and 1K, and our data show that the total entropy from $0 \rightarrow 6K$ for the *BJLT* crystals is identical to that of the standard samples. This shift to lower temperatures of the anomaly explains why the value of $C/T(T_c)$ for the *BJLT* crystals is enhanced compared to standard UBe_{13} . By performing an equal entropy construction on all samples we arrive at the correct value of $\gamma(0)$. We move now to low temperature.

Our data clearly indicate that the *BJLT* peak is due to a single superconducting transition and is not due to the admixture of two transitions which occur at nearly the same temperature. The extremely sharp, vertical *BJLT* peaks possess a transition width which is equal to that of standard UBe_{13} . Also, as we have mentioned, within our error bars there is no difference in either the superconducting entropy or $\gamma(0)$ between the standard and *BJLT* samples.

The very low temperature specific heat data of *BJLT* crystal 19 (figure 5.30) suggest that there may be subtle differences in the nodal structure of the superconducting ground state between *BJLT* and standard UBe_{13} . It is not clear that the limiting temperature reached here ($\sim 100mK$) is sufficiently low such that the true structure of $C(T)$ is not masked by higher temperature electronic or Fermi surface effects which are unrelated to the low temperature nodal structure.

By analyzing ΔC_{T_c} and T_c for as-grown and melted *BJLT* crystals 21 and 24, and unannealed and annealed polycrystalline $UBe_{12.89}Al_{.11}$ we have discovered that the depressed T_c observed (which is essentially identical for *ALL* samples) is due solely to the *Al* impurity effect on the anisotropic ground state. Once *Al* is

introduced into the lattice, there appears to be no correlation between the relatively stable (depressed) T_c and the highly variable ΔC_{T_c} . An impurity induced change of symmetry would require that T_c be altered as well in going from unannealed (suppressed ΔC_{T_c}) to annealed $UBe_{12.89}Al_{.11}$ (enhanced ΔC_{T_c}), for example, as all impurities in anisotropic superconductors smooth out the energy gap, act as pair-breakers, and thus reduce T_c . This discovery argues against a change in symmetry (d -wave to s -wave) of the *BJLT* ground state and supports the hypothesis that the large ΔC_{T_c} observed is due to increased strong coupling effects. The strong coupling parameter β is enhanced by at least a factor of 1.5 in going from standard to *BJLT* UBe_{13} . This direct observation of impurity induced increased strong coupling effects in a heavy fermion superconductor is certainly interesting. What makes it even more interesting is that these effects are not due only to the presence of the *Al* impurity, but are also clearly related to the placement of the impurity in the lattice among the *Be* lattice sites.

Since *Al* is clearly a factor in the novel properties observed here, we have attempted to duplicate the single crystalline results in *Al* doped polycrystals, in which the amount of *Al* may be controlled. Our results for $UBe_{13-x}Al_x$ ($x=.11, .20$) indicate that *Al* doping affects ΔC_{T_c} and T_c for the unannealed samples in much the same way as does doping with other elements. We observe that ΔC_{T_c} is suppressed and T_c is reduced. However, once the samples are annealed for only 5 hours at $1400^\circ C$ and then cooled gradually at $15^\circ C/hour$ to $1000^\circ C$ (typical single crystalline growth conditions) the dramatic reduction of the lattice parameters (see table 5.6) is accompanied by an increase in ΔC_{T_c} while T_c is unchanged. This is especially true for $UBe_{12.89}Al_{.11}$, the *Al* content of which is similar to

that of the *BJLT* crystals. After annealing, the superconducting ground state of $UBe_{12.89}Al_{.11}$ is significantly altered as is evidenced by the standard value of ΔC_{T_c} occurring at the reduced T_c of .71K (table 5.14). Note from table 5.5 that the short annealing time and more importantly the slow cool down from 1400°C resulted in a substantial homogenization (and therefore redistribution) of the *Al* impurity and preferential occupation of the *BeI* lattice site. We have also seen in section 5.2 that the 11% *Al* doped x-ray diffraction peaks were consistently 2.5 times wider (FWHM) than the *BJLT* crystal 31 peaks. This is an indication of stress and/or non-uniformity in the crystalline lattice planes and their respective interplanar distances. Thus we are able to approach the *BJLT* ground state in polycrystalline $UBe_{12.89}Al_{.11}$ only when we anneal the arc-melted sample and allow the *Al* impurity to migrate to the *BeI* lattice site. We have also attempted to influence the *Al* distribution of several *BJLT* crystals.

Melting *BJLT* crystals creates essentially polycrystalline material and destroys the *BJLT* ground state. The similarity between the melted *BJLT* and *Al* doped polycrystalline $UBe_{12.89}Al_{.11}$ specific heat data is clear (figures 5.41 and 5.42). However, when we subject the *BJLT* lattice to long term-high temperature annealing the *Al* is forced completely out of the lattice and the specific heat resembles that of standard, *Al*-free UBe_{13} . These results are a clear indication (once again) that it is the presence of *Al* in the lattice which is responsible for the depressed T_c and the position of *Al* in the lattice which affects ΔC_{T_c} . It is also clear from table 5.14 that the superconducting entropy and density of states, determined via $\gamma(0)$, in going from the as-grown *BJLT* to the annealed standard-like ground state is unchanged. This lends further support to our assertion that the large ΔC_{T_c} ob-

served is the result of increased strong coupling effects and not due to an increase in the density of states at the Fermi level. We have also checked this possibility via specific heat measurements in magnetic field.

By measuring the specific heat of *BJLT* crystals 19 and 31 in field and comparing those results to standard 2A we have learned that the superconducting ground states and pairing mechanisms for both systems are similar. We know this because the large value of H'_{c2} , which is a characteristic of all UBe_{13} samples, is unchanged in going from the standard to the *BJLT* ground state. Thus both ground states are extremely (and equally) insensitive to the application of magnetic fields. Also, since this slope is directly proportional to the effective mass (m^*) of the quasi-particles, the equality of the two slopes suggests that there is not an increase in m^* (and therefore $\gamma(0)$) in going from the standard to the *BJLT* state.

5.5 Resistivity and Magnetoresistance

The d.c. resistivity of *BJLT* crystal 31 as well as 4 reference samples was measured by a standard 4-probe technique (see section 4.5 for details). We include data for polycrystalline $UBe_{12.94}Al_{0.06}$ because of the similarity between the lattice constant for this sample (10.265 *Angstroms*) and that of *BJLT* 31 (10.264 *Angstroms*). All data are shown in figure 5.56. Relevant parameters were calculated and are given in table 5.16. These include the temperature (T_{max}) of the maximum resistivity (ρ_{max}), the resistivity ratio $\rho_R = \rho_{300K}/\rho_{1.5K}$, the size of the low temperature maximum $\Delta\rho = (\rho_{max} - \rho_{10K})/\rho_{10K}$, and the width of the resistive anomaly (ΔT_ρ) measured between $\rho = \rho_{max}$ and $\rho = \rho_{max} - \Delta\rho/2$. The values of T_{max} , ρ_{max} , and ρ_R for all samples are seen to be nominal. We note that our error

bars of $\pm 10\%$ for ρ are due mainly to geometrical uncertainties in the size and cross section of the sample. It is well known that UBe_{13} has a tendency to develop small cracks when spot-welded and prepared for such a measurement. No such anomalies were detected for the samples measured in this study. There appears to be no correlation between the single or polycrystalline nature of the samples or the small impurity concentrations present and the resistivity ratio, which is commonly used as a gauge of sample purity. From the data given, the only features which differentiate *BJLT* 31 (an impurity ridden single crystal) from all other samples are the size and width of the resistive anomaly. In both cases the values calculated indicate that the *BJLT* 31 resistive normal state is much more polycrystalline than single crystalline in nature. And, by plotting the resistivity data of crystal 31 and $UBe_{12.94}Al_{0.06}$ together in figure 5.57 it becomes clear that the *BJLT* coherence peak is substantially reduced in magnitude and broadened in temperature even when compared to an apparently similar (based on lattice size) polycrystal. This may be an indication that the *BJLT* crystal does indeed contain more *Al* than the $Al_{0.06}$ polycrystal.

Previous doping studies on UBe_{13} have shown that this low temperature peak is shifted down in temperature when the lattice is expanded, and up in temperature as the lattice is contracted [121].⁴ It has also been observed that neither T_{max} nor ρ_{max} are observed to decrease monotonically with T_c . By applying a field of 11T ρ_{max} is essentially destroyed while the 2.5K anomaly in C is perturbed only slightly. These observations suggest that the low temperature anomaly in ρ and

⁴This behavior of T_{max} with lattice size is similar to that of the 2.5K anomaly in C discussed previously. We also observed from those data that a suppression of the anomaly in C did not necessarily result in a larger ΔC_{T_c} for unannealed $UBe_{12.89}Al_{0.11}$.

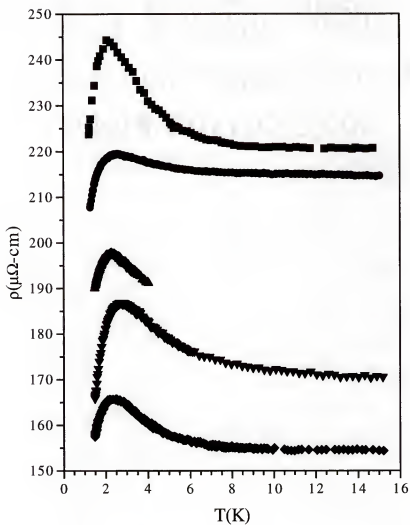


Figure 5.56: The resistivity vs. temperature for *BJLT* crystal 31 (circles), standard polycrystal 9*P* (diamonds), standard polycrystal 7*P* (downtriangles), $UBe_{12.94}Al_{0.06}$ (uptriangles), and standard single crystal 14 (squares).

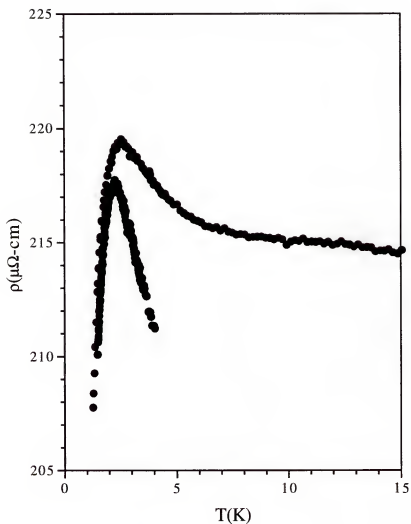


Figure 5.57: The resistivity vs. temperature for *BJLT* crystal 31 (upper curve) and polycrystal $UBe_{12.94}Al_{.06}$ (lower curve). The polycrystalline data have been shifted up in temperature to aid in comparing the two curves. We observe the substantial broadening and suppression of the *BJLT* coherence peak compared to the *Al* doped polycrystal. This may be an indication that the *Al* content of the *BJLT* crystal is greater than $Al_{.06}$.

Table 5.16: Resistivity parameters used to compare *BJLT* crystal 31, $UBe_{12.94}Al_{.06}$, and UBe_{13} standards.

Sample Description	T_c (K)	T_{max} (K)	ρ_{max} $\mu\Omega - cm$	ρ_R	$\Delta\rho$ $\mu\Omega - cm$	ΔT_ρ (K)
<i>BJLT</i> 31	.73 \pm .04	2.56 \pm .05	219 \pm 22	.59	4	2.75 \pm .05
9P	.90	2.34	165	.78	10	2.60
Standard PC						
7P	.93	2.75	187	.64	15	2.68
Standard PC						
$UBe_{12.94}Al_{.06}$.81	2.26	198	.60	7(4K)	2.41(4K)
Unannealed PC						
14	.91	2.25	244	.56	23	2.18
Standard SC						

the superconducting transition in UBe_{13} quite possibly have separate causes. The fact that T_{max} of the resistive anomaly for *BJLT* 31 is not reduced compared to that of the standards listed here, while T_{max} of the high temperature specific heat anomaly is reduced, suggests that these 2 anomalies may have separate causes as well. What can be gleaned from magnetoresistive measurements on this novel material? The magnetoresistance of *BJLT* crystal 31 was measured in fields of 1, 2, 3, 4, 6, 8, 10, 12, and 14T. We plot the resistance as a function of field ($R(H)$) versus temperature (T) in figure 5.58, and the relative magnetoresistance $\Delta R = (R(H, T) - R(0, T))/R(0, T)$ versus temperature in figure 5.59.

According to the data in figure 5.58, ρ_{max} is suppressed and shifted to higher temperatures by applied magnetic fields. The field dependence, through 4T, is quadratic and can be written as

$$T_{max} = T_0 + A \cdot H^2 \quad (5.1)$$

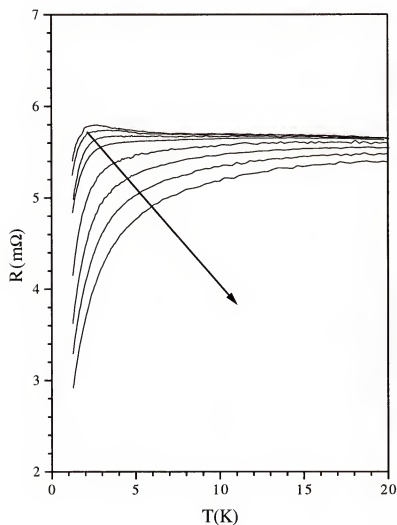


Figure 5.58: The resistivity vs. temperature for *BJLT* crystal 31 as a function of applied field. The arrow points in the direction of increasing field. The data shown were taken in 0, 2, 4, 6, 8, 10, 12, and 14T. The coherence peak moves to higher temperatures with increasing field, and becomes a broad shoulder by 6T.

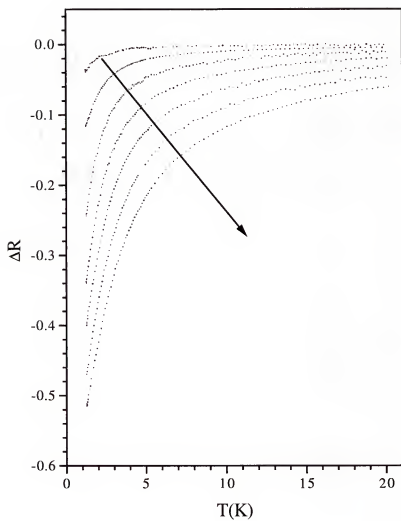


Figure 5.59: The relative magnetoresistance vs. temperature for *BJLT* crystal 31. The arrow points in the direction of increasing field. Data were taken in fields of 2, 4, 6, 8, 10, 12, and 14T.

where $T_0 = 2.56K (\pm .07K)$ and $A = .16K/T^2 (\pm .02K/T^2)$. The value of A obtained here is roughly twice that obtained previously on a standard UBe_{13} single crystal ($T_c = .88K$) [72]. No theory for the field dependence of this resistive anomaly has been proposed to date. Turning now to the relative magnetoresistance in figure 5.59, we observe that it is clearly negative and temperature and field dependent. It is well known that both single and polycrystalline UBe_{13} exhibit the same, unique, scaling relationship in their magnetoresistance which is independent of field orientation (transverse or longitudinal). A similar scaling procedure was attempted for *BJLT* crystal 31 and the results are presented in figure 5.60. Here, we plot ΔR versus $\log[(T + T^*)^\beta / H]$ where $T^* = -.29K$ and $\beta = .57$ for all fields. This scaling approach appears to be very successful. Additionally, the data for each successive pair of fields were analyzed in a similar manner in order to arrive at the range of values (error bars) for T^* and β . As a result of this procedure we calculate that T^* ranges from $-.17K$ to $-.49K$ and β ranges from $.56$ to $.59$. The value of β obtained here compares very well to that of previous reports, while T^* is roughly 3 times less. What this means is unclear. For the two channel Kondo model it has been predicted that $T^* = 0$ and $\beta = .50$. Thus it appears that the relative magnetoresistance of the *BJLT* groundstate may indicate an approach to two channel Kondo behavior in this system.

To summarize, the 0 field resistivity of *BJLT* crystal 31 appears to possess the properties expected from an unannealed, impure single crystal of UBe_{13} . When measured in magnetic field, the low temperature coherence peak is suppressed and shifted to higher temperatures at a rate twice that of standard single crystalline UBe_{13} . The relative magnetoresistance of the *BJLT* ground state is also seen to

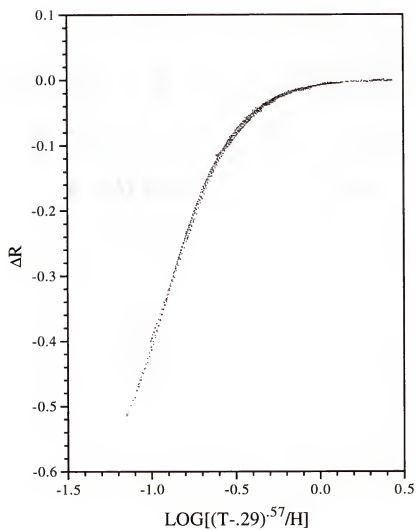


Figure 5.60: The scaled relative magnetoresistance for *BJLT* crystal 31.

display the same, unique scaling relationship as standard single and polycrystalline UBe_{13} . The coefficient β obtained from the scaling is essentially equal to previous values, while the reduced temperature T^* may be an indication of an approach to two channel Kondo behavior.

5.6 Other Studies

During the course of this research we became aware of several simultaneous studies concerning *BJLT* UBe_{13} . In this section we present the results of those studies and discuss their significance in terms of the data presented in this chapter. The first study involved a crystal designated by crystal type "L" [122]. This crystal

Table 5.17: Specific heat parameters for crystal "L" and a comparison to *BJLT* 24 and annealed $UBe_{12.89}Al_{.11}$.

Sample Description	T_c (K)	ΔC_{T_c} ($\frac{mJ}{mole-K}$)	$C/T(T_c)$ ($\frac{mJ}{mole-K^2}$)	$\Delta C_{T_c}/(C/T(T_c) \cdot T_c)$
Crystal "L"	.74	1850	1240	2
<i>BJLT</i> 24	.74	2100	1162	2.44
$UBe_{12.89}Al_{.11}$.71	1798	1197	2.11
Annealed PC				

was claimed to be a variant of single crystalline UBe_{13} which we have designated *BJLT*. However, upon examination of the data presented in that reference it is clear that the specific heat parameters which pertain to this sample are much more like those of our annealed polycrystalline $UBe_{12.89}Al_{.11}$. This is made clear in table 5.17.

By comparing crystal type "L" with annealed $UBe_{12.89}Al_{11}$ and *BJLT* crystal 24 (which displays the smallest ΔC_{T_c} among our 9 *BJLT* samples) we see that even though T_c is reduced in crystal "L", ΔC_{T_c} is still $\sim 12\%$ less than that for crystal 24, while it is equal to (within our 5% error bars) that of the annealed *Al* doped polycrystal. Notice also that $C/T(T_c)$ is similar for all samples. Since the values of ΔC_{T_c} and C_{T_c} for annealed $UBe_{12.89}Al_{11}$ and crystal "L" are essentially equal, we expect that the ratio of these two parameters will also be identical for these samples. This ratio approaches 2 for crystal "L" and 2.11 for annealed $UBe_{12.89}Al_{11}$.⁵ Corrections for proper entropy balance notwithstanding its clear that crystal type "L" does not possess the increased strong coupling effects which are a hallmark of the *BJLT* ground state.⁶ Further analysis of the specific heat data for this crystal reveal an anomalous shoulder in C/T centered around $\sim .45K$. The significance of this anomaly is unknown. However, no such anomaly has been observed in other *BJLT* crystals (see below) and not in the small piece of crystal "L" removed and measured by another group. Measurements of the specific heat in field for crystal "L" revealed a value for H_{c2}' of $-50T/K$, which is certainly in line with our *BJLT* and standard UBe_{13} results of $-56T/K$ and $-50T/K$ for crystals 19 and 2A respectively.

Further work on crystal "L" included analysis of the coefficient of thermal expansion (α). By calculating the jump in α at the onset of superconductivity, designated by $\Delta\alpha$, and using Ehrenfests' relation for the rate of change of T_c with

⁵The authors also claim that a small piece of crystal "L" crystal was cut off and measured by another group, and those results indicated a ratio of 2.6.

⁶By considering an equal entropy construction for annealed $UBe_{12.89}Al_{11}$, we arrive at a strong coupling parameter (β) of 2.44. This falls well below 2.79, the value obtained for *BJLT* crystal 24 and the smallest value of β observed in this study.

pressure, the authors discovered that the pressure dependence of T_c for crystal "L" was 5 times less than that of a UBe_{13} standard. No physical explanation was put forth to explain the difference in this pressure dependence.

So when considering these results it is important to realize that the crystal "L" under investigation is not quite a strong coupled *BJLT* crystal. In fact the similarity of the type "L" and our annealed $UBe_{12.89}Al_{.11}$ results suggests that crystal "L" may be a single crystalline intermediate in much the same way as $UBe_{12.89}Al_{.11}$ appears to be a polycrystalline intermediate. This supports our assertion that subtle impurity induced structural effects play a key role in the formation of the *BJLT* ground state. Evidently the single crystalline growth process experienced by crystal "L" was only slightly altered from that of the true *BJLT* crystals, and as a result the ground state observed is in an intermediate phase. Certainly further study of this crystal would be very interesting, and may help bridge the gap in our understanding of this complex system. The reduced T_c observed is a sign of a lattice impurity, and this is almost certainly *Al*. Investigating the effects of short term high temperature annealing on the specific heat of crystal "L" would prove very interesting. We now examine the results from a second study.

The specific heat data obtained in the next study are a clear indication for true *BJLT* behavior [108]. We label this crystal R1 and present the data in table 5.18 and figure 5.61. While T_c is depressed to .74K for crystal R1, ΔC_{T_c} is significantly enhanced and approaches a value of 2450 mJ/mole-K^2 . Also, the ratio of ΔC_{T_c} to C_{T_c} is roughly 3.18 and is a good indicator that this crystal is a strongly coupled *BJLT* crystal.⁷ The specific heat of crystal R1 was measured as a function of

⁷According to the data presented in this reference there is no sign of an anomaly in C/T at .45K.

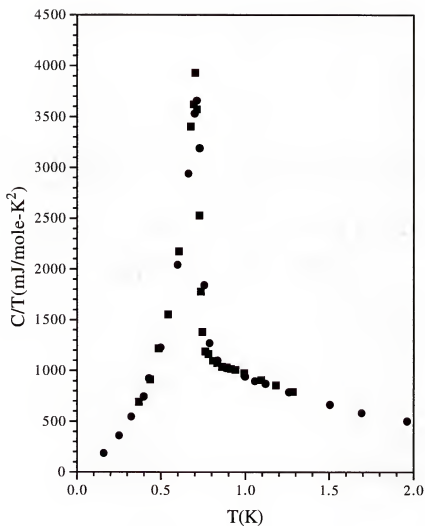


Figure 5.61: The specific heat divided by temperature vs. temperature for *BJLT* crystal 30 (squares) and crystal R1 (circles). The large, narrow superconducting transition of crystal R1 is proof that this crystal possesses a true *BJLT* ground state.

Table 5.18: Specific heat parameters for crystal R1 and a comparison to *BJLT* 30.

Sample Description	T_c (K)	ΔC_{T_c} ($\frac{mJ}{mole-K}$)	$\gamma(0)$ ($\frac{mJ}{mole-K^2}$)	$\Delta C_{T_c}/(\gamma(0) \cdot T_c)$
Crystal R1	.74	2447	1100	3
<i>BJLT</i> 30	.72	2429	1085	3.11

magnetic field, and for fields less than the critical field ($H \leq H_{c2}$) it was discovered that the behavior of $C(H)$ was superlinear. Specifically, the dependence was found to be $C \propto H^2 \cdot T$. From this temperature and field dependence the authors were able to show that this *BJLT* single crystal must possess a superconducting gap with lines of nodes, which is consistent with *d*-wave symmetry. This supports nicely our claim that the increase in the coupling strength parameter β from standard to *BJLT* UBe_{13} is due solely to increased stong coupling effects, and should not be mistaken for a possible change in symmetry from *d*-wave to *s*-wave. It was also discovered, via this analysis, that the difference between the magnetic susceptibility determined with parameters obtained from fitting $C(H, T)$, and the normal state susceptibility, implies that roughly 25% of the entropy lost below T_c is due to the loss of magnetic fluctuations.

The data presented in this study support our assertion that the symmetry of the underlying *BJLT* ground state is identical to that of standard UBe_{13} (where we assume that all evidence to date suggests standard UBe_{13} possesses *d*-wave symmetry). What is equally as interesting is the evidence presented which claims that the *BJLT* ground state may be influenced by magnetic fluctuations, the loss of which makes up $\sim 25\%$ of the total entropy lost below T_c . We note that

a magnetic transition was claimed via thermal expansion measurements on the *BJLT* crystal in this reference, and that β was 70% larger for this crystal than for a standard UBe_{13} crystal which did not show a magnetic anomaly [123, 124]. These thermal expansion results, however, are somewhat controversial due to their lack of reproducibility.

CHAPTER 6

CONCLUSION

To conclude this study we will first review our important findings from the previous chapter. Next, we will compare and contrast our results with those obtained on polycrystalline $UBe_{12.97}B_{.03}$. Possible approaches to understanding these novel superconducting ground states will follow. We close with suggestions for future work.

6.1 Review of Results

Our *EPMA* results on *BJLT* single crystals and polycrystalline $UBe_{13-x}Al_x$ have revealed that the *Al* impurity in all systems resides solely on the *Be* lattice sites, and that it is distributed non-uniformly throughout the lattice. Short-term, high temperature annealing in conjunction with a gradual cool-down allows the *Al* to migrate through the lattice and become more homogeneously distributed in the polycrystals, whereas arc-melting has little effect on the over-all *Al* inhomogeneity of the *BJLT* crystals. However, the large *Al* rich islands in the *BJLT* lattice are significantly dissipated upon melting. Though the *BJLT* ground state is also destroyed after melting, we believe that the presence of these large *Al* rich regions is not responsible for the novel superconducting properties observed. What is important is the observation that *Al* is extremely mobile in the UBe_{13} lattice, and changes in the superconducting ground state (for example an enhanced or

suppressed ΔC_{T_c}) are always observed in conjunction with the displacement of the *Al*. Once introduced into the lattice, the position of the *Al* impurity in the lattice (*BeI* or *BeII* site) and the size of the resulting unit cell appear to be directly related to the observed changes in ΔC_{T_c} . T_c is not affected by the redistribution of the *Al* in all cases. To examine the *BJLT* unit cell in greater detail we have also performed x-ray diffraction studies.

Due to the presence of *Al*, the *BJLT* lattice is expanded over that of standard UBe_{13} . However, this expansion is $\sim 50\%$ less than we expect according to the *EPMA* determined *Al* content and our analysis of the linear relationship between lattice parameter and *Al* concentration in polycrystalline material. What is very interesting is that after annealing for 5 hours at $1400^\circ C$ and cooling to $1000^\circ C$ at $15^\circ C/\text{hour}$, the polycrystalline $UBe_{13-x}Al_x$ ($x = .11, .20$) lattice is contracted and the relationship between a_0 and x is still linear, indicating a systematic transfer of *Al* to the larger *BeI* site. We calculate that the *BeI* lattice site is $\sim 35\%$ larger than the *BeII* lattice site. This transfer to the larger *BeI* site explains both the smaller than expected *BJLT* lattice parameter and the contraction of the annealed polycrystalline $UBe_{13-x}Al_x$ lattice. The lattice of annealed $UBe_{12.89}Al_{.11}$ approaches *BJLT* dimensions. In addition, ΔC_{T_c} of the annealed $UBe_{12.89}Al_{.11}$ ground state is dramatically enhanced over ΔC_{T_c} of the unannealed, larger polycrystal. Via x-ray analysis no traces of secondary phases, interstitial *Al* pockets or non-uniform lattice strain were detected. An analysis of x-ray linewidth as determined by synchrotron diffraction clearly showed that the unannealed $UBe_{12.89}Al_{.11}$ peak FWHM was consistently ≥ 2.5 times larger than the peak FWHM of *BJLT* crystal 31. Thus it appears that, compared to unannealed $UBe_{12.89}Al_{.11}$, the *BJLT* lattice is able

to incorporate *Al* into the larger *BeI* lattice site during the slow crystal growth process so as to minimize any residual stress/strain which may be experienced by the unit cell. Once again we see that a change in a materials property, in this case the redistribution of *Al* and its effect on the size of the unit cell, is accompanied by a dramatic change in the superconducting ground state (ΔC_{T_c}). We now move on to magnetic properties.

The magnetic susceptibility of as-grown and melted *BJLT* UBe_{13} is comparable to, and within the scatter limits of, pure and *Al* doped UBe_{13} . Any magnetic correlations which might exist in pure UBe_{13} are neither enhanced nor suppressed (down to 1.8K) in the novel *BJLT* system. While performing these magnetic studies we did discover that annealing and/or chemical substitution of the UBe_{13} lattice promotes the formation of a ferromagnetic-like anomaly in $\chi_{d.c.}$ at 160K. We have addressed certain aspects of this feature in appendices A and B. The occurrence of this anomaly is in no way correlated with the novel superconducting properties of the *BJLT* ground state observed through specific heat measurements. We discuss those measurements next.

When compared to standard UBe_{13} we may characterize the *BJLT* ground state as one which possesses a T_c reduced by $\sim 20\%$ and a ΔC_{T_c} enhanced by as much as 50%. Since the superconducting entropy, $\gamma(0)$, and transition width for all *BJLT* transitions analyzed here are all equal to their respective standard values, we conclude that the *BJLT* peak is due to a single superconducting transition. Above T_c it is seen that the standard 2.5K anomaly in C is suppressed and shifted to lower temperatures, indicating that the local U environment is altered compared to standard UBe_{13} . Attempts to fit the suppressed high temperature *BJLT* anomaly

in C to a 3-term, two-level Schottky model were unsuccessful. The entropy removed from this anomaly is redistributed below 1K such that the total entropy from $0 \rightarrow 6K$ is unchanged (within our error bars) in going from standard to *BJLT* UBe_{13} .

Very low temperature specific heat measurements have revealed that as the temperature is reduced below $\sim 4K$ and approaches $.105K$ the *BJLT* specific heat shows no sign of a low temperature up-turn is proportional to $T^{2.4}$. That this relationship differs somewhat from that of standard UBe_{13} (T^3) and appears to be approaching the polycrystalline $UBe_{12.97}B_{.03}$ limit of T^2 suggests that there may be differences in the nodal structure between *BJLT* and standard UBe_{13} . However, the temperature reached here is quite possibly not low enough to rule out Fermi surface effects and additional electronic contributions to C in this range. Since *Al* is present in all *BJLT* crystals we have checked to see whether the *BJLT* ground state may be duplicated in polycrystalline $UBe_{13-x}Al_x$.

The superconducting transition of unannealed $UBe_{12.89}Al_{.11}$ is suppressed and shifted down in temperature, as we expect from similar doping studies in this system. However, once annealed, ΔC_{T_c} is enhanced by $\sim 300\%$ while T_c is unchanged. Thus a redistribution of *Al* is accompanied by a dramatic improvement in ΔC_{T_c} . Similarly, by arc-melting as-grown *BJLT* crystals 21 and 24 and causing a substantial *Al* redistribution in these systems (as seen in the dissipation of the large *Al* rich islands) we discover that ΔC_{T_c} is suppressed and becomes very (unannealed) polycrystalline-like.¹ There is a clear connection between the (re)distribution and placement of *Al* on the *BeI* lattice site and ΔC_{T_c} . High temperature specific

¹The similarity between T_c and ΔC_{T_c} for unannealed $UBe_{12.89}Al_{.11}$ and melted *BJLT* crystals 21 and 24 is also proof for the similarity of the *Al* content of these systems.

heat studies on the unannealed polycrystalline material indicate that the 2-level f -electron system is almost completely suppressed. The local f -electron environment is altered and as a result the amplitude of any f -electron correlations present may be diminished. This situation appears similar for the melted *BJLT* crystals 21 and 24, which also possess suppressed superconducting transitions. Once the polycrystalline material is annealed we observe the return of a fraction of the high temperature anomaly lost during arc-melting. The high temperature anomalies of annealed $UBe_{12.89}Al_{1.11}$ and the *BJLT* crystals possess similar properties (T_{max} and ΔC_{max}).

As we noted earlier, since $\gamma(0)$ is unaltered in going from the standard to the *BJLT* ground states, the enhancement of ΔC_{T_c} in these systems may be attributed solely to strong coupling effects. We have also probed the superconducting ground state and pairing mechanism of the *BJLT* crystals by measurements of the specific heat in magnetic field. The value of H'_{c_2} is essentially unchanged in going from standard to *BJLT* UBe_{13} . This is taken as evidence that both ground states are equally insensitive to applied magnetic fields. Also, since we know that $H'_{c_2} \propto m^*$, we may conclude that the quasi-particle effective mass is similar in both systems. This is also concluded from the equivalence of the values of the *BJLT* and standard $\gamma(0)$. We turn now to resistivity and magnetoresistance.

Resistivity data in 0 field obtained on *BJLT* crystal 31 indicate that this crystal possesses properties expected from an unannealed, slightly impure UBe_{13} sample. The 2.5K coherence peak is suppressed by roughly 80% and broadened by almost 30% compared to a pure single crystal, while the resistivity ratios for these systems are essentially equal. The temperature of the maximum is not reduced, unlike the

temperature of the corresponding maximum in the specific heat. When measured in magnetic field the relative magnetoresistance of the *BJLT* ground state displays the same unique scaling relationship obeyed in standard UBe_{13} . The form of this relationship and the parameters obtained have been used to argue against both the single impurity Kondo model and the Kondo lattice model descriptions of the ground state, and for the presence of ferromagnetic correlations.

6.2 Comparisons to *B* doped UBe_{13}

The very interesting specific heat data of $UBe_{12.97}B_{.03}$ was presented in section 2.2.3. We would now like to compare and contrast our results on *BJLT* UBe_{13} with those obtained for the *B* doped compound. We begin by considering the materials aspects of the *B* and *Al* doped UBe_{13} lattice. The atomic radii of B^{3+} (.98 *Angstroms*) is somewhat less than that of Be^{2+} (1.12 *Angstroms*), while the Al^{3+} radius (1.43 *Angstroms*) is substantially larger. From NMR studies on $UBe_{13-x}B_x$ ($0 \leq x \leq .067$) we know that the *B* resides exclusively on the larger cubic *BeI* lattice site [125]. Also, our *EPMA* and x-ray studies indicate that the *Al* impurity in both *Al* doped annealed polycrystalline as well as *BJLT* UBe_{13} preferentially occupies the *BeI* lattice site, although we have also seen that the *Al* distribution is rather non-uniform. No second phases have been observed in either the *B* or *Al* doped samples, indicating good solubility at the impurity levels of interest here. Thus once introduced into the lattice we would expect the smaller *B* impurity to induce a contraction of the lattice, and the larger *Al* impurity to expand the lattice. However, no change in the lattice parameter (a_0) has been observed in *B* doped UBe_{13} up to levels of 6.7% [94] (measured with respect to *U*), while only

1% *Al* produces a measurable expansion of .002 *Angstroms* [95]. It is interesting to consider previous doping experiments on $UBe_{13-x}M_x$ ($M=Ga, B, Al, Cu$) [94, 96]. Since both *Ga* (1.41 *Angstroms*) and *Cu* (1.28 *Angstroms*) are larger than *Be* they expand the unit cell once introduced on to the *Be* site(s). The unit cell is expanded by .008 *Angstroms* with the addition of 12% *Ga* (recall from table 5.5 that the addition of 11% *Al* resulted in an expansion of roughly .01 *Angstroms*) and by .005 *Angstroms* with only 6% *Cu*. Since the difference between the *Cu* and *Be* radii (with *Cu* being larger) is roughly equal to difference between the *B* and *Be* radii (with *B* being smaller), it is noteworthy that the substitution of 6% *Cu* has a measurable effect on the size of the unit cell whereas the substitution of 6% *B* apparently does not. It could be that the *B* occupies only the larger *BeI* site while larger *Cu* is dispersed between the *BeI* and smaller *BeII* lattice sites. Further examination of the data reveals that annealing has a pronounced effect on a_0 for the *Ga* and *Al* doped samples, while it has no effect on the *Cu* and *B* doped systems. After annealing for only 5 days at 950°C the 12% *Ga* doped lattice parameter was reduced by .009 *Angstroms*. This is similar to the reduction of the 11% *Al* a_0 by roughly .007 *Angstroms* (table 5.6). Thus as far as impurity induced structural effects are concerned, it appears that *Al* and *Ga* behave quite similarly (they expand the lattice and are extremely mobile) once introduced into the UBe_{13} lattice, whereas *B* is extremely stable and has a small effect on the size of the unit cell. Since all three elements (*Ga*, *Al*, *B*) are in the same column of the periodic table we expect them to possess similar chemical properties.

Chemically, since *Ga*, *Al*, *B* are all trivalent compared to bivalent *Be*, we would expect similar band filling effects from all three dopants, although at the levels of

interest here this effect should be $\leq 1\%$. Since the host compound, UBe_{13} , becomes superconducting at $T_c \sim .9K$, we may be able to view the chemical effects of the various impurities in terms of their effect on T_c . To that end we note that T_c values for 3% B doped polycrystals are fairly inconsistent [126, 127, 94, 128]. For a B level of 3% T_c has been reported to be as low as .77K and as high as .91K. Establishing a clear trend for T_c as a function of B concentration is difficult. A slight, non-monotonic variation of only 15% is observed in T_c for doping levels up to 6.7%. By the 10% level $T_c \leq .015K$. And, at the 10 and 20% levels annealing appears to have little effect on T_c for the B doped material. Sample quality and difficulty in controlling such small quantities of impurity are generally assumed to play key roles in the resulting T_c . Quite different behavior is observed for Al and Ga . A monotonic behavior of T_c as a function of impurity concentration has been observed in Al and Ga doped polycrystals, while annealing results in a marked increase in T_c for both systems [95, 114]. So it is clear from the chemical and physical evidence gathered to date that, compared to Al and Ga , B is quite unique in its effects on T_c and a_0 of UBe_{13} . Keeping these differences in mind we now compare the superconducting properties of the $BJLT$ and anomalous $UBe_{12.97}B_{.03}$ ground states.

In our comparison of the two superconducting ground states, we will concentrate on parameters obtained via the standard equal entropy data analysis technique. To aid in the comparison we have plotted the specific heat data for $BJLT$ crystal 19 and $UBe_{12.97}B_{.03}$ [94] in figure 6.1, and give the values of important parameters in table 6.1. Referring to figure 6.1, we observe that the B doped peak is substantially wider than the $BJLT$ peak. This is an indication of superior sam-

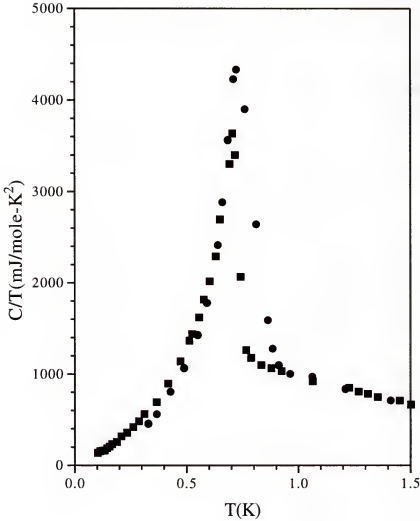


Figure 6.1: The specific heat divided by temperature vs. temperature for *BJLT* crystal 19 (squares) and polycrystalline $UBe_{12.97}B_{0.03}$ (circles). Compared to typical *BJLT* crystal 19, the *B*-doped polycrystal has a larger T_c (identical to the pure starting material used in that study) and a very broad transition. Because of this broad transition, the *B*-doped normal state entropy must be substantially increased below T_c to reach entropy balance at T_c . This results in a 15% larger $\gamma(0)$ in this material compared to the standard. We also note that from an equal entropy construction viewpoint, since the slopes of both curves below their peak maxima are equal, the much wider *B*-doped transition must result in a larger ΔC_{T_c} to accommodate the extra area under the curve.

Table 6.1: Specific heat parameters for $UBe_{12.97}B_{.03}$ and a “pure” polycrystal (made and measured during the same study [94]) and a comparison to *BJLT* 19 and standard 2A.

Sample Description	T_c (K)	ΔC_{T_c} $(\frac{mJ}{mole-K})$	$C/T(T_c)$ $(\frac{mJ}{mole-K^2})$	$\gamma(0)$ $(\frac{mJ}{mole-K^2})$	$\Delta C_{T_c}/(\gamma(0) \cdot T_c)$
$UBe_{12.97}B_{.03}$.79	4013	1120	1550	3.28
UBe_{13}	.82	1580	941	1350	1.43
<i>BJLT</i> 19	.73	2196	1157	985	3.05
2A	.91	1705	852	1031	1.83
Standard SC					

ple quality for the *singlecrystalline BJLT* sample. Note that all *BJLT* results are on as-grown single crystals, and that all *B* data correspond to polycrystalline samples. However, as we have shown, we may approach the *BJLT* ground state in polycrystalline $UBe_{12.89}Al_{.11}$ by annealing according to the single crystalline growth protocol. Thus some of the effects of annealing on the superconducting transition of $UBe_{12.89}Al_{.11}$ already seem to be incorporated into the unannealed $UBe_{12.97}B_{.03}$ ground state. The very broad nature of the *B*-doped transition also plays a role in the large ΔC_{T_c} calculated for this sample. Notice that the slopes of the data for the *B*-doped and *BJLT* samples in figure 6.1 below the peaks in C/T are equal. This means that, when performing an equal entropy construction, the superconducting data below the peak in C/T for the *B*-doped sample must be extrapolated to much higher temperatures (and therefore much larger values of C/T) than *BJLT* 19 in order to account for the extra area under the peak.

From table 6.1 we notice the difference in the T_c 's between the two data sets. This topic has already been discussed above. Notice that T_c for the pure UBe_{13} sample used for the B doping study is only .82K. This value is reduced compared to that of nominally pure UBe_{13} . The point to make here is that the reduced T_c of the B doped polycrystal is essentially equal to T_c for the pure sample used in the same study. There is no difference between the two T_c 's. Clearly there is a difference ($\sim 20\%$) between the pure (crystal 2A) and $BJLT$ T_c 's presented in this work. Thus a 20% reduction in T_c from the standard value is a property we may associate with the $BJLT$ single crystals only. The depressed values of T_c observed in the B doping study (for the pure and doped material) are probably a sign of poor sample quality. Next, it is clear that the value of $C/T(T_c)$ is enhanced for the $BJLT$ and B doped samples. This effect has been associated (section 5.4) with the suppression and shifting to lower temperatures of the high temperature anomaly in C . By calculating the superconducting and normal state entropy at T_c for both samples we observe that both novel ground states possess a negative entropy balance. However, by adjusting the normal state C/T below T_c to ensure proper entropy balance at T_c it becomes clear that $\gamma(0)$ for the B doped material is substantially enhanced ($\sim 15\%$) over that of the reference material from the same study. This is an important difference between polycrystalline $UBe_{12.97}B_{.03}$ and $BJLT$ single crystals. The density of states for the Al "doped" $BJLT$ single crystals is not enhanced. Therefore the enhancement of ΔC_{T_c} may be attributed solely to increased strong coupling effects in these crystals. In general it has been discovered that ΔC_{T_c} for the entire B doped polycrystalline system rises quickly, reaches a maximum around the $B_{.03}$ level, and then falls off rapidly [94]. For polycrys-

talline Al doped UBe_{13} we observe that ΔC_{T_c} is strictly a decreasing function of Al concentration [114]. Very low temperature specific heat measurements on $BJLT$ 19 and $UBe_{12.97}B_{.03}$ show deviations from the $C \propto T^3$ relationship verified in pure UBe_{13} , indicating possible changes in the gap symmetry and/or nodal structure. Finally we note that the $UBe_{12.97}B_{.03}$ sample investigated was also subjected to μSR studies, and no quasi-static magnetic correlations were observed below 1K.

The comparison of $BJLT$ UBe_{13} and polycrystalline $UBe_{12.97}B_{.03}$ has shown that from a materials and thermal property point of view these systems are quite different. A clear trend of T_c with B concentration is difficult to observe, and as we have seen the anomalous ground state of $UBe_{12.97}B_{.03}$ may be observed in samples which possess a T_c identical to that of the pure starting material. The variation of ΔC_{T_c} for B doped UBe_{13} is non-monotonic, and by only the 10% impurity level superconductivity is completely suppressed down to .015K. On the other hand the suppression of ΔC_{T_c} for Al doped UBe_{13} is monotonic, and superconductivity remains at least up to the 40% Al level. We have also seen that the density of states for $BJLT$ -like $UBe_{12.97}B_{.03}$ is markedly enhanced compared to the standard value. The density of states for our single crystalline $BJLT$ samples is not enhanced over the standard value.

When we consider the size of the crystalline lattice there appears to be little to no change in the lattice parameter up to at least the 7% doping level in the B doped material. Though Al is much larger than either B or Be , expansion of the lattice is seen even at the 1% Al impurity level. Once introduced into the lattice B has been found to reside strictly on the BeI lattice site. Our data suggests that the Al in single crystalline $BJLT$ and annealed polycrystalline UBe_{13} also resides

predominantly on the *BeI* site. Through annealing and its effect on the lattice parameter and the redistribution of the *Al* impurity it is clear that *B* is much more stable in the UBe_{13} lattice than *Al*.

Finally, we stress the point that the novel *BJLT* properties observed to date have been seen in *singlecrystalline Al* "doped" UBe_{13} and *polycrystalline B* doped UBe_{13} . The *BJLT* ground state is also approached in annealed polycrystalline $UBe_{12.89}Al_{.11}$. This is an important observation. The single crystalline *BJLT* samples, and to only a slightly lesser degree the 3% *B* doped polycrystals, most probably represent crystal systems which are able to take maximum advantage of their respective impurities introduced during fabrication and achieve this by incorporating those impurities on to the *BeI* lattice site. The slower single crystalline growth period appears to be necessary to allow the UBe_{13} lattice to accommodate the large *Al* impurity as the single crystals form out of the melt, whereas the relatively rapid arc-melting process provides sufficient time to allow the smaller *B* impurity to be incorporated into the most energetically favorable lattice position. The arc-melting process does not provide sufficient time and energy for the $UBe_{13-x}Al_x$ lattice to take maximum advantage of the large *Al* impurity, and so the resulting superconducting transition is suppressed. However, $UBe_{12.89}Al_{.11}$ is nearly *BJLT*-like, and annealing according to single crystalline growth specifications is sufficient to allow the *Al* to redistribute to the *BeI* site and for the system to reach a highly enhanced superconducting state. Thus the data presented to date for all samples, when taken together, suggest that impurity induced structural changes and impurity site occupation, controlled by variables associated with the crystal (poly or single) growth process, can not be underes-

timated in their potential to dramatically alter the underlying superconducting ground state in UBe_{13} . Now we would like to try to understand these results on a phenomenological level.

6.3 Impurities and UBe_{13}

Whether introduced into the U or Be lattice sites, all substitutional impurities have a pronounced effect on the superconducting properties of UBe_{13} . With the possible exception of B , all impurities cause T_c and ΔC_{T_c} to be rapidly suppressed. This type of behavior is common to all HFS, and applies to magnetic as well as non-magnetic impurities. If the impurity spin-conduction electron hybridization is strong, the impurity moment is naturally very short lived compared to thermal fluctuation lifetimes, and there is little possibility for a spin-spin exchange interaction to develop between the impurity spin and the conduction electrons [129]. Put another way, we can say that the very rapid impurity spin fluctuations result in an impurity spin fluctuation temperature which is much larger than T_c . An impurity moment does not develop and the impurity is described as non-magnetic. In a traditional BCS s -wave superconductor, as we have mentioned, non-magnetic impurities have no effect on T_c once introduced into the lattice [42]. However, if an impurity moment does develop due to a weak impurity spin-conduction electron hybridization, then through a spin-spin exchange interaction the impurity acts to break up the spin singlet Cooper pairs and T_c is reduced [100, 130]. As we have seen, the reduction of T_c in UBe_{13} due to the addition of non-magnetic Al , as well as Y , is large (20% for the $BJLT$ crystals) and certainly not expected in an s -wave

superconductor [97, 98]. In order to address this behavior we must consider the effects of the impurity on the orbital part of the superconducting wave function.

6.4 Symmetry and *f*-electron Correlations

It has long been known that impurities have a measureable effect on T_c when introduced into anisotropic superconductor [131]. Impurities (magnetic or non-magnetic) act to round off the density of states and reduce the order parameter. The Cooper pairs are then less able to take advantage of the new state and T_c falls. When the doped UBe_{13} specific heat data are viewed in this light, the rapid suppression of T_c and ΔC_{T_c} are taken as evidence for a highly anisotropic superconducting ground state. While comparisons to 3He and the extreme insensitivity of T_c to applied magnetic fields have been used as evidence to support a *p*-wave state [132], other experiments have claimed to reveal a *d*-wave character [108, 133, 134]. Most theoretical approaches to UBe_{13} today assume a *d*-wave symmetry, and that is the approach we shall also take.

Although an exact theoretical value of ΔC_{T_c} for *d*-wave superconductors is somewhat model dependent, a weak coupling value of .67 has been put forth [135]. We notice from table 5.9 that the value for our standard crystal 2A is 1.83. This is obviously highly enhanced, even with respect to the *s*-wave value of 1.43. Thus as we have discussed, pure UBe_{13} possesses a ΔC_{T_c} which falls outside of the realm of standard weak coupling *BCS* theory. This is taken as direct evidence for the presence of strong coupling, which acts to enhance ΔC_{T_c} as well as the energy gap at $T=0$ ($\Delta(0)$) [136]. In fact T_c in such a system is smaller than expected based on the weak coupling value of $\Delta(0)$. Strong coupling effects arise when the entire

electron-phonon interaction is treated in detail without making the weak coupling assumption that the interaction parameter (V) is isotropic and constant for all electrons within the lattice energy of the Fermi surface [39]. Thus in UBe_{13} we are working with a highly anisotropic, strong-coupled heavy Fermion superconductor. Let us now try to understand the effects of Al and the $BJLT$ superconducting ground state.

The effect of Al on T_c and ΔC_{T_c} in unannealed polycrystalline $UBe_{13-x}Al_x$ is typical. Both quantities are rapidly suppressed as the anisotropic ground state is smoothed out. After the system is annealed and the Al impurity is redistributed to the BeI lattice site, T_c remains the same while ΔC_{T_c} is greatly enhanced. Clearly the lack of a change in T_c from the unannealed to the annealed state indicates that the annealed and unannealed anisotropic order parameters are altered by the Al in similar ways. One possible explanation for the jump in ΔC_{T_c} is that the order parameter of pure UBe_{13} is predominantly s -wave, but contains enough anisotropic d -wave character to produce the power law relationships characteristic of a system with nodes. As the order parameter becomes more isotropic due to Al doping, ΔC_{T_c} approaches its strong-coupled-enhanced pure s -wave isotropic value. Precisely how the redistribution of Al between Be lattice sites promotes this effect (for any model we discuss) is an open question. However, this particular scenario would require that the UBe_{13} ground state have a large s -wave component. As we have said, most studies indicate that the ground state is in fact d -wave. So to understand our annealed $UBe_{12.89}Al_{.11}$ and $BJLT$ specific heat data we need to include one more factor into our phenomenological approach, and that is f -electron correlations.

Magnetic correlations have long been associated with HFS [137, 123, 138]. These correlations, which are commonly referred to as dynamic spin fluctuations, are simply f -electron correlations localized in momentum space, as opposed to (static) long range magnetic order which is localized in real space. Antiferromagnetic spin fluctuation mediated Cooper pairing has been proposed to explain the unusual properties of HFS [139, 140, 134, 141, 142]. Working in the strong coupling formalism, we write the total free energy in the superconducting state as [143]

$$F = F_n + A(T) \cdot |\Delta|^2 + B \cdot |\Delta|^4 \quad (6.1)$$

where $A(T) = N(0)(T - T_c)/T_c$, Δ is the superconducting order parameter, $N(0)$ is the density of states at the Fermi level, F_n is the normal state free energy, and $B(T) = .0533N(0)/(K_B T_c)^2$. For $T < T_c$ we want to minimize F with respect to Δ . This is easily done. Plugging Δ back into our equation for the free energy we arrive at an expression for the free energy difference between the superconducting and normal states for $T < T_c$:

$$F_{sc} - F_n = -A(T)^2/B \quad (6.2)$$

The specific heat jump at T_c is now simply related to the second derivative of ΔF with respect to T . We get for the final result:

$$\Delta C_{T_c} = 1/(B \cdot T_c) \quad (6.3)$$

Thus clearly as the factor B is reduced, ΔC_{T_c} is enhanced. It is important to note that this simple analysis also yields an expression for the order parameter (and hence the energy gap) as a function of temperature, and it may be written as

$$\Delta(T)^2 \propto \frac{1 - T/T_c}{2B} \quad (6.4)$$

Thus by comparing equations 6.3 and 6.4 we see that as $T \rightarrow T_c$, ΔC_{T_c} is proportional to the slope of the square of the energy gap. Once again we stress that precisely how the parameter B is reduced in the context of a redistribution of Al among the Be lattice sites is not clear.

By carrying out a much more detailed analysis of the free energy difference of equation 6.2, it has been shown that ΔC_{T_c} can be expressed in terms of the strong coupling parameter T_c/ω_0 [144, 145]. The frequency ω_0 characterizes the energy of the pair mediating bosonic excitation. For HFS it is believed that these bosons may be dynamic antiferromagnetic f -electron correlations. It has been shown for d -wave superconductors that there is a critical frequency, ω_c , below which the correlations are pair breaking, while for $\omega_0 > \omega_c$, T_c is actually enhanced [140]. Thus there is a region around ω_c in which a balance is reached and T_c is unchanged. Investigations of the low frequency modes have revealed that in this limit ΔC_{T_c} is enhanced for d -wave superconductors mediated by antiferromagnetic f -electron correlations [145, 146]. When we alter the spectral function which characterizes these correlations (through Al or B doping for example) and reduce ω_0 , ΔC_{T_c} is enhanced. We may now address the results presented in this work.

First, the reduction in T_c for all samples is due simply to the presence of *Al* and its effects on the anisotropic superconducting order parameter. For the unannealed *Al* doped polycrystals ΔC_{T_c} is also reduced significantly, as the models predict. We observe that for these unannealed samples the high temperature specific heat anomaly is almost completely suppressed down to 1K. Thus the local U environment is altered to the point where the 2-level U system is almost non-existent and the amplitude of the dynamic intersite U f -electron correlations is significantly reduced. Once the *Al* polycrystals are annealed and a majority of the *Al* migrates to the larger *BeI* lattice site, the local U environment becomes more single crystalline-like, a portion of the entropy lost below T_c during arc-melting returns, and the amplitude of the low frequency dynamic f -electron correlations is increased, although the frequency is less than that in standard UBe_{13} , and ΔC_{T_c} is markedly enhanced while T_c is unchanged. Clearly from equation 6.4 we see that the slope of $\Delta(T)^2$ as $T \rightarrow T_c$ is enhanced in the *BJLT* ground state compared to standard UBe_{13} . As the value of $\Delta(0)$ involves the summation over all energies of the spin fluctuation spectrum, we would not expect that adding low energy spectral weight to the system would significantly alter $\Delta(0)$. We associate the re-emergence of the low frequency f -electron correlations with the observed increase in ΔC_{T_c} . In this sense the evolution of ΔC_{T_c} in $UBe_{13-x}Al_x$ from the unannealed to the annealed state is similar to the evolution of ΔC_{T_c} in going from pure UBe_{13} to $UBe_{12.97}B_{0.03}$. The only difference between the two systems appears to be that *Al* acts to reduce T_c much more effectively than does *B*. The data for the *BJLT* single crystals simply reflects the fact that the slow crystal growth process results in a majority of the *Al* impurity occupying the *BeI* lattice site. Thus the *BJLT*

crystals enter the enhanced superconducting state immediately. When we melt the *BJLT* crystals and redistribute the *Al*, ΔC_{T_c} is reduced. As in the case of the polycrystalline samples, the high temperature anomaly in C is almost completely suppressed and the amplitude of the low frequency intersite f -electron correlations is significantly reduced.

What we have learned here is that by considering both pair breaking and dynamic spin fluctuations in the HFS UBe_{13} , we may better understand the novel *BJLT* ground state. Clearly the problem of preferential *BeI* site occupation by the *Al* impurity, and its effect on the superconducting properties of this compound require further study. We note that theoretical studies into the electronic structure of the UBe_{13} ground state have revealed that the *BeII* atomic site volume contains .15 electron less charge than the *BeI* volume, indicating that the *BeII* atoms are bonded more strongly than the *BeI* atoms [147]. Crystallographic data tell us that the *BeI-BeII* distance is essentially equal to the *BeII-BeII* distance in UBe_{13} . So the difference in the *BeI-BeII* site charge is thought to be due to increased *BeII-U* bonding and hybridization. Though the hybridization has been shown to be rather small [148, 149, 150], it has been discovered that small changes in the *Be-U* hybridization result in measureable changes in $\gamma(0)$ for this system [79]. If a majority of the *BeII* lattice sites are occupied by *Al*, then the *U-Al* hybridization may be associated with the demise of the 2-level system at 2.5K, the alteration of the local U environment and a reduction of the intersite $U-U$ f -electron correlations, resulting in a suppressed ΔC_{T_c} . These detrimental effects would be alleviated by a transfer of a majority of the *Al* to the more weakly hybridized *BeI* lattice site. Relating *Be* site occupation, structural differences, and how they alter the *Be-U*

(and $Al-U$) hybridization and the f -electron correlation spectral density will surely be a challenge.

6.5 Future Work

There are a number of experiments we may perform to learn more about this interesting superconducting system. First, as we pointed out previously, while B stands alone in its effects on T_c and the lattice parameter of UBe_{13} , it lies in the same column ($IIIB$) of the periodic table as Al , Ga , In , and Tl . It has also been shown that Ga behaves very much like Al in its effect on these parameters. Thus arc-melting and *annealing* polycrystalline Ga doped UBe_{13} might possibly result similar novel properties observed here. As the atomic radius of Ga (1.41 *Angstroms*) is essentially equal to that of Al we would expect a similar concentration of Ga (roughly 11%) would be necessary to induce *BJLT*-like results in the specific heat. By establishing a trend for the $IIIB$ elements we may conclude that the single p -electron donated by these elements is responsible for increased f -moment screening, which then would obviously alter the f -electron correlation spectral density, and ultimately ΔC_{T_c} .

NMR measurements on Al doped polycrystalline $UBe_{12.89}Al_{.11}$ would help to determine the percent change in Be lattice site occupancy of the Al in going from the unannealed to the annealed state. Precisely how much Al must reside on the larger BeI lattice in order to induce the *BJLT*-like ground state? By measuring *NMR* resonances for 9Be and ^{27}Al nuclei and analyzing the resultant field-swept spectra in terms of the known quadrupolar interaction parameters for UBe_{13} we may determine whether the Al is located predominantly on the cubic BeI site.

Since preferential BeI site occupation by the Al obviously has an effect on the lattice parameter for these novel $BJLT$ systems, we would like to know what other structural anomalies are induced by this occupation. Neutron diffraction studies may prove very useful in elucidating fine structural differences between standard and $BJLT\ UBe_{13}$. Any changes in the $BeII-U$ and $BeII-BeI$ distances may be measured from sample to sample. As these distances are directly related to bonding and hybridization among the various atoms, a correlation may develop between interatomic distance and ΔC_{T_c} in this system.

APPENDIX A

$\chi_{D.C.}$ ANOMALY I

The results presented in figure 5.18 are very interesting. As we have seen, the anomaly located at 160K in $\chi_{d.c.}$ is certainly not a necessary condition for the formation of either the *BJLT* or the standard UBe_{13} ground states. This appears to be a separate entity which deserves careful study. We have initiated such a study and present some preliminary findings here. In appendix A we concentrate on magnetic susceptibility results. In appendix B we present some preliminary findings from x-ray diffraction and resistivity studies of this novel feature.

A.1 Magnetic Susceptibility

The anomaly observed in $\chi_{d.c.}$ for annealed *BJLT* crystal 30 has an onset temperature (T_0) of 160K. *EPMA* and low temperature specific heat results (sections 5.1 and 5.4) indicate that annealing has caused the *Al* impurity to migrate completely out of the lattice. Thus the data may be taken to be those of a pure, annealed, single crystal of UBe_{13} . We would like to know whether this anomaly may be observed in non-annealed pure or doped UBe_{13} samples, and whether it is purely a single crystalline effect. We address these questions by first noting that a similar feature has already been observed in $U_xTh_{1-x}Be_{13}$ ($.48 < x < 1$) and in an annealed single crystal of pure UBe_{13} [151, 152]. Is this anomaly present in unannealed pure UBe_{13} , or in UBe_{13} doped on the *Be* site? To further the study of this

novel transition we have prepared and measured (in the low field limit of $H=100\text{G}$) a total of 7 high purity polycrystals both annealed and unannealed, 15 doped polycrystals of $UBe_{13-x}M_x$ ($M = Ga, Ni, Cu, Pd, Al$) also annealed and unannealed, and 11 pure single crystalline samples. We begin with the single crystalline data.

Table A.1: A listing of 10 pure annealed and unannealed UBe_{13} single crystals indicating which crystals developed the 160K anomaly in $\chi_{d.c.}$.

Sample	Annealing	160K anomaly (?)
1A	1750 hours/ 1400°C	Yes
11A	1750 hours/ 1400°C	Yes
3A	1750 hours/ 1400°C	Yes
4A	1750 hours/ 1400°C	Yes
5A	1750 hours/ 1400°C	Yes
10A	1750 hours/ 1400°C	Yes
10M	None	No
Melted		
13A	1200 hours/ 1400°C	Yes
13	None	No
2A	6 months/ 1000°C	No

The single crystals studied here are listed in table A.1. All crystals were grown via the standard *Al*-flux growth technique. No traces of *Al* were detected in these crystals via *EPMA* analysis. We note that a portion of crystal 13A was powdered and compressed into a pellet prior to the data gathering, so the data for this sample (figure A.7) are of a compressed powder. The powdering was done to facilitate the x-ray studies which will be presented in appendix B. Thus while cold working apparently does not destroy the anomaly in 13A, melting does appear to destroy it in crystal 10A (10M). What is apparent from table A-1 is that only those crystals

which were annealed for at least 1200 hours at 1400°C posses an anomaly in χ_{dc} . The data for these crystals are presented in figures A.1-A.7.

Since melting a single crystal essentially creates a polycrystal, we have also investigated 7 high purity unannealed and annealed polycrystalline samples. The data for the pure polycrystals are given in table A.2. Once again we see that,

Table A.2: A listing of 13 high purity unannealed and annealed UBe_{13} polycrystals indicating which polycrystals developed the 160K anomaly.

Sample	Annealing	160K anomaly (?)
3P	None	No
3PA	336 hours/ 1400°C	No
6P	None	No
6PA	600 hours/ 1200°C	No
7P	None	No
7PA	600 hours/ 1200°C	No
9P	None	No
9PA	600 hours/ 1200°C	No
10P	None	No
10PA	1900 hours/ 1400°C	Yes
11P	None	No
12P	None	No
12PA	1900 hours/ 1400°C	Yes

as in the single crystalline case, long term high temperature annealing appears to be the key factor for the formation of the 160K anomaly. We plot the data for samples 10P, 10PA, 12P, and 12PA in figures A.8-A.9.

Annealing affects changes in lattice size and atomic position. The same is true for doping with substitutional impurities. It has been shown that substituting *Th* onto the *U* site promotes formation of the 160K anomaly. We have therefore

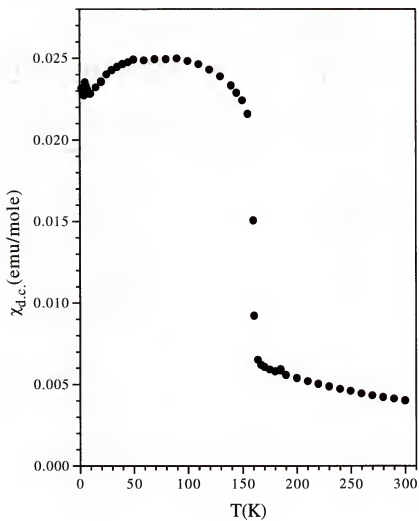


Figure A.1: The magnetic susceptibility vs. temperature in an applied field of $H=100\text{G}$ for standard UBe_{13} crystal 1A. This crystal was annealed for 1750 hours at 1400°C .

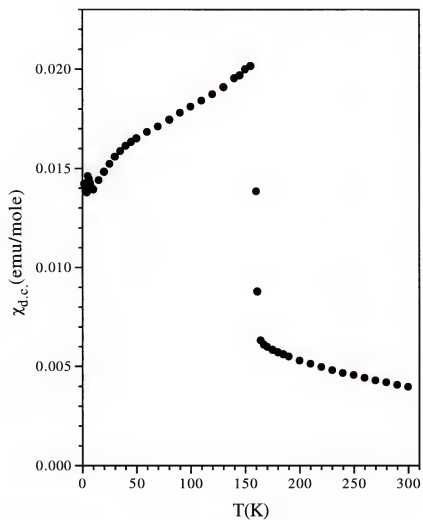


Figure A.2: The magnetic susceptibility vs. temperature in an applied field of $H=100G$ for standard UBe_{13} crystal 11A. This crystal was annealed for 1750 hours at $1400^{\circ}C$.

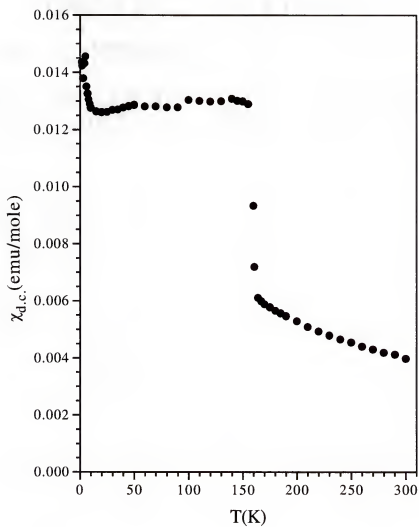


Figure A.3: The magnetic susceptibility vs. temperature in an applied field of $H=100\text{G}$ for standard UBe_{13} crystal 3A. This crystal was annealed for 1750 hours at 1400°C .

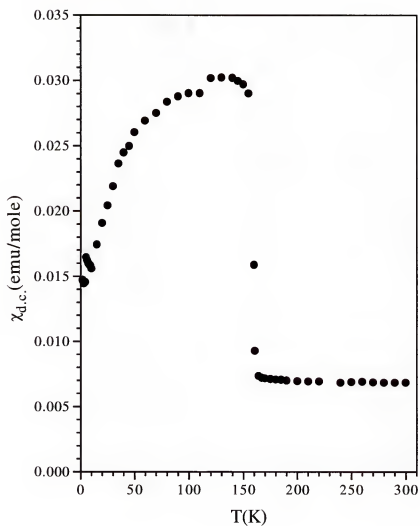


Figure A.4: The magnetic susceptibility vs. temperature in an applied field of $H=100\text{G}$ for standard UBe_{13} crystal 4A. This crystal was annealed for 1750 hours at 1400°C .

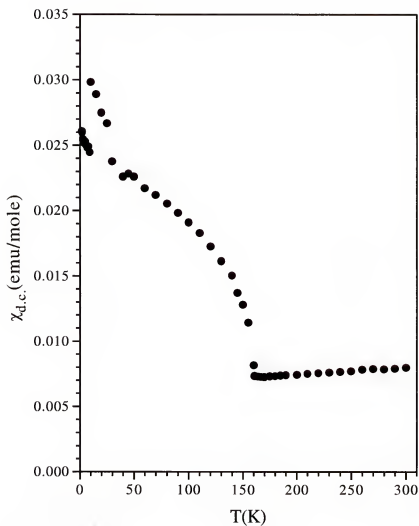


Figure A.5: The magnetic susceptibility vs. temperature in an applied field of $H=100\text{G}$ for standard UBe_{13} crystal 5A. This crystal was annealed for 1750 hours at 1400°C .

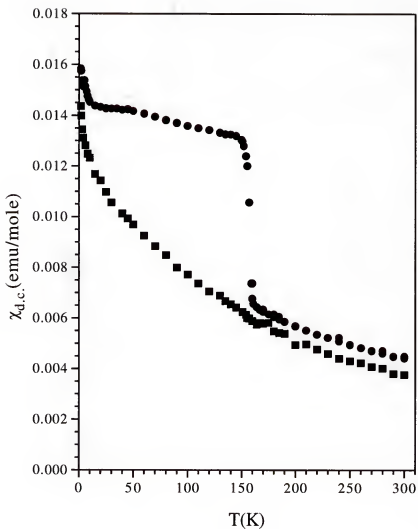


Figure A.6: The magnetic susceptibility vs. temperature in an applied field of $H=100\text{G}$ for standard UBe_{13} crystal 10A both annealed (circles) and melted (squares). This crystal was annealed for 1750 hours at 1400°C .

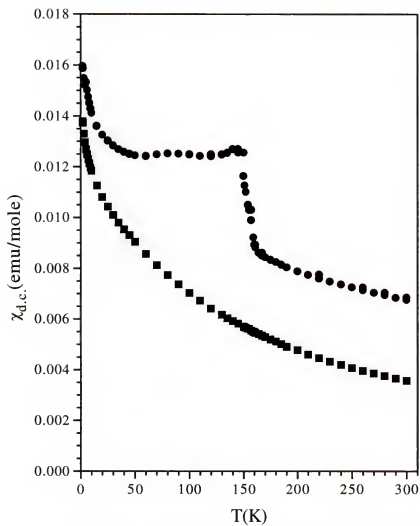


Figure A.7: The magnetic susceptibility vs. temperature in an applied field of $H=100\text{G}$ for standard UBe_{13} crystal 13 and 13A unannealed (squares) and annealed (circles). This crystal was annealed for 1200 hours at 1400°C . Note also that the annealed data represent those of a compressed pellet of the original crystal.

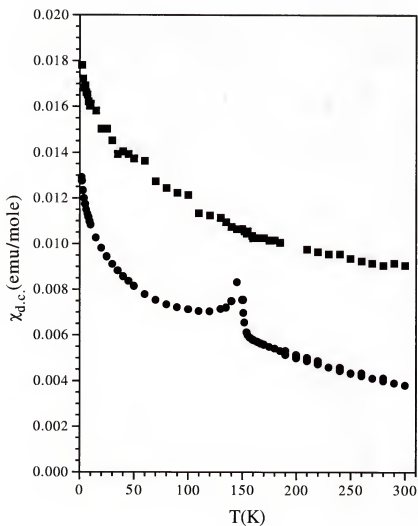


Figure A.8: The magnetic susceptibility vs. temperature in an applied field of $H=100\text{G}$ for unannealed (squares) and annealed (circles) high purity UBe_{13} polycrystal 10P. This sample was annealed for 1900 hours at 1400°C . The scatter in the unannealed data is due to a low signal to noise ratio present for the small quantity of sample measured.

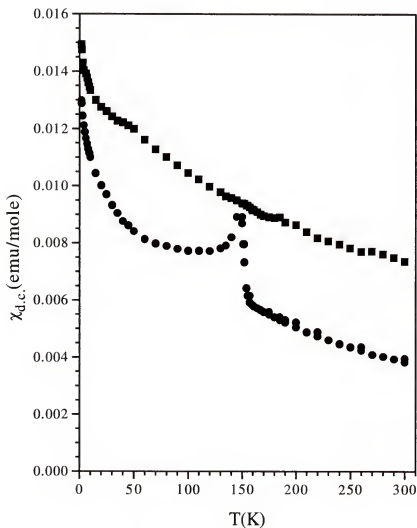


Figure A.9: The magnetic susceptibility vs. temperature in an applied field of $H=100\text{G}$ for unannealed (squares) and annealed (circles) high purity UBe_{13} polycrystal 12P. This sample was annealed for 1900 hours at 1400°C . The scatter in the unannealed data is due to a low signal to noise ratio present for the small quantity of sample measured.

substituted additional elements onto the *Be* site(s) of UBe_{13} in an effort to further characterize this novel effect. Results are presented in table A.3 and the data are shown in figures A.10-A.16.

Table A.3: A listing of 16 doped UBe_{13} polycrystals.

$UBe_{13-x}M_x$ (M_x)	Annealing	160K anomaly (?)
$Ga_{.03}$	None	Yes
$Ga_{.08}$	None	No
$Ni_{.01}$	1 month/ 1050°C	No
$Ni_{.015}$	None	No
$Ni_{.10}$	None	No
$Cu_{.01}$	None	No
$Cu_{.03} - 1$	None	Yes
$Cu_{.03} - 2$	None	Yes
$Cu_{.06}$	None	Yes
$Pd_{.01}$	None	Yes
$Al_{.08}$	None	Yes
$Al_{.08}A$	800 hours/ 1400°C	Yes
$Al_{.11}$	None	No
$Al_{.11}A$	5 hours/ 1400°C	Yes
$Al_{.20}$	None	No
$Al_{.20}A$	5 hours/ 1400°C	No

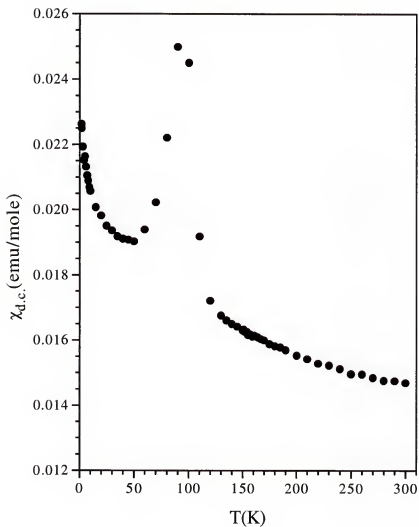


Figure A.10: The magnetic susceptibility vs. temperature in an applied field of $H=100\text{G}$ for unannealed $UBe_{12.97}Ga_{0.03}$. The strange anomaly seen here with an onset temperature of 130K has never before been observed in pure or doped UBe_{13} .

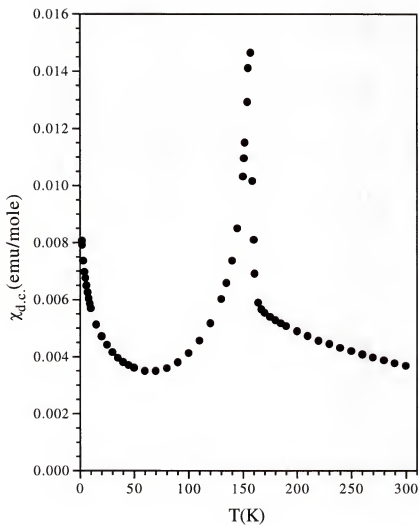


Figure A.11: The magnetic susceptibility vs. temperature in an applied field of $H=100G$ for unannealed $UBe_{12.97}Cu_{0.03}$ - sample 1. The strange anomaly seen here is similar to that observed previously in $UBe_{12.97}Ga_{0.03}$. However the onset temperature of the Cu doped anomaly is 160K and thus more like the other anomalous transitions presented in this section.

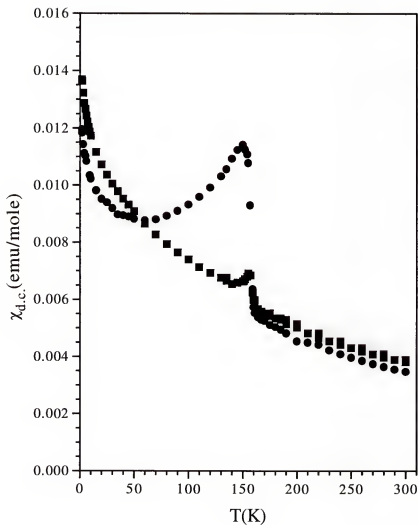


Figure A.12: The magnetic susceptibility vs. temperature in an applied field of $H=100\text{G}$ for unannealed (squares) and annealed (circles) $\text{UBe}_{12.92}\text{Al}_{0.08}$. Note here that the anomaly already exists in the unannealed material and appears to be enhanced by annealing. This sample was annealed for 800 hours at 1400°C .

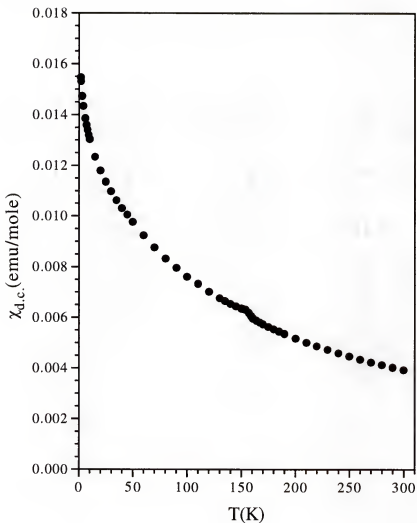


Figure A.13: The magnetic susceptibility vs. temperature in an applied field of $H=100\text{G}$ for unannealed $\text{UBe}_{12.97}\text{Cu}_{0.03}$ - *sample2*. The anomaly witnessed here is almost completely suppressed in 100G and appears to be more step-like than that seen in $\text{UBe}_{12.97}\text{Cu}_{0.03}$ - *sample*. The radical difference between the anomalies in the two $\text{Cu}_{0.03}$ doped polycrystals suggests that the cause of this novel feature in some UBe_{13} samples is not based purely on stoichiometry.

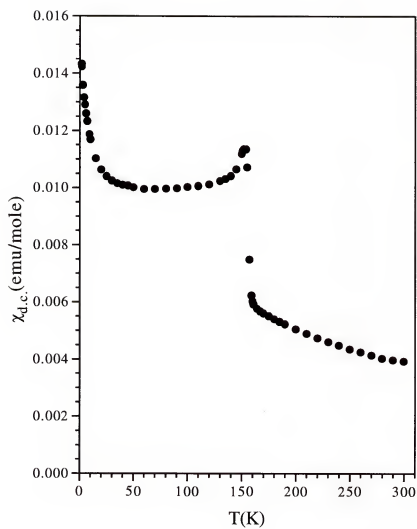


Figure A.14: The magnetic susceptibility vs. temperature in an applied field of $H=100\text{G}$ for unannealed $\text{UBe}_{12.94}\text{Cu}_{0.06}$.

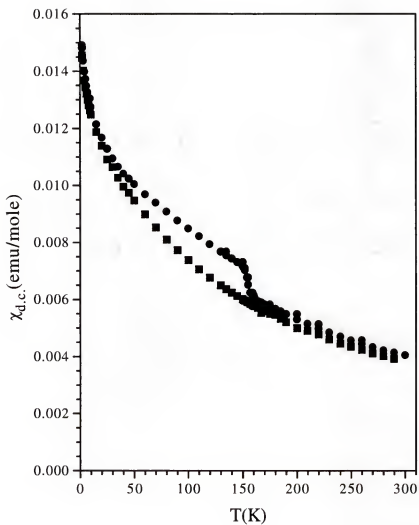


Figure A.15: The magnetic susceptibility vs. temperature in an applied field of $H=100G$ for unannealed (squares) and annealed (circles) $UBe_{12.89}Al_{11}$. Note here that the anomaly does not exist in the unannealed material and is produced via annealing. This sample was annealed for only 5 hours at $1400^{\circ}C$.

It is clear from these data that the substitution of impurities onto the Be lattice sites of UBe_{13} is capable of producing the same anomalous transition in $\chi_{d.c.}$ as seen in pure, annealed UBe_{13} and in Th doped UBe_{13} . Annealing does not appear to be the deciding factor in these samples. Moreover, the data in figures A.10 ($UBe_{12.97}Ga_{.03}$) and A.11 ($UBe_{12.97}Cu_{.03} - 1$, sample 1) are unlike any seen to date. The radical difference between the transitions in $UBe_{12.97}Cu_{.03} - 1$ and $UBe_{12.97}Cu_{.03} - 2$, as well as the appearance of the anomaly in $UBe_{12.89}Al_{.11}$ only after annealing suggest that stoichiometry is also not the sole factor for promotion of the anomaly.

We have seen that alteration of the crystalline lattice via annealing and/or chemical substitution is key to the creation of the 160K anomaly in $\chi_{d.c.}$. What may learn of the anomaly itself? Since it appears to be ferromagnetic-like in nature we would expect that measuring $\chi_{d.c.}$ versus temperature as a function of applied field would result in a variation of the onset temperature, or critical temperature, with field, due to the alteration of the local effective field experienced by the electronic spins. However, no temperature dependence has been observed over a range of fields of roughly two orders of magnitude. The data for single crystal 11A are presented in figure A.17. What we do observe is that the size of the anomaly is certainly a function of applied field and is almost completely suppressed by 4000G. What this means is unclear. Interestingly, the magnetization of this same crystal shows hysteresis in field, with a coercive field of $\sim 500G$.

Thus the magnetic susceptibility results presented here paint an interesting picture of this novel transition in UBe_{13} . We have seen that it may be induced via long-term high temperature annealing of pure single or polycrystalline samples, by

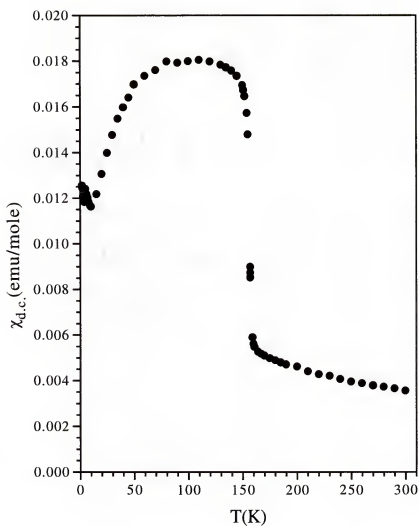


Figure A.16: The magnetic susceptibility vs. temperature in an applied field of $H=100\text{G}$ for unannealed $UBe_{12.99}Pd_{01}$.

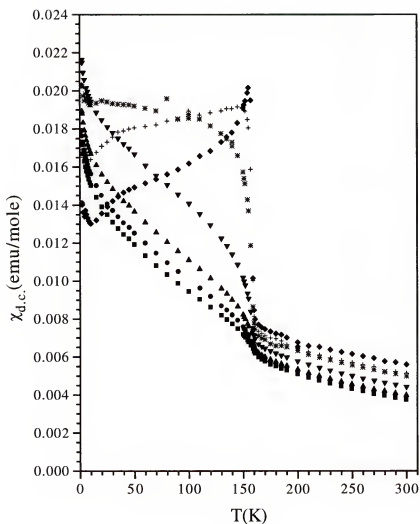


Figure A.17: The magnetic susceptibility vs. temperature as a function of applied field (H) for UBe_{13} crystal 11A. Although the magnetization of this sample shows hysteresis in applied field at $T=1.8K$, the data from this figure give no indication for a field dependent onset (or critical) temperature. The susceptibility was measured in 50 (diamonds), 125 (crosses), 300 (stars), 1000 (downtriangles), 2000 (uptriangles), 3000 (circles), and 4000G (squares).

chemical substitution, and by short term annealing of chemically substituted samples. Although ferromagnetic-like in appearance, the critical temperature of the anomaly has no detectable field dependence over almost two orders of magnitude, yet the magnetization of samples which possess the anomaly does show hysteresis in field. The size of the anomaly, however, is field dependent. And finally, we have produced two samples, $UBe_{12.97}Ga_{.03}$ and $UBe_{12.97}Cu_{.03} - 1$, which possess a transition unlike any ever seen in doped or pure UBe_{13} . The relationship between this transition and the 160K anomaly is, as yet, unknown. So, the magnetic nature of the novel feature is unclear. Therefore we have initiated transport property and x-ray diffraction studies to search for the presence of structural anomalies which may be associated with the transition at 160K. Some preliminary results are presented in Appendix B.

APPENDIX B

$\chi_{d.c.}$ ANOMALY II

In this appendix we first present our preliminary x-ray diffraction results on an annealed single crystal of UBe_{13} (sample 13A). The sample was pulverized into a fine powder and placed between two layers of clear tape. The total volume occupied was approximately $5\text{ mm} \times 10\text{ mm} \times 1\text{ mm}$. It has already been shown that cold working (powdering) does not destroy the 160K anomaly in $\chi_{d.c.}$. The powder was subjected to synchrotron radiation with a wavelength of $.73347\text{ Angstroms}$ and measured on beamline X3B1 at the National Synchrotron Light Source (NSLS), Brookhaven national Laboratory. Details of the x-ray diffraction technique were given in section 3.9.

B.1 X-ray Analysis

In order to search for a possible structural anomaly occurring at 160K in some UBe_{13} samples, we measured the lattice parameter (a_0) (obtained from a Bragg's law analysis of the high angle 0,2,10 diffraction peak) as a function of temperature from 30-300K. The results are presented in figure B.1. We see from figure B.1 that there is clearly a kink in the lattice parameter of this crystal, and that this kink occurs in the same temperature range as the anomaly in $\chi_{d.c.}$. It is important to note that the symmetry of the crystal structure (Fm $\bar{3}$ c, face centered cubic) was not altered due to this shift in a_0 . All peaks measured below the novel tran-

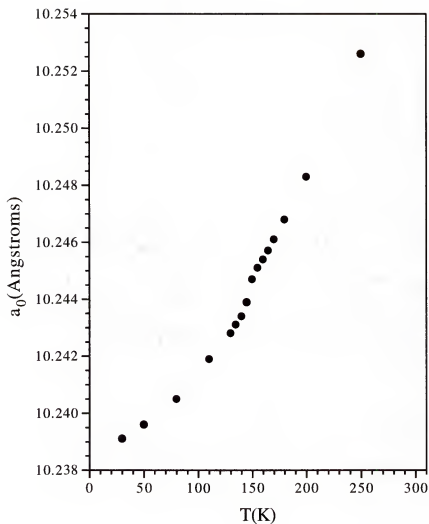


Figure B.1: The lattice parameter vs. temperature for powdered, annealed UBe_{13} single crystal 13A. Data were taken from 30-300K, but we concentrate here on the region of interest (160K). There is clearly an anomalous drop in the lattice parameter for this crystal, and the drop occurs over the same temperature range as the anomaly seen in $\chi_{d.c.}$. By using a reasonable extrapolation of the high temperature lattice parameter to lower temperatures we conclude that the shift in a_0 is on the order of .001 *Angstroms*.

sition retained there appropriate, cubic Miller indices. A reasonable extrapolation of the high temperature data to lower temperatures suggests that by 130K the anomalous event has resulted in an additional $.001 \text{ Angstrom}$ contraction of the lattice over that which would be expected from the high temperature trend. We have not been able to observe this effect in a similar measurement conducted on an anomaly-free single crystal. The number of data points gathered during a similar neutron diffraction study carried out previously were insufficient to observe the fine structure exhibited here. Our preliminary x-ray data of figure B.1 suggest that the electron density in anomalous UBe_{13} increases by roughly $.01\%$ in going from 130-170K. As this is an increase over that which would be expected from the existing trend, we would expect the d.c. resistivity to experience a corresponding decrease in this temperature range.

B.2 Resistivity

The d.c. resistance of a portion of annealed single crystal $10A$ was measured via the 4-probe technique discussed in section 3.5. The data are shown in figure B.2. These data clearly cover the temperature range in question with a resolution of 1 part in 10,000. No anomaly can be observed. This is quite surprising considering the measurable shift in the lattice parameter of a similar anomalous crystal displayed previously.

In this appendix we have seen, via synchrotron x-ray diffraction, that there appears to be some sort of structural anomaly which results in a contraction of the lattice by $\sim .001 \text{ Angstroms}$ in some UBe_{13} crystals. The temperature at which this structural anomaly takes place coincides with the temperature of the observed

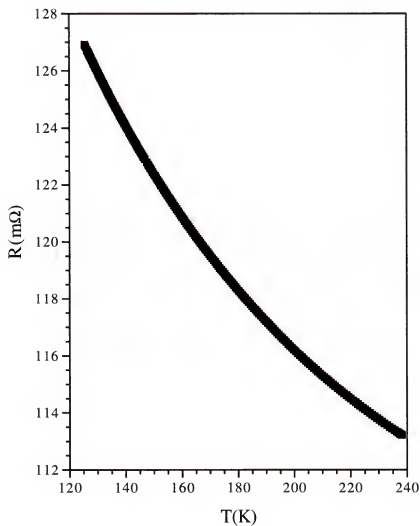


Figure B.2: The d.c. resistance vs. temperature for UBe_{13} crystal 10A. The data presented here give no indication for anomalous behavior over the entire temperature range shown. This crystal clearly displays the 160K anomaly in $\chi_{d.c.}$.

magnetic anomaly in $\chi_{d.c.}$. No change in the d.c. resistance was observed at this temperature. Further studies are obviously needed in order to better understand this novel magnetic-like state in some UBe_{13} samples.

REFERENCES

- [1] F. Steglich, J. Aarts, C.D. Bredl, W. Lieke, D. Meschede, W. Franz, and H. Schafer. *Phys. Rev. Lett.*, 43(25):1892, 1979.
- [2] D.W. Hess, P.S. Riceborough, and J.L. Smith. *Encyc. Appl. Phys.*, volume 7, page 435. VCH Pub., New York, 1993.
- [3] D.L. Cox and M.B. Maple. *Phys. Today*, pages 32–40, February 1995.
- [4] Z. Fisk, D.W. Hess, C.J. Pethick, D. Pines, J.L. Smith, J.D. Thompson, and J.O. Willis. *Science*, 239:33–42, 1 January 1988.
- [5] Z. Fisk, H.R. Ott, T.M. Rice, and J.L. Smith. *Nature*, 320:124–129, 13 March 1986.
- [6] M.B. Maple. *Phys. Today*, pages 72–80, March 1986.
- [7] G.R. Stewart. *Rev. Mod. Phys.*, 56(4):755–788, 1984.
- [8] C. Kittel. *Introduction to Solid State Physics*. John Wiley and Sons, Inc. New York, 6 edition, 1986.
- [9] K. Satoh, T. Fujita, Y. Maeno, Y. Onuki, and T. Komastabara. *J. Magn. Magn. Mat.*, 76-77:128, 1988.
- [10] S.G. Thomas, W.W. Kim, M. Lenkewitz, and G.R. Stewart. *Physica B*, 199-200:88, 1994.
- [11] J.O. Willis. Unpublished data.
- [12] H.R. Ott, H. Rudigier, P. Delsing, and Z. Fisk. *Phys. Rev. Lett.*, 52:1551, 1984.
- [13] Z. Fisk, G.R. Stewart, J.O. Willis, H.R. Ott, and F. Hulliger. *Phys. Rev. B*, 30:6360, 1984.
- [14] H.R. Ott, H. Rudigier, Z. Fisk, and J.L. Smith. *Phys. Rev. Lett.*, 50(20):1595–1598, 1983.

- [15] J.O. Willis J.L. Smith G.R. Stewart, Z. Fisk. *Phys. Rev. Lett.*, 52:679, 1984.
- [16] T.T.M. Palstra, A.A. Menovsky, J. van den Berg, A.J. Dirkmaat, P.H. Kes, G.J. Nieuwenhuys, and J.A. Mydosh. *Phys. Rev. Lett.*, 55(24):2727, 1985.
- [17] C. Geibel, S. Thies, D. Kaczorowski, A. Mehner, A. Granel, B. Seidel, U. Alheim, R. Helfrich, K. Peterson, C.D. Bredl, and F. Steglich. *Z. Phys. B*, 84:1, 1991.
- [18] K.G. Wilson. *Rev. Mod. Phys.*, 47:773, 1975.
- [19] G.R. Stewart, Z. Fisk, and M.S. Wire. *Phys. Rev. B*, 30:482, 1984.
- [20] C. Quitmann, B. Andraka, J.S. Kim, B. Treadway, G. Fraunberger, and G.R. Stewart. *Phys. Rev. B*, 38:6432, 1988.
- [21] M.S. Wire. PhD dissertation, Univ. Calif., San Diego, 1984.
- [22] J.O. Willis. *J. Appl. Phys.*, 61:4373, 1987.
- [23] P.H. Frings, J.J.M. Franse, F.R. deBoer, and A. Menovsky. *J. Magn. Magn. Matt.*, 31-34:240, 1983.
- [24] B. Battlog, J.P. Remeika, A.S. Cooper, and Z. Fisk. *J. Appl. Phys.*, 55:2001, 1984.
- [25] M.B. Maple. *Phys. Rev. Lett.*, 56:185, 1986.
- [26] C.M. Varma. *Comments Solid State Phys.*, 11:221, 1985.
- [27] K.H.J. Buschow and J.F. Fast. *Z. Phys. Chem.*, 50:1, 1966.
- [28] H.R. Ott, H. Rudigier, E. Felder, Z. Fisk, and J.D. Thompson. *Phys. Rev. B*, 35(3):1452, 1987-II.
- [29] J.O. Willis, J.D. Thompson, J.L. Smith, and Z. Fisk. *J. Magn. Magn. Matt.*, 63-64:461, 1987.
- [30] J.O. Willis. *Phys. Rev. B*, 31:1654, 1985.
- [31] F. Steglich, C.D. Bredl, W. Lieke, U. Rauchswalbe, and G. Sparn. *Physica*, 126B:82.
- [32] M.B. Maple, J.W. Chen, Y. Dalichaouch, T. Kohara, C. Rossel, and M.S. Torikachvili. *Phys. Rev. Lett.*, 56(2):185, 1986.

- [33] A. Amato, R. Feyerherm, F.N. Gyax, A. Schenk, M. Weber, R. Caspary, P. Hellman, C. Schank, C. Geibel, F. Steglich, D.E. MacLaughlin, E.A. Knetsch, and R.H. Heffner. *Europhys. Lett.*, 19:127, 1992.
- [34] J.W. Allen, S.J. Oh, L.E. Cox, W.P. Ellis, M.S. Wire, Z. Fisk, J.L. Smith, B.B. Pate, I. Lindau, and A.J. Arko. *Phys. Rev. Lett.*, 54:2635, 1985.
- [35] J.W. Allen. *J. Magn. Magn. Matt.*, 76-77:324, 1988.
- [36] S. Chapman, M. Hunt, P. Meeson, P.H.P. Reinders, M. Springfield, and M. Norman. *J. Phys. Condens. Matt.*, 2:8123, 1990.
- [37] L. Taillefer, R. Newbury, G.G. Lonzarich, Z. Fisk, and J.L. Smith. *J. Magn. Magn. Matt.*, 63-64:372, 1987.
- [38] C. Geibel, S. Thies, D. Kaczorowski, A. Mehner, A. Grauel, B. Seidel, U. Alheim, R. Helfrich, K. Peterson, C.D. Bredl, and F. Steglich. *Z. Phys. B*, 83:305, 1991.
- [39] M. Tinkham. *Introduction to Superconductivity*. McGraw-Hill, New York, 2 edition, 1996.
- [40] R.H. Heffner and M.R. Norman. *Preprint, Los Alamos National Laboratory*, 1995.
- [41] P. Fulde, J. Keller, and G. Zwicknagl. *Solid State Physics*, volume 41, page 1. Academic Press, San Diego, 1988.
- [42] P.W. Anderson. *J. Phys. Chem. Solids*, 11:26, 1959.
- [43] H.R. Ott, H. Rudigier, Z. Fisk, and J.L. Smith. *Phys. Rev. B*, 31(3):1651-1653, 1985.
- [44] R.A. Fisher, S. Kim, B.F. Woodfield, N.E. Phillips, L. Taillefer, K. Hasselbach, J. Flouquet, A.L. Giorgi, and J.L. Smith. *Phys. Rev. Lett.*, 62:1411, 1989.
- [45] E.A. Lynton. *Superconductivity*. Wiley, New York, 2 edition, 1964.
- [46] D. Vollhardt and P. Wolfe. *The Superfluid Phases of Helium 3*. Taylor and Francis, New York, 1990.
- [47] P.A. Lee, T.M. Rice, J.W. Serene, L.J. Sham, and J.W. Wilkins. *Comments Cond. Mat. Phys.*, 12(3):99-161, 1986.

- [48] P.W. Anderson. *Phys. Rev.*, 124:41, 1961.
- [49] J.R. Schrieffer and P.A. Wolf. *Phys. Rev.*, 149:491, 1966.
- [50] F.D.M. Haldane. *Phys. Rev. Lett.*, 40:416, 1978.
- [51] O. Gunnarsson and K. Schonhammer. *Phys. Rev. B*, 28:4315, 1983.
- [52] G. Baym and C.J. Pethick. *The Physics of Liquid and Solid Helium*, volume 2. Wiley, New York, 1978.
- [53] S. Doniach. *Physica B*, 91:231, 1977.
- [54] F. Steglich, C. Geibel, K. Gloos, G. Olesch, C. Schank, C. Wassilew, A. Loidl, A. Krimmel, and G.R. Stewart. *J. Low Temp. Phys.*, 95:3, 1994.
- [55] D.P. Shoemaker, R.E. Marsh, F.J. Ewing, and L. Pauling. *Acta Cryst.*, 5:637–644, 1952.
- [56] N.C. Baeuzinger and D.E. Rundle. *Acta Cryst.*, 2:258, 1949.
- [57] P. Villars and L.D. Calvert. *Pearson's Handbook of Crystallographic Data for Intermetallic Phases*. ASM International, Materials Park, OH, 2 edition, 1991.
- [58] J.L.C. Daams, P. Villars, and J.H.N. van Vucht. *Atlas of Crystal Structure Types for Intermetallic Phases*. ASM International, Materials Park, OH, 1991.
- [59] S.M. Shapiro, A.I. Goldman, G. Shirane, and D.E. Cox. *J. Magn. Magn. Mat.*, 52:418–420, 1985.
- [60] A.I. Goldman, S.M. Shapiro, D.E. Cox, J.L. Smith, and Z. Fisk. *Phys. Rev. B*, 32(9):6042–6044, 1985.
- [61] E.A. Knettsch. PhD dissertation, University of Leiden, 1996.
- [62] R. Felten, F. Steglich, G. Weber, H. Rietschel, F. Gompf, B. Renker, and J. Beuers. *Europhys. Lett.*, 2(4):323–329, 1986.
- [63] J.S. Kim and G.R. Stewart. *Phys. Rev. B*, 51(22):16190–16193, 1995.
- [64] Y. Lassailly, A.K. Bhattacharjee, and B. Coqblin. *Phys. Rev. B*, 31:7424, 1985.

- [65] B. Andraka, W.W. Kim, J.S. Kim, and G.R. Stewart. *Phys. Rev. B*, 44(10):5040–5045, 1991-II.
- [66] J.L. Smith, Z. Fisk, J.O. Willis, B. Batlogg, and H.R. Ott. *J. Appl. Phys.*, 55:1996, 1984.
- [67] F.G. Aliev, N.B. Brandt, R.V. Lutsiv, V.V. Moschalkov, and S.M. Chudinov. *JETP*, 35:539, 1982.
- [68] R. Felton, F. Steglich, G. Weber, H. Reitschel, F. Gompf, B. Renker, and J.B. Beuers. *Europhys. Lett.*, 2:323, 1986.
- [69] J.S. Schilling. *Phys. Rev. B*, 33:1667, 1986.
- [70] E.A. Knetsch, G.J. Nieuwenhuys, J.A. Mydosh, R.H. Heffner, and J.L. Smith. *Physica B*, 186-188:251, 1992.
- [71] H.M. Mayer, U. Rauchswalbe, F. Steglich, G.R. Stewart, and A.L. Giorgi. *Z. Phys. B*, 64:299, 1986.
- [72] G.M. Schmiedeshoff, A. Lacerda, Z. Fisk, and J.L. Smith. *Phys. Rev. B*, 54(10):7401–7405, 1996-II.
- [73] J.P. Brison, J. Flouquet, and G. Deutscher. *J. Low Temp. Phys.*, 76(5/6):453–464, 1989.
- [74] U. Rauchswalbe, F. Steglich, and H. Rietschel. *Physica*, 148B:33–36, 1987.
- [75] U. Rauchswalbe, F. Steglich, and H. Rietschel. *Europhys. Lett.*, 1(2):71–76, 1986.
- [76] J.O. Willis, J.D. Thompson, J.L. Smith, and Z. Fisk. *J. Magn. Magn. Mat.*, 63-64:461–463, 1987.
- [77] J.D. Thompson, M.W. McElfresh, J.O. Willis, Z. Fisk, J.L. Smith, and M.B. Maple. *Phys. Rev. B*, 35(1):48–54, 1987.
- [78] B. Andraka and G.R. Stewart. *Phys. Rev. B*, 49(17):12359–12361, 1994-I.
- [79] J.S. Kim, B. Andraka, C.S. Jee, S.B. Roy, and G.R. Stewart. *Phys. Rev. B*, 41(16):11073–11081, 1990.
- [80] R. Troc, W. Trzebiatowski, and K. Piprek. *Bull. L'academie Pol. des Sci.*, 19(6-7):427–432, 1971.

- [81] E. Bucher, J.P. Maita, G.W. Hull, R.C. Fulton, and A.S. Cooper. *Phys. Rev. B*, 11:440, 1975.
- [82] M.B. Maple, J.W. Chen, S.E. Lambert, Z. Fisk, J.L. Smith, H.R. Ott, J.S. Brooks, and M.J. Naughton. *Phys. Rev. Lett.*, 54(5):477-480, 1985.
- [83] J.P. Brison, J. Flouquet, and G. Deutscher. *J. Low Temp. Phys.*, 76:453, 1989.
- [84] D.E. MacLaughlin, C. Tien, W.G. Clark, M.D. Lan, Z. Fisk, J.L. Smith, and H.R. Ott. *Phys. Rev. Lett.*, 53:1833, 1984.
- [85] F. Gross, B.S. Chandrasekhar, K. Andres, U. Rauchswalbe, E. Bucher, and B. Luthi. *Physica C*, 153-155:439, 1988.
- [86] F. Thomas, B. Wand, T. Luhmann, P. Gegenwart, G.R. Stewart, and F. Steglich. *J. Low Temp. Phys.*, 102(1/2):117-132, 1996.
- [87] P.J.C. Signore, B. Andraka, G.R. Stewart, and M.W. Meisel. *Phys. Rev. B*, 52(14):10315-10326, 1995-II.
- [88] U. Rauchschwalbe. *Physica 147B*, pages 1-80, 1987.
- [89] G.M. Schmiedeshoff, Z. Fisk, and J.L. Smith. *Phys. Rev. B*, 45:10544, 1992.
- [90] N.E. Alekseevskii, V.I. Nizhaukovskii, V.N. Narozhnyi, E.P. Khlybov, and A.V. Mitin. *J. Low Temp. Phys.*, 64:87, 1986.
- [91] F.G. Aliev, V. Kovochik, V.V. Moshchalkov, V.V. Pryadun, N.E. Alekseevskii, A.V. Mitin, N. Agrait, and S. Vieira. *J. Low Temp. Phys.*, 85:359, 1991.
- [92] R.A. Fisher, S.E. Lacy, C. Marcenat, J.A. Olsen, N.E. Phillips, Z. Fisk, A.L. Giorgi, J.L. Smith, and G.R. Stewart. In L.C. Gupta and S.K. Malik, editors, *Theoretical and Experimental Aspects of Valence Fluctuations and Heavy Fermions*, pages 345-348. Plenum Publishing Corp., New York, 1987.
- [93] H.M. Mayer, U. Rauchschwalbe, C.D. Bredl, F. Steglich, H. Rietschel, H. Schmidt, H. Wuhl, and J. Beuers. *Phys. Rev. B*, 33(5):3168-3171, 1986.
- [94] W.P. Beyermann, R.H. Heffner, J.L. Smith, M.F. Hundley, P.C. Canfield, and J.D. Thompson. *Phys. Rev. B*, 51(1):404-409, 1995-I.
- [95] J.L. Smith, Z. Fisk, J.O. Willis, A.L. Giorgi, R.B. Roof, H.R. Ott, H. Rudigier, and E. Felder. *Physica*, 135B:3-8, 1985.

- [96] A.L. Giorgi, Z. Fisk, J.O. Willis, G.R. Stewart, and J.L. Smith. In U. Eckern, A. Schmid, W. Weber, and H. Wuhl, editors, *LT-17 (Contributed Papers)*, pages 229–230. North-Holland, Amsterdam, 1984.
- [97] J.L. Smith, Z. Fisk, J.O. Willis, H.R. Ott, S.E. Lambert, Y. Dalichaouch, and M.B. Maple. *J. Magn. Magn. Mat.*, 63-64:464–466, 1987.
- [98] U. Ahlheim, M. Winkelmann, P. van Aken, C.D. Bredl, F. Steglich, and G.R. Stewart. *J. Magn. Magn. Mat.*, 76-77:520–522, 1988.
- [99] M.J. Graf, N.A. Fortune, J.S. Brooks, J.L. Smith, and Z. Fisk. *Phys. Rev. B*, 40(13):9358–9361, 1989.
- [100] A.A. Abrikosov and L.P. Gor'kov. *JETP*, 12:1243, 1961.
- [101] T.F. Roenbaum. *Superconductivity Review*, 2:257–281, 1998.
- [102] E. Felder, A. Bernasconi, H.R. Ott, Z. Fisk, and J.L. Smith. *Physica C*, 162-164:429–430, 1989.
- [103] B. Batlogg, D. Bishop, B. Golding, C.M. Varma, Z. Fisk, J.L. Smith, and H.R. Ott. *Phys. Rev. Lett.*, 55:1319, 1985.
- [104] R.H. Heffner, J.L. Smith, J.O. Willis, P. Birrer, C. Baines, F.N. Gygax, B. Hitti, E. Lippelt, H.R. Ott, A. Schenk, E.A. Knetsch, J.A. Mydosh, and D.E. MacLaughlin. *Phys. Rev. Lett.*, 65:2816, 1990.
- [105] S.E. Lambert, Y. Dalichaouch, M.B. Maple, J.L. Smith, and Z. Fisk. *Z. Phys.*, 57:1619, 1986.
- [106] J.S. Kim, B. Andraka, and G.R. Stewart. *Phys. Rev. B*, 44(13):6921–6926, 1991-I.
- [107] R.H. Heffner, W.P. Beyermann, J.L. Smith, J.O. Willis, P. Birrer, C. Baines, F.N. Gygax, B. Hitti, E. Lippelt, H.R. Ott, A. Schenk, E.A. Knetsch, J.A. Mydosh, and D.E. MacLaughlin. *J. Appl. Phys.*, 69:5481, 1991.
- [108] A.P. Ramirez, C.M. Varma, Z. Fisk, and J.L. Smith. *Preprint, ATT Bell Laboratories*, 1994.
- [109] P.H.P. Reinders, B. Wand, F. Steglich, G. Fraunberger, G.R. Stewart, and G. Adrian. *Europhys. Lett.*, 25(8):619–624, 1994.
- [110] Z. Fisk and J.P. Remeika. *Handbook on the Physics and Chemistry of Rare Earths*, volume 12. Elsevier Science Pub. B.V., Amsterdam, 1989.

- [111] R. Bachmann, Jr. F.J. DiSalvo, T.H. Geballe, R.L. Greene, R.E. Howard, C.N. King, H.C. Kirsch, K.N. Lee, R.E. Schwall, H.U. Thomas, and R.B. Zubeck. *Rev. Sci. Instrum.*, 43(2):205, 1972.
- [112] G.R. Stewart. *Rev. Sci. Instrum.*, 54:1, 1983.
- [113] R. Bachman, H.C. Kirsch, and T.H. Geballe. *Rev. Sci. Instrum.*, 41:547, 1970.
- [114] J.S. Kim. PhD dissertation, Univ. of Florida, 1992.
- [115] B. Andracka and G.R. Stewart. *Rev. Sci. Instr.*, 62:837, 1991.
- [116] J.I. Goldstein, D.E. Newberry, P. Echlin, D.C. Joy, Jr. A.D. Romig, C.E. Lyman, C. Fiori, and E. Lifshin. *Scanning Electron Microscopy and X-ray Microanalysis*. Plenum Press, New York, 2 edition, 1992.
- [117] J.P. Brison, J.C. Lasjaunias, A. Ravex, J. Flouquet, D. Jaccard, Z. Fisk, and J.L. Smith. *Physica, C* 153-155:437-438, 1988.
- [118] M.J. Besnus, J.P. Kappler, and A. Meyer. *Solid State Comm.*, 48(9):835, 1983.
- [119] G.R. Stewart, Z. Fisk, J.L. Smith, H.R. Ott, and F.M. Mueller. In U. Eckern, A. Schmid, W. Weber, and H. Wuhl, editors, *LT-17 (Contributed Papers)*, pages 321-322. Elsevier Science Publishers B.V., Amsterdam, 1984.
- [120] H.M. Mayer, U. Rauchschwalbe, F. Steglich, G.R. Stewart, and A.L. Giorgi. *Z. Phys. B*, 64:299, 1986.
- [121] J.L. Smith, Z. Fisk, J.O. Willis, B. Batlogg, and H.R. Ott. *J. Appl. Phys.*, 55(6):1996, 1984.
- [122] C. Langhammer, R. Helfrich, A. Bach, F. Kromer, M. Lang, T. Michels, M. Deppe, F. Steglich, and G.R. Stewart. *J. Magn. Magn. Mater.*, 177-181:443-444, 1998.
- [123] R.N. Kleiman. *Phys. Rev. Lett.*, 64:1975, 1990.
- [124] A. de Visser. *Phys. Rev. B*, 45:2962, 1992.
- [125] E.T. Ahrens, P.C. Hammel, R.H. Heffner, A.P. Reyes, J.L. Smith, and W.G. Clark. *Phys. Rev. B*, 48(9):6691-6694, 1993-I.

- [126] H.R. Ott, E. Felder, Z. Fisk, R.H. Heffner, and J.L. Smith. *Phys. Rev. B*, 44(13):7081–7084, 1991-I.
- [127] R.H. Heffner, H.R. Ott, A. Schenck, J.A. Mydosh, and D.E. MacLaughlin. *J. Appl. Phys.*, 70(10):5782–5787, 1991.
- [128] Z. Fisk and H.R. Ott. *Int. J. Mod. Phys. B*, 3(4):535–571, 1989.
- [129] M.B. Maple. *Appl. Phys.*, 9:179–204, 1976.
- [130] E. Muller-Hartmann. *Magnetism: A Treatise on Modern Theory and Materials*, volume 5, chapter 12. Academic Press, New York, 1973.
- [131] D. Markowitz and L.P. Kadanoff. *Phys. Rev.*, 131(2):563–575, 1963.
- [132] H.R. Ott, H. Rudigier, T.M. Rice, K. Ueda, Z. Fisk, and J.L. Smith. *Phys. Rev. Lett.*, 52(21):1915–1918, 1984.
- [133] C. Broholm. *Phys. Rev. Lett.*, 65:2062, 1990.
- [134] K. Miyake, S. Schmitt-Rink, and C.M. Varma. *Phys. Rev. B*, 34:6554, 1986.
- [135] E. Schachinger and J.P. Carbotte. *Phys. Rev. B*, 43(13):10279–10288, 1991.
- [136] J.P. Carbotte. *Rev. Mod. Phys.*, 62:1027, 1990.
- [137] J.W. Chen. *J. Appl. Phys.*, 57:3076, 1985.
- [138] B. Ellman. *Phys. Rev. B*, 44:12074, 1991.
- [139] K. Miyake, S. Schmitt-Rink, and C.M. Varma. *Phys. Rev. Lett.*, 57:2575, 1986.
- [140] A.J. Millis, S. Sachdev, and C.M. Varma. *Phys. Rev. B*, 37:4975–4986, 1988.
- [141] D.J. Scalapino, E. Loh, and J.E. Hirsch. *Phys. Rev. B*, 34:8190, 1986.
- [142] J.E. Hirsch. *Phys. Rev. Lett.*, 54:1317, 1985.
- [143] P.G. deGennes. *Superconductivity of Metals and Alloys*. Addison-Wesley Pub. Co., Inc., Reading, MA, 1989.
- [144] F. Marsiglio and J.P. Carbotte. *Phys. Rev. B*, 33:6141, 1986.
- [145] P.J. Williams and J.P. Carbotte. *Phys. Rev. B*, 39(4):2180–2187, 1989.

- [146] P.J. Williams. *Phys. Rev. B*, 47(22):15145–15151, 1993-II.
- [147] W.E. Pickett, H. Krakauer, and C.S. Wang. *Physica*, 135 B-C(1-3):31–33, 1985.
- [148] A.J. Bevolo. *J. Less Comm. Met.*, 153:101, 1989.
- [149] G. Landgren, Y. Jugnet, J.F. Morar, A.J. Arko, Z. Fisk, J.L. Smith, H.R. Ott, and B. Reihl. *Phys. Rev. B*, 29:493, 1984.
- [150] E. Whilloud, Y. Baer, H.R. Ott, Z. Fisk, and J.L. Smith. *Phys. Rev. B*, 29:9, 1984.
- [151] F.G. Aliev, S. Vieira, R. Vilar, and J.L. Martinez. *JETP Lett.*, 60(8):591–594, 1994.
- [152] F.G. Aliev, S. Vieira, R. Villar, J.L. Martinez, C.L. Seaman, and M.B. Maple. *Physica B*, 206-207:454–456, 1995.

BIOGRAPHICAL SKETCH

The author was born and raised in lovely Levittown, Pennsylvania, and first entered school in the fall of 1971, around 9 o'clock. He quickly developed an affinity for books, cookies, and science. Twenty-seven years, 1 B.S., 1 M.S., 1 PhD., and far too many cookies later he has decided to finally leave school and pursue his childhood dream of never growing up.

General Audience Abstract of Dissertation Presented to the Graduate
School of the University of Florida in Partial Fulfillment of the
Requirements for the Degree of Doctor of Philosophy

AN INVESTIGATION OF SOME UNUSUAL SINGLE CRYSTALS
OF
THE HEAVY FERMION SUPERCONDUCTOR UBe_{13}

By

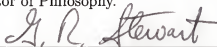
Stephen G. Thomas

December 1998

Chairman: G.R. Stewart
Major Department: Physics

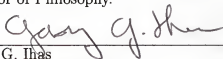
The novel crystals of UBe_{13} studied here become superconducting at a lower temperature than standard UBe_{13} , and the superconducting electrons inside are much more strongly coupled together. We have discovered that the presence of a small amount of Al is responsible for these effects. Through experimentation we have been able to induce this novel state in previously standard material. The anomalous behavior occurs only when the Al impurity resides on certain points within the crystal lattice. Since all atoms in the lattice interact with their local environment, by altering the local environment we alter these interactions. It appears that the local environment of the U atoms is being dramatically affected. This in turn causes a reduction in the frequency of interaction between individual U atoms, and results in the novel properties observed.

I certify that I have read this study and that in my opinion it conforms to acceptable standards of scholarly presentation and is fully adequate, in scope and quality, as a dissertation for the degree of Doctor of Philosophy.



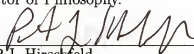
G.R. Stewart, Chairman
Professor of Physics

I certify that I have read this study and that in my opinion it conforms to acceptable standards of scholarly presentation and is fully adequate, in scope and quality, as a dissertation for the degree of Doctor of Philosophy.



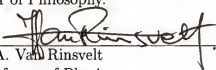
G.G. Ihas
Professor of Physics

I certify that I have read this study and that in my opinion it conforms to acceptable standards of scholarly presentation and is fully adequate, in scope and quality, as a dissertation for the degree of Doctor of Philosophy.



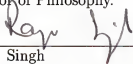
P.J. Hirschfeld
Professor of Physics

I certify that I have read this study and that in my opinion it conforms to acceptable standards of scholarly presentation and is fully adequate, in scope and quality, as a dissertation for the degree of Doctor of Philosophy.



H.A. Van Rinsvelt
Professor of Physics

I certify that I have read this study and that in my opinion it conforms to acceptable standards of scholarly presentation and is fully adequate, in scope and quality, as a dissertation for the degree of Doctor of Philosophy.



R. Singh
Professor of Materials Science

This dissertation was submitted to the Graduate Faculty of the Department of Physics in the College of Liberal Arts and Sciences and to the Graduate School and was accepted as partial fulfillment of the requirements for the degree of Doctor of Philosophy.

December 1998

Dean, Graduate School